

*Simulation of Terahertz Antennas in Free Space
and on Dielectric Substrates using the Green's
Function Surface Integral Equation Method*

DIPLOMA PROJECT
GROUP 5.325A, FYS10
PHYSICS
AALBORG UNIVERSITY
SUBMITTED JUNE 3, 2021

Department of Materials and
Production

9000 Aalborg

Title: Simulation of Terahertz Antennas in Free Space and on Dielectric Substrates using the Green's Function Surface Integral Equation Method



AALBORG UNIVERSITY
DENMARK

Project:

Diploma Project

Project Period:

02/02-2021 - 03/06-2021

Project Group: 5.325A, FYS10

Participants:

Daniel R. Simonsen

Frederik T. Schøler

Josefine M. Christensen

Supervisor:

Thomas M. Søndergaard

Number of Pages: 74

Number of Pages Incl. App.: 95

In this project, scattering problems with perfect electric conductors are numerically modelled using the the Green's Function Surface Integral Equation Method (GFSIEM). The developed method is tested by comparison between the analytic result of a current on a sphere with the simulated result. Then scatterers in the form of perfect electric conductors in the shape of boxes with rounded corners and edges are examined in free space with an incident electromagnetic field. Here the scattered far-field and the surface currents are examined. Furthermore, the configuration is analysed with the scatterers atop a silicon layer of infinite extent. It was found that the method provides accurate simulations of the surface currents and differential scattering cross sections of different geometries, both in free space and on dielectric substrates, with limitations at short wavelengths.

Preface

This thesis has been written by three students from the Department of Physics and Nanotechnology, Aalborg University, under supervision of Thomas M. Søndergaard, in the time period 02/02/2021 - 03/06/2021.

A special thanks is given to Thomas M. Søndergaard for his great help and guidance throughout the project period, where weekly meetings has been essential for understanding the theory along with the development and implementation of the code used for the simulations within this report.

Readers Guide

All aberrations throughout this project will be presented in the nomenclature, while less common aberrations furthermore will be presented in the text the first time it is used like *aberration of word* (AoW).

References within this report can be found throughout, where they will be denoted as e.g. Sec. A,B and Eq. (A,B), where A is a reference to the parent chapter in which e.g. the equation appears, while B represents the equations order of appearance within said chapter.

Citations to external sources used within this project has been cited as follows: [source, x. 1-2], where *source* is a number indicating the location of the source in the bibliography and $x. 1-2$ is an index of a number of pages or chapters used from the source. The references are typically located at the beginning of a section, indicating that the whole section is based on this/these reference(s). When this is not the case, references are located as they are utilized.

Nomenclature

CW	Continuous Wave
DSCS	Differential Scattering Cross Section
EFIE	Electric Field Integral Equation
FEM	Finite Element Method
GFIEM	Green's Function Integral Equation Method
GFSIEM	Green's Function Surface Integral Equation Method
LHS	Left Hand Side
MFIE	Magnetic Field Integral Equation
PCA	Photoconductive Antenna
PEC	Perfect Electric Conductor
PMC	Perfect Magnetic Conductor
RHS	Right Hand Side
RMSE	Root-Mean-Square Error

Table of Contents

1	Introduction	7
1.1	Modelling of Terahertz Radiation	7
1.2	Antennas	8
1.3	Terahertz Generation and Technology	9
2	Theory	10
2.1	Derivation of the General Wave Equation	11
2.2	Green's Function for a Homogeneous Medium	12
2.2.1	Mathematical Basis of the Dyadic Green's Function	13
2.2.2	Derivation of the Green's Function from the Electric- and the Magnetic Field	13
2.3	Surface Integral Equations	20
2.3.1	Derivation of the Surface Integral Equations	20
2.4	Layered Structure	26
2.4.1	Green's Function For a Layered Structure	26
2.4.2	The Far-Field Green's Tensor	28
2.4.3	The Magnetic Field Integral Equation for a Layered Structure	29
2.5	Multiple Scatterers	32
3	Method	35
3.1	Finite Element Mesh	35
3.1.1	Parameterisation of Triangular Elements	36
3.1.2	Polynomials	40
3.1.3	Two-Dimensional Polynomials	43
3.2	Implementation	44
3.2.1	Numerical Integration	46
3.2.2	Implementation of the Indirect Green's Tensor	48
4	Results and Analysis	51
4.1	Differential Scattering Cross Section of a Dipole	51
4.2	Evaluation of the Spherical Scatterer in Free Space	52
4.2.1	Comparison of Parameters	52
4.2.2	Evaluation of the Surface Current	59
4.2.3	Evaluating the Stability as a Function of the Wavelength	60
4.2.4	Evaluation of the Differential Scattering Cross Section	61

4.3	Evaluation of a Single Box-shaped Scatterer in Free Space	62
4.3.1	Evaluation of Resonance	63
4.3.2	Evaluation of the Surface Current	63
4.3.3	Evaluation of the Differential Scattering Cross Section	64
4.4	Evaluation of a Single Box-shaped Scatterer on a Layered Structure	65
4.4.1	Evaluation of the Surface Current	65
4.4.2	Evaluation of the Differential Scattering Cross Section	66
4.5	Evaluation of Multiple Box-shaped Scatterers	66
4.5.1	Comparison Between Two Coupled and Two Duplicated Scatterers	66
4.5.2	Multiple Box Antennas on a Layered Structure	68
4.5.3	Evaluation of the Differential Scattering Cross Section for Multiple Duplicated Scatterers	68
5	Conclusion	72
	Bibliography	73
A	Boundary Conditions	75
B	Weyl Expansion	77
C	Derivation of the Green's Function for a Layered Structure	79
C.1	The Differential Scattering Cross Section Green's Tensor	84
C.2	Curl of the Indirect Green's Tensor for the Electric Field	86
D	Higher-Dimensional Polynomials	88
E	Analytic Scattering from a Spherical Particle	91
E.1	Scattering Cross Section	94
E.2	Legendre Polynomials	94

Introduction

This project concerns itself with modelling of terahertz radiation scattering on metal antennas, and this chapter will therefore review different ways of modelling such radiation. Furthermore it will review different types of antennas along with different ways of generating terahertz radiation.

In Ch. 2 the theory behind the simulations will be presented, where different structures are concerned, which are all based on Fig. 2.1. Though, for all structures the first thing to be derived is the Green's tensor for the given structure, as it is essential in the Green's function integral equation method, where an integral including said Green's tensor is used in order to find the surface current of the scatterer(s) in question. From the surface current the far-field can be derived, which in turn is used to obtain the differential scattering cross section.

In order to accurately simulate these structures a finite element mesh is used, which will therefore be described in Ch. 3, along with a review of the implementation of the presented theory and the methods used to numerically calculate the surface current.

In Ch. 4 both the surface current and the differential scattering cross section will be simulated and discussed for all structures, however, within this chapter simulations of a spherical scatterer in free space will also be presented and compared to analytically obtained results, in order to evaluate the accuracy of the numerically obtained results for the previously mentioned structures.

Lastly, an overall conclusion to this project will be presented in Ch. 5.

1.1 Modelling of Terahertz Radiation

Terahertz radiation is the part of the electromagnetic spectrum ranging between infrared radiation and microwave radiation, with wavelengths ranging from around 1mm to $100\mu\text{m}$. For many years the spectrum was known as the "terahertz gap", as it is only relatively recent that practical technologies for generation and detection of terahertz radiation have been developed. Since the 90's, the field of terahertz radiation and spectroscopy has seen rapid development as terahertz radiation shows great promise for a variety of applications. These include biological uses such as determining vira[1] or detecting specific sugar molecules[2], security issues such as detection of explosives[3] and use in nondestructive testing[4], particularly in the aerospace industry[5].

This report is focused on modelling optical antennas for use in the terahertz regime using the Green's function surface integral equation method, which may also be known as the method of

moments, which is a useful method as only the surface of a scatterer needs to be taken into consideration in order to obtain information about the field surrounding the scatterer. In this project a finite element approach is used, where the surface is divided into triangular patches which will be referred to as elements, where a set of mesh points are defined. Now, the solution space of the current, which is solved for in the integral equation, is constrained to a piecewise polynomial expansion on each element. In order to do this, the integral equation is solved for each mesh point, which is in contrast to a typical Galerkin formulation[6, Ch. 8], where instead of solving the problem for a sample of mesh points, one would integrate over the individual elements with a set of basis functions. The Galerkin method with the integral equation would then require a double integral which would be more time consuming but with the advantage of softening the singularities. As this is not the approach used in this project, singularities have been carefully taken into consideration.

1.2 Antennas

This section is based on [7, ch. 13]

In general an antenna is a device designed to efficiently convert radiation to localized energy and vice versa. The most common and well known type of antenna is the radio wave antenna used in most telecommunication. Radio wave antennas consists of metal wires, which can be treated as perfect conductors. Running a current through the wires induces an electromagnetic field, which then, in turn, can induce a current in another antenna wire. The principle is the same in optical antennas, however, some considerations must be taken.

In contrast to radio wave antennas, optical antennas were originally designed for microscopy[8]. At optical frequencies, metal nanowires, the main component of optical antennas, cannot be thought of as perfect conductors, since the typical diameters of the wires are smaller than the skin depth of the metal they are comprised of. This results in the electromagnetic field fully penetrating the wires and inducing a volume current instead of pure surface currents as in radio wave antennas. Noble-metal nanowires can also support plasmon modes with wavelengths that are shorter than for free space, which at optical frequencies will dominate the behavior of the antenna. These considerations result in some key design differences between optical and radio wave antennas. One of the major differences between optical and radio wave antennas is the way an emitter or a receiver is connected to the antenna, as the small size of the optical antennas prevents them from being wired in a traditional way. Instead, optical antennas incorporate interconnects in their design.

As the terahertz spectrum lies between the optical and the radio spectrum, the terahertz antenna may share properties from optical as well as radio antennas. Here the terahertz frequency may be regarded as small in comparison to optical frequencies, thus, by using the Drude model for the metal scatterer in the low frequency limit, the permittivity of the scatterer may be assumed negative infinite[9], which will therefore be assumed for the scatterers in this project. This implies

that the scatterer is assumed to be a perfect electric conductor and is thereby equivalent to the modelling of the scattering by a regular radio antenna.

1.3 Terahertz Generation and Technology

Among the technologies that have managed to breach the terahertz gap is the *photoconductive antenna* (PCA)[10]. Here a DC voltage is applied between a metal dipole acting as an antenna placed on a photoconductive substrate, such as a semiconductor, where a short pulse in the timescale of a femtosecond, with energy higher than the band gap, is used to excite carriers in the antenna gap, resulting in a photocurrent driving the antenna. By ensuring a small lifetime for the carriers, the temporal dependence of the current is determined by the properties of the photoconductor which, by design, should result in a pulse lasting in the order of picoseconds with a significant part of the radiation in the terahertz spectrum. Similarly, a PCA may be used as a terahertz detector based on the currents that are controlled by the terahertz radiation rather than an applied DC voltage. By assuming an expression for the generated current in the gap between the contacts, the corresponding terahertz radiation for a PCA may be modelled with the Green's function surface integral equation method, however this has been out of the scope for this project.

An example of a continuous terahertz source is with photomixing[11], where the terahertz radiation originates from two *continuous wave* (CW) lasers that are slightly detuned to excite a modulated photocurrent, which may be coupled to an antenna in order to produce CW terahertz radiation.

In [12] the prospects of using a compact cylindrical microlens is examined, while in [13] a cylindrical gradient index microlens is optimised in order to collimate the generated terahertz radiation and out-couple it from the semiconductor substrate in which it propagates. According to [14], the radiated power may be amplified by utilising an array of terahertz emitters. This may either be done by aligning discrete PCA components or by a single die integrated approach with an array on the same substrate.

Theory

As was previously stated in Ch. 1, the aim of this project is to model terahertz antennas, also referred to as scatterers, and their ability to manipulate terahertz radiation in various setups, and it is therefore important to consider the physical laws that govern these phenomena. This chapter will therefore present the derivation of important equations used in the modelling of the behavior of electromagnetic waves in nano-optical setups. In order to do this the general wave equation will first be derived in Sec. 2.1 before relevant equations regarding the structure of interest will be presented, where the *Green's function integral equation method*, or GFIEM, and the *Green's function surface integral equation method*, or GFSIEM, is used.

The Structure of Interest

The theory within Sec. 2.2 and throughout the rest of this chapter will be regarding a structure as seen in Fig. 2.1, which is similar to the structure of a PCA. Here two metal scatterers with

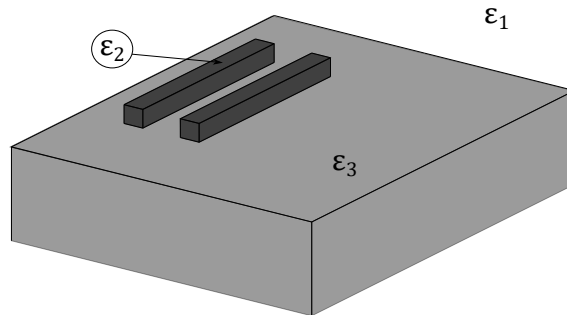


Figure 2.1: Illustration of the structure of interest.

permittivity ε_2 can be seen on top of an infinite homogeneous substrate with permittivity ε_3 , however, one could easily imagine an expansion of this structure by the addition of even more scatterers, while considering only a single scatterer would significantly simplify the structure, in turn simplifying the calculations which will be presented within this chapter. This structure is then further surrounded by a media with permittivity ε_1 , which is often considered to be that of vacuum, that is $\varepsilon_1 = 1$.

Within this chapter the problem of evaluating the structure in Fig. 2.1 will be split into different subproblems. Firstly, the simplest version of this structure possible will be presented in Sec. 2.2 and Sec. 2.3, i.e. a single scatterer completely surrounded by a homogeneous media which can easily be achieved by applying $\varepsilon_1 = \varepsilon_3$. Then a single scatterer on top of an infinite substrate

surrounded by an otherwise homogeneous media will be described in Sec. 2.4 before multiple scatterers will be considered in Sec. 2.5.

2.1 Derivation of the General Wave Equation

The content and derivations within this section are based on [15, Sec. 2.1].

In order to derive the general wave equation for both the electric- and the magnetic field, the macroscopic Maxwell equations in matter [15, Ch. 2.1, Eq. 2.1-2.4]

$$\nabla \cdot \mathbf{D}(\mathbf{r}, t) = \rho(\mathbf{r}, t), \quad (2.1a)$$

$$\nabla \cdot \mathbf{B}(\mathbf{r}, t) = 0, \quad (2.1b)$$

$$\nabla \times \mathbf{E}(\mathbf{r}, t) = -\frac{\partial \mathbf{B}(\mathbf{r}, t)}{\partial t}, \quad (2.1c)$$

$$\nabla \times \mathbf{H}(\mathbf{r}, t) = \mathbf{J}(\mathbf{r}, t) + \frac{\partial \mathbf{D}(\mathbf{r}, t)}{\partial t}, \quad (2.1d)$$

can be used. Here $\mathbf{D} = \varepsilon_0 \mathbf{E} + \mathbf{P}$ is the electric displacement for a linear, local and isotropic media, where \mathbf{P} is the induced polarisation density. If the displacement field is evaluated within the frequency domain rather than within the time domain it can be found that $\mathbf{D} = \varepsilon_0 \varepsilon \mathbf{E}$, where $\varepsilon(\mathbf{r}, \omega)$ is the dielectric constant. Furthermore, $\mathbf{B} = \mu_0 \mathbf{H}$ is the magnetic induction field for a non-magnetic material, ρ and \mathbf{J} are the free charge- and current density, respectively, while \mathbf{E} and \mathbf{H} are the electric- and the magnetic field, respectively.

By assuming that the time dependence for both the electric- and the magnetic field is on the form $e^{-i\omega t}$, the differential terms in Eq. (2.1) can be evaluated. If the fields are then evaluated in the frequency domain \mathbf{D} and \mathbf{B} can be replaced by their equivalent expressions in terms of \mathbf{E} and \mathbf{H} and the Maxwell equations can be rewritten into

$$\nabla \cdot (\varepsilon(\mathbf{r}) \mathbf{E}(\mathbf{r})) = \frac{\rho(\mathbf{r})}{\varepsilon_0}, \quad (2.2a)$$

$$\nabla \cdot \mathbf{H}(\mathbf{r}) = 0, \quad (2.2b)$$

$$\nabla \times \mathbf{E}(\mathbf{r}) = i\omega \mu_0 \mathbf{H}(\mathbf{r}), \quad (2.2c)$$

$$\nabla \times \mathbf{H}(\mathbf{r}) = \mathbf{J}(\mathbf{r}) - i\omega \varepsilon_0 \varepsilon(\mathbf{r}) \mathbf{E}(\mathbf{r}), \quad (2.2d)$$

where the frequency dependence has been omitted.

By isolating \mathbf{H} in Eq. (2.2c) and inserting this into Eq. (2.2d), and likewise isolating \mathbf{E} in Eq. (2.2d) and inserting this into Eq. (2.2c), results in a general wave equation for both the electric-

and the magnetic field on the form

$$\begin{aligned} \nabla \times \nabla \times \mathbf{E}(\mathbf{r}) &= i\omega\mu_0 (\mathbf{J}(\mathbf{r}) - i\omega\varepsilon_0\varepsilon(\mathbf{r})\mathbf{E}(\mathbf{r})) \\ \Rightarrow -\nabla \times \nabla \times \mathbf{E}(\mathbf{r}) + k_0^2\varepsilon(\mathbf{r})\mathbf{E}(\mathbf{r}) &= -i\omega\mu_0\mathbf{J}(\mathbf{r}), \end{aligned} \quad (2.3a)$$

$$\begin{aligned} \nabla \times \frac{1}{\varepsilon(\mathbf{r})} \nabla \times \mathbf{H}(\mathbf{r}) - \nabla \times \frac{1}{\varepsilon(\mathbf{r})} \mathbf{J}(\mathbf{r}) &= -i\omega\varepsilon_0 (i\omega\mu_0\mathbf{H}(\mathbf{r})) \\ \Rightarrow -\nabla \times \frac{1}{\varepsilon(\mathbf{r})} \nabla \times \mathbf{H}(\mathbf{r}) + k_0^2\mathbf{H}(\mathbf{r}) &= -\nabla \times \frac{1}{\varepsilon(\mathbf{r})} \mathbf{J}(\mathbf{r}). \end{aligned} \quad (2.3b)$$

These wave equations have to be fulfilled within both the scatterer and the surrounding media, however, the fields across the interface between these two have to be continuous and some boundary conditions for both the electric- and the magnetic field should therefore be considered. A more in depth derivation of these boundary conditions can be found in App. A, where they in Eq. (A.3) are found to be¹

$$\hat{\mathbf{n}} \cdot (\varepsilon_2\mathbf{E}_2(\mathbf{r}) - \varepsilon_1\mathbf{E}_1(\mathbf{r})) = \frac{\rho_s(\mathbf{r})}{\varepsilon_0}, \quad (2.4a)$$

$$\hat{\mathbf{n}} \cdot (\mathbf{H}_2(\mathbf{r}) - \mathbf{H}_1(\mathbf{r})) = 0, \quad (2.4b)$$

$$\hat{\mathbf{n}} \times (\mathbf{E}_2(\mathbf{r}) - \mathbf{E}_1(\mathbf{r})) = 0, \quad (2.4c)$$

$$\hat{\mathbf{n}} \times (\mathbf{H}_2(\mathbf{r}) - \mathbf{H}_1(\mathbf{r})) = \mathbf{J}_s(\mathbf{r}), \quad (2.4d)$$

where $\rho_s(\mathbf{r})$ and $\mathbf{J}_s(\mathbf{r})$ are the free surface charge- and current density respectively, while $\hat{\mathbf{n}}$ is the surface normal vector, which always points away from the scatterer and into the surrounding media. Furthermore, it should be noted that the boundary conditions in Eq. (2.4a) and Eq. (2.4b) relate to the transverse field components while the boundary conditions in Eq. (2.4c) and Eq. (2.4d) relate to the tangential field components.

2.2 Green's Function for a Homogeneous Medium

The content and derivations within this section are based on [7, Sec. 2.12 and Sec. 2.13] and [15, Sec. 6.2 and Sec. 9.1].

In order to accurately find both the electric- and the magnetic field one can use Green's functions, where it is useful to first introduce the dyadic Green's function, as the electric- and the magnetic field can be expressed as volume integral equations including said Green's tensor as seen in Eq. (2.22). From these equations the electric and magnetic field integral equations for a perfect conductor, Eq. (2.64) and Eq. (2.65) respectively, can be found, which in turn are used to derive the surface current in Eq. (2.75). However, before it can be introduced the mathematical basis behind it should be presented.

¹From this point on the notation $\mathbf{E}_i(\mathbf{r})$ will be used instead of $\mathbf{E}(\mathbf{r})$ in region i . This notation will further extend to the magnetic field along with the permittivity.

2.2.1 Mathematical Basis of the Dyadic Green's Function

If one is presented with an inhomogeneous differential equation on the form

$$\mathcal{L}\mathbf{A}(\mathbf{r}) = \mathbf{B}(\mathbf{r}), \quad (2.5)$$

where \mathcal{L} is a linear operator, $\mathbf{A}(\mathbf{r})$ is an unknown response of the system and $\mathbf{B}(\mathbf{r})$ is a known source function, causing the inhomogeneity, that is $\mathbf{B}(\mathbf{r}) \neq 0$, then the task of solving this equation can be rather difficult. However, by using that \mathcal{L} is linear it is known that a general solution to Eq. (2.5) can be expressed as the sum of the complete homogeneous solution, \mathbf{A}_0 , and a particular inhomogeneous solution. In order to find such an arbitrary inhomogeneous particular solution, when \mathbf{A}_0 is known, one can use the special inhomogeneity, $\delta(\mathbf{r} - \mathbf{r}')$, for which it is known that

$$\mathcal{L}\overleftrightarrow{\mathbf{G}}(\mathbf{r}, \mathbf{r}') = \overleftrightarrow{\mathbf{I}}\delta(\mathbf{r} - \mathbf{r}'). \quad (2.6)$$

Here $\overleftrightarrow{\mathbf{G}}(\mathbf{r}, \mathbf{r}')$ is the dyadic Green's function, also referred to as the Green's tensor, where \mathbf{r} is the point of evaluation and \mathbf{r}' is the position of the field source, while $\overleftrightarrow{\mathbf{I}}$ is the unit dyad. If it is then assumed that $\overleftrightarrow{\mathbf{G}}(\mathbf{r}, \mathbf{r}')$ has been found, then Eq. (2.6) can be rewritten by multiplying by $\mathbf{B}(\mathbf{r}')$ from the right and afterwards integrating over the volume of interest, which yields

$$\int_V \mathcal{L}\overleftrightarrow{\mathbf{G}}(\mathbf{r}, \mathbf{r}')\mathbf{B}(\mathbf{r}')d^3r' = \int_V \overleftrightarrow{\mathbf{I}}\mathbf{B}(\mathbf{r}')\delta(\mathbf{r} - \mathbf{r}')d^3r' = \mathbf{B}(\mathbf{r}). \quad (2.7)$$

By inserting Eq. (2.5) into this equation, it is straight forward to find an expression of $\mathbf{A}(\mathbf{r})$ on the form

$$\mathbf{A}(\mathbf{r}) = \int_V \overleftrightarrow{\mathbf{G}}(\mathbf{r}, \mathbf{r}')\mathbf{B}(\mathbf{r}')d^3r'. \quad (2.8)$$

2.2.2 Derivation of the Green's Function from the Electric- and the Magnetic Field

In order to find the unknown response of the system by solving Eq. (2.8), $\overleftrightarrow{\mathbf{G}}(\mathbf{r}, \mathbf{r}')$ has to be known, though, it has yet to be found. In order to find this dyadic Green's function one can use either the electric- or the magnetic field, however, within this section both fields will be used in order to achieve an expression for both fields that is dependent on $\overleftrightarrow{\mathbf{G}}(\mathbf{r}, \mathbf{r}')$. It should further be noted that the Green's functions which will be derived here are only valid in a single region at a time, hence $\varepsilon(\mathbf{r})$ is a region dependent constant, due to each region being homogeneous.

Firstly, the electric- and the magnetic field can be rewritten into the form

$$\mathbf{E}(\mathbf{r}) = i\omega\mathbf{A}(\mathbf{r}) - \nabla\varphi(\mathbf{r}), \quad (2.9a)$$

$$\mathbf{H}(\mathbf{r}) = \frac{1}{\mu_0}\nabla \times \mathbf{A}(\mathbf{r}), \quad (2.9b)$$

where $\mathbf{B}(\mathbf{r})$ has been expressed using a time-harmonic vector potential, $\mathbf{A}(\mathbf{r})$, as $\mathbf{B}(\mathbf{r}) = \nabla \times \mathbf{A}(\mathbf{r})$, and $\varphi(\mathbf{r})$ is a scalar potential, introduced when removing $\nabla \times$ in the electric field, since $\nabla \times \nabla \varphi(\mathbf{r}) =$

0. These fields can then be inserted into Eq. (2.2d) yielding

$$\nabla \times \nabla \times \mathbf{A}(\mathbf{r}) = \mu_0 \mathbf{J}(\mathbf{r}) - i\omega \mu_0 \varepsilon_0 \varepsilon (i\omega \mathbf{A}(\mathbf{r}) - \nabla \varphi(\mathbf{r})). \quad (2.10)$$

As neither $\mathbf{A}(\mathbf{r})$ nor $\varphi(\mathbf{r})$ are uniquely defined, the Lorenz gauge condition can be used such that

$$\varphi(\mathbf{r}) = \frac{1}{i\omega \mu_0 \varepsilon_0 \varepsilon} \nabla \cdot \mathbf{A}(\mathbf{r}), \quad (2.11)$$

and Eq. (2.10) can then be written on the form

$$\nabla \times \nabla \times \mathbf{A}(\mathbf{r}) = \mu_0 \mathbf{J}(\mathbf{r}) + k_0^2 \varepsilon \mathbf{A}(\mathbf{r}) + \nabla \nabla \cdot \mathbf{A}(\mathbf{r}). \quad (2.12)$$

Then the vector identity, $\nabla \times \nabla \times = -\nabla^2 + \nabla \nabla \cdot$, can be used to further rewrite this expression into the Helmholtz equation

$$(\nabla^2 + k_0^2 \varepsilon) \mathbf{A}(\mathbf{r}) = -\mu_0 \mathbf{J}(\mathbf{r}). \quad (2.13)$$

A similar expression can be found for $\varphi(\mathbf{r})$ by inserting Eq. (2.9a) into Eq. (2.2a) yielding

$$\begin{aligned} \nabla (\varepsilon (i\omega \mathbf{A}(\mathbf{r}) - \nabla \varphi(\mathbf{r}))) &= \frac{\rho(\mathbf{r})}{\varepsilon_0} \\ \Rightarrow \nabla \varepsilon \cdot (i\omega \mathbf{A}(\mathbf{r}) - \nabla \varphi(\mathbf{r})) + \varepsilon \nabla \cdot (i\omega \mathbf{A}(\mathbf{r}) - \nabla \varphi(\mathbf{r})) &= \frac{\rho(\mathbf{r})}{\varepsilon_0}. \end{aligned} \quad (2.14)$$

By then inserting Eq. (2.11) into this expression one finds that

$$(\nabla^2 + k_0^2 \varepsilon) \varphi(\mathbf{r}) = -\frac{\rho(\mathbf{r})}{\varepsilon_0 \varepsilon}. \quad (2.15)$$

It is easily seen that all three scalar equations in Eq. (2.13) ($A_x(\mathbf{r})$, $A_y(\mathbf{r})$ and $A_z(\mathbf{r})$) and the scalar equation in Eq. (2.15) are all on the form

$$(\nabla^2 + k_0^2 \varepsilon) f(\mathbf{r}) = -g(\mathbf{r}), \quad (2.16)$$

where the scalar Green's function appropriate for this inhomogeneous differential equation, $g(\mathbf{r}, \mathbf{r}')$, will satisfy

$$(\nabla^2 + k_0^2 \varepsilon) g(\mathbf{r}, \mathbf{r}') = -\delta(\mathbf{r} - \mathbf{r}'). \quad (2.17)$$

By realising that Eq. (2.16) is on the same form as in Eq. (2.5) one can by the same logic presented in Sec. 2.2.1 find an expression for $\mathbf{A}(\mathbf{r})$ and $\varphi(\mathbf{r})$ on the same form as in Eq. (2.8), hence

$$\mathbf{A}(\mathbf{r}) = \mu_0 \int_V g(\mathbf{r}, \mathbf{r}') \mathbf{J}(\mathbf{r}') d^3 r', \quad (2.18a)$$

$$\varphi(\mathbf{r}) = \frac{1}{\varepsilon_0 \varepsilon} \int_V g(\mathbf{r}, \mathbf{r}') \rho(\mathbf{r}') d^3 r'. \quad (2.18b)$$

However, in order to find $\mathbf{A}(\mathbf{r})$ or $\varphi(\mathbf{r})$ from these integrals, $g(\mathbf{r}, \mathbf{r}')$ has to be known. It can be shown[16, Sec. 6.4] that

$$g(\mathbf{r}, \mathbf{r}') = \frac{e^{\pm i k_0 \sqrt{\varepsilon} |\mathbf{r} - \mathbf{r}'|}}{4\pi |\mathbf{r} - \mathbf{r}'|}, \quad (2.19)$$

for a homogeneous three-dimensional media, where the sign denotes the direction of propagation of the spherical wave; that is '+' denotes a wave propagating away from the singularity, while

'-' denotes a wave that propagates towards it. From this point on only the radiating boundary condition will be considered, ensuring only outwards propagating waves, where the fields vanishes as the distance to the singularity increases.

While $g(\mathbf{r}, \mathbf{r}')$ is sufficient when the electric- and the magnetic field is expressed in terms of a vector- and a scalar potential, the dyadic Green's function has to be considered when this is not the case. The reason why $g(\mathbf{r}, \mathbf{r}')$ is insufficient in this case is that a source current in one direction, e.g. in the x -direction, will cause an electric- and a magnetic field with components in all three directions (x , y and z), as can be seen in Eq. (2.2c) and Eq. (2.2d), while the same source current will only lead to a vector potential with a single component in the same direction as the source current, as seen in Eq. (2.13).

In order to determine $\overleftrightarrow{\mathbf{G}}(\mathbf{r}, \mathbf{r}')$ for the electric- and the magnetic field, Eq. (2.3a) and Eq. (2.3b) should be considered respectively. These can be recalled as

$$\begin{aligned} -\nabla \times \nabla \times \mathbf{E}(\mathbf{r}) + k_0^2 \varepsilon \mathbf{E}(\mathbf{r}) &= -i\omega\mu_0 \mathbf{J}(\mathbf{r}), \\ -\nabla \times \nabla \times \mathbf{H}(\mathbf{r}) + k_0^2 \varepsilon \mathbf{H}(\mathbf{r}) &= -\nabla \times \mathbf{J}(\mathbf{r}), \end{aligned}$$

for a homogeneous material. Similarly to Eq. (2.17) it can be found that the dyadic Green's function appropriate for these differential equations satisfies

$$-\nabla \times \nabla \times \overleftrightarrow{\mathbf{G}}(\mathbf{r}, \mathbf{r}') + k_0^2 \varepsilon \overleftrightarrow{\mathbf{G}}(\mathbf{r}, \mathbf{r}') = -\overleftrightarrow{\mathbf{I}} \delta(\mathbf{r} - \mathbf{r}'), \quad (2.20)$$

where $\mathbf{E}(\mathbf{r})$ and $\mathbf{H}(\mathbf{r})$ can be found to be

$$\mathbf{E}(\mathbf{r}) = i\omega\mu_0 \int_V \overleftrightarrow{\mathbf{G}}(\mathbf{r}, \mathbf{r}') \mathbf{J}(\mathbf{r}') d^3 r', \quad (2.21a)$$

$$\mathbf{H}(\mathbf{r}) = \int_V (\nabla \times \overleftrightarrow{\mathbf{G}}(\mathbf{r}, \mathbf{r}')) \mathbf{J}(\mathbf{r}') d^3 r', \quad (2.21b)$$

by the same arguments presented in order to derive Eq. (2.18). However, as mentioned in Sec. 2.2.1 the general solution is the sum of a homogeneous solution and a particular inhomogeneous solution, as the ones just found, and the general solution of $\mathbf{E}(\mathbf{r})$ and $\mathbf{H}(\mathbf{r})$ can therefore be expressed as

$$\mathbf{E}(\mathbf{r}) = \mathbf{E}_0(\mathbf{r}) + i\omega\mu_0 \int_V \overleftrightarrow{\mathbf{G}}(\mathbf{r}, \mathbf{r}') \mathbf{J}(\mathbf{r}') d^3 r', \quad (2.22a)$$

$$\mathbf{H}(\mathbf{r}) = \mathbf{H}_0(\mathbf{r}) + \int_V (\nabla \times \overleftrightarrow{\mathbf{G}}(\mathbf{r}, \mathbf{r}')) \mathbf{J}(\mathbf{r}') d^3 r', \quad (2.22b)$$

which are also known as the volume integral equations.

The last step in order to be able to accurately determine the electric- and the magnetic field from these equations is to find an expression for $\overleftrightarrow{\mathbf{G}}(\mathbf{r}, \mathbf{r}')$. In order to do this the Lorenz gauge in Eq.

(2.11) is used in Eq. (2.9a), yielding

$$\begin{aligned}\mathbf{E}(\mathbf{r}) &= i\omega\mathbf{A}(\mathbf{r}) - \frac{1}{i\omega\mu_0\varepsilon_0\varepsilon}\nabla\nabla\cdot\mathbf{A}(\mathbf{r}) \\ &= i\omega\left(1 + \frac{1}{k_0^2\varepsilon}\nabla\nabla\cdot\right)\mathbf{A}(\mathbf{r}).\end{aligned}\quad (2.23)$$

If then a single component of Eq. (2.20) is considered, e.g.

$$-\nabla\times\nabla\times\mathbf{G}_x(\mathbf{r},\mathbf{r}') + k_0^2\varepsilon\mathbf{G}_x(\mathbf{r},\mathbf{r}') = -\delta(\mathbf{r}-\mathbf{r}')\mathbf{I}_x, \quad (2.24)$$

and compared to the wave equation for the electric field, it is easily recognised that $\mathbf{G}(\mathbf{r},\mathbf{r}') = \mathbf{E}(\mathbf{r})$ if $\mathbf{J}(\mathbf{r}) = (i\omega\mu_0)^{-1}\delta(\mathbf{r}-\mathbf{r}')\mathbf{n}_x$. If this current is then used in Eq. (2.18a) it can be found that

$$\begin{aligned}\mathbf{A}(\mathbf{r}) &= \mu_0\int_V g(\mathbf{r},\mathbf{r}')\frac{1}{i\omega\mu_0}\delta(\mathbf{r}-\mathbf{r}')\mathbf{I}_x d^3r' \\ &= \frac{1}{i\omega}g(\mathbf{r},\mathbf{r}')\mathbf{I}_x,\end{aligned}\quad (2.25)$$

which can then be used in Eq. (2.23), yielding

$$\mathbf{G}_x(\mathbf{r},\mathbf{r}') = \left(1 + \frac{1}{k_0^2\varepsilon}\nabla\nabla\cdot\right)g(\mathbf{r},\mathbf{r}')\mathbf{I}_x. \quad (2.26)$$

The dyadic Green's function can therefore be expressed as

$$\overleftrightarrow{\mathbf{G}}(\mathbf{r},\mathbf{r}') = \left(\overleftrightarrow{\mathbf{I}} + \frac{1}{k_0^2\varepsilon}\nabla\nabla\cdot\right)g(\mathbf{r},\mathbf{r}'), \quad (2.27)$$

where $\nabla\cdot(g(\mathbf{r},\mathbf{r}')\overleftrightarrow{\mathbf{I}}) = \nabla g(\mathbf{r},\mathbf{r}')$ has been used.

2.2.2.1 Validation of the Green's Functions

Up until this point $g(\mathbf{r},\mathbf{r}')$ and $\overleftrightarrow{\mathbf{G}}(\mathbf{r},\mathbf{r}')$ from Eq. (2.19) and Eq. (2.27) respectively, have been assumed to be solutions to Eq. (2.17) and Eq. (2.20), however, it has yet to be validated.

In order to prove that Eq. (2.19) is in fact a solution to Eq. (2.17) it should first be shown that

$$(\nabla^2 + k_0^2\varepsilon)g(\mathbf{r},\mathbf{r}') = 0 \quad \text{for } \mathbf{r} \neq \mathbf{r}'. \quad (2.28)$$

To ease the calculations, the singularity of the Green's function is set at the origin, $\mathbf{r}' = \mathbf{0}$, without loss of generality as this corresponds to a translation of the coordinates. When evaluating Eq. (2.28) it is useful to know that $\nabla r = \frac{\mathbf{r}}{r}$, where $r = |\mathbf{r}|$, and $\nabla^2 r = \frac{2}{r}$ when \mathbf{r} is three-dimensional. If Eq. (2.28) is then evaluated one term at a time it can be found that

$$\nabla g(\mathbf{r},\mathbf{0}) = \left(ik_0\sqrt{\varepsilon} - \frac{1}{r}\right)\frac{\mathbf{r}}{r}g(\mathbf{r},\mathbf{0}). \quad (2.29)$$

By then using the chain rule for a vector product, $\nabla\cdot(f\mathbf{A}) = \nabla f\cdot\mathbf{A} + f\nabla\cdot\mathbf{A}$, it can further be found that

$$\begin{aligned}\nabla^2 g(\mathbf{r},\mathbf{0}) &= \left(-k_0^2\varepsilon - \frac{ik_0\sqrt{\varepsilon}}{r} - \frac{ik_0\sqrt{\varepsilon}}{r} + \frac{2}{r^2}\right)g(\mathbf{r},\mathbf{0}) + \left(ik_0\sqrt{\varepsilon} - \frac{1}{r}\right)\frac{2}{r}g(\mathbf{r},\mathbf{0}) \\ &= \left(-k_0^2\varepsilon + \frac{2}{r^2} - 2\frac{ik_0\sqrt{\varepsilon}}{r} + 2\frac{ik_0\sqrt{\varepsilon}}{r} - \frac{2}{r^2}\right)g(\mathbf{r},\mathbf{0}) = -k_0^2\varepsilon g(\mathbf{r},\mathbf{0}),\end{aligned}\quad (2.30)$$

hence Eq. (2.28) is satisfied when $g(\mathbf{r},\mathbf{r}')$ is given as in Eq. (2.19), where $\mathbf{r} \neq \mathbf{r}'$ as the derivatives

are not defined at this point.

Next, the value at the singularity should be evaluated by integration, which must yield -1 if the singularity is contained in order to verify Eq. (2.17). By choosing a sphere of radius R in the limit of $R \rightarrow 0$ centered around the singularity for integration, this can be shown to be true by evaluating each term separately. By first evaluating the first term, using Gauss's theorem (Eq. (A.1a)), it can be found that

$$\lim_{R \rightarrow 0} \oint_S \nabla \frac{e^{ik_0\sqrt{\varepsilon}r}}{4\pi r} \cdot \hat{\mathbf{r}} d^2r = - \lim_{R \rightarrow 0} \oint_S \frac{1}{4\pi r^2} d^2r = -1, \quad (2.31)$$

where it has been used that the surface area of a sphere with radius r is $4\pi r^2$. Then the second term of Eq. (2.17) can be evaluated as

$$k_0^2 \varepsilon \lim_{R \rightarrow 0} \int_V \frac{e^{ik_0\sqrt{\varepsilon}r}}{4\pi r} d^3r = k_0^2 \varepsilon \lim_{R \rightarrow 0} \int_0^R r dr = k_0^2 \varepsilon \lim_{R \rightarrow 0} \frac{R^2}{2} = 0, \quad (2.32)$$

hence Eq. (2.17) is satisfied.

Now, in order to show that Eq. (2.27) is in fact a solution to Eq. (2.20), $\vec{\mathbf{G}}(\mathbf{r}, \mathbf{r}')$ is substituted into said equation while using the identity $\nabla \times (\nabla \times \mathbf{A}) = \nabla \nabla \cdot \mathbf{A} - \nabla^2 \mathbf{A}$, hence

$$\begin{aligned} & (\nabla^2 - \nabla \nabla \cdot + k_0^2 \varepsilon) \left(\overleftarrow{\mathbf{I}} + \frac{1}{k_0^2 \varepsilon} \nabla \nabla \right) g(\mathbf{r}, \mathbf{r}') \\ &= (\nabla^2 \overleftarrow{\mathbf{I}} - \nabla \nabla \cdot \overleftarrow{\mathbf{I}} + k_0^2 \varepsilon \overleftarrow{\mathbf{I}} + \frac{1}{k_0^2 \varepsilon} \nabla^2 \nabla \nabla - \frac{1}{k_0^2 \varepsilon} \nabla \nabla^2 \nabla + \nabla \nabla) g(\mathbf{r}, \mathbf{r}') \\ &= (\nabla^2 \overleftarrow{\mathbf{I}} + k_0^2 \varepsilon \overleftarrow{\mathbf{I}}) g(\mathbf{r}, \mathbf{r}'). \end{aligned} \quad (2.33)$$

As it has just been shown that $(\nabla^2 + k_0^2 \varepsilon)g(\mathbf{r}, \mathbf{r}') = -\delta(\mathbf{r} - \mathbf{r}')$ it is immediately obvious that $-\nabla \times \nabla \times \vec{\mathbf{G}}(\mathbf{r}, \mathbf{r}') + k_0^2 \varepsilon \vec{\mathbf{G}}(\mathbf{r}, \mathbf{r}') = -\overleftarrow{\mathbf{I}} \delta(\mathbf{r} - \mathbf{r}')$, hence Eq. (2.27) satisfies Eq. (2.20).

However, $\vec{\mathbf{G}}(\mathbf{r}, \mathbf{r}')$ has yet to be explicitly determined, which can be done by analytically evaluating Eq. (2.27) where Eq. (2.19) has been inserted. If the second term in Eq. (2.27) is evaluated one term at a time, and it is used that $\nabla R = \frac{\mathbf{R}}{R}$, where $R = |\mathbf{R}| = |\mathbf{r} - \mathbf{r}'|$, and $\nabla \nabla R = \frac{1}{R} \overleftarrow{\mathbf{I}} - \frac{\mathbf{R}\mathbf{R}}{R^3}$, it can be found that

$$\nabla g(\mathbf{r}, \mathbf{r}') = \left(ik_0 \sqrt{\varepsilon} - \frac{1}{R} \right) \frac{\mathbf{R}}{R} g(\mathbf{r}, \mathbf{r}'). \quad (2.34)$$

By then using that $\nabla(f\mathbf{A}) = (\nabla f)\mathbf{A} + f(\nabla \mathbf{A})$, it can further be found that

$$\begin{aligned} \nabla \nabla g &= \left(\left[ik_0 \sqrt{\varepsilon} \left(ik_0 \sqrt{\varepsilon} - \frac{1}{R} \right) - \frac{1}{R} \left(ik_0 \sqrt{\varepsilon} - \frac{1}{R} \right) + \frac{1}{R^2} \right] \frac{\mathbf{R}\mathbf{R}}{R^2} \right. \\ &\quad \left. + \left[ik_0 \sqrt{\varepsilon} - \frac{1}{R} \right] \left[\frac{1}{R} \overleftarrow{\mathbf{I}} - \frac{\mathbf{R}\mathbf{R}}{R^3} \right] \right) g(\mathbf{r}, \mathbf{r}') \\ &= \left(\left[-k_0^2 \varepsilon - \frac{2ik_0 \sqrt{\varepsilon}}{R} + \frac{2}{R^2} \right] \frac{\mathbf{R}\mathbf{R}}{R^2} + \left[ik_0 \sqrt{\varepsilon} - \frac{1}{R} \right] \left[\frac{1}{R} \overleftarrow{\mathbf{I}} - \frac{\mathbf{R}\mathbf{R}}{R^3} \right] \right) g(\mathbf{r}, \mathbf{r}') \\ &= \left(\left[-k_0^2 \varepsilon - \frac{3ik_0 \sqrt{\varepsilon}}{R} + \frac{3}{R^2} \right] \frac{\mathbf{R}\mathbf{R}}{R^2} + \left[\frac{ik_0 \sqrt{\varepsilon}}{R} - \frac{1}{R^2} \right] \overleftarrow{\mathbf{I}} \right) g(\mathbf{r}, \mathbf{r}'), \end{aligned} \quad (2.35)$$

yielding

$$\vec{\mathbf{G}}(\mathbf{r}, \mathbf{r}') = \left(\left[1 + \frac{i}{k_0 \sqrt{\epsilon} R} - \frac{1}{k_0^2 \epsilon R^2} \right] \overleftrightarrow{\mathbf{I}} - \left[1 + \frac{3i}{k_0 \sqrt{\epsilon} R} - \frac{3}{k_0^2 \epsilon R^2} \right] \frac{\mathbf{R}\mathbf{R}}{R^2} \right) g(\mathbf{r}, \mathbf{r}'). \quad (2.36)$$

2.2.2.2 The Far-Field of the Dyadic Green's Function

Up until this point the electric- and magnetic field just at the surface of the scatterer has been considered, however, as mentioned in Ch. 1 an antenna is used to receive and emit a signal. In the case where the antenna is used for emitting signals the far-field is of interest, since this is the detectable signal.

In the far-field $\vec{\mathbf{G}}(\mathbf{r}, \mathbf{r}')$ can be expressed in spherical coordinates where the unit vectors are defined as

$$\begin{aligned} \hat{\mathbf{r}} &= \frac{\mathbf{r}}{r}, \\ \hat{\boldsymbol{\theta}} &= \hat{\mathbf{x}} \cos \theta \cos \varphi + \hat{\mathbf{y}} \cos \theta \sin \varphi - \hat{\mathbf{z}} \sin \theta, \\ \hat{\boldsymbol{\phi}} &= -\hat{\mathbf{x}} \sin \varphi + \hat{\mathbf{y}} \cos \varphi. \end{aligned}$$

In the limit of far-field where \mathbf{r}' is close to the center of the sphere compared to \mathbf{r} most terms in Eq. (2.36) vanishes due to R being large, hence

$$\vec{\mathbf{G}}^{(ff)}(\mathbf{r}, \mathbf{r}') = \left(\overleftrightarrow{\mathbf{I}} - \frac{\mathbf{R}\mathbf{R}}{R^2} \right) g(\mathbf{r}, \mathbf{r}'). \quad (2.37)$$

By then using that

$$R = |\mathbf{r} - \mathbf{r}'| = \sqrt{(\mathbf{r} - \mathbf{r}') \cdot (\mathbf{r} - \mathbf{r}')} = \sqrt{r^2 - 2\mathbf{r} \cdot \mathbf{r}' + r'^2} \approx r - \frac{2r\hat{\mathbf{r}} \cdot \hat{\mathbf{r}}'}{2r} r' = r - \mathbf{r}' \cdot \hat{\mathbf{r}}, \quad (2.38)$$

where $r \gg r'$ has been used in order to make a second order Taylor expansion, and $\mathbf{r}' = r' \hat{\mathbf{r}}'$ has been applied, along with $\overleftrightarrow{\mathbf{I}} = \hat{\mathbf{r}}\hat{\mathbf{r}} + \hat{\boldsymbol{\theta}}\hat{\boldsymbol{\theta}} + \hat{\boldsymbol{\phi}}\hat{\boldsymbol{\phi}}$, it can be found that

$$\vec{\mathbf{G}}^{(ff)}(\mathbf{r}, \mathbf{r}') = \left(\hat{\boldsymbol{\theta}}\hat{\boldsymbol{\theta}} + \hat{\boldsymbol{\phi}}\hat{\boldsymbol{\phi}} \right) \frac{e^{ik_0 \sqrt{\epsilon} r}}{4\pi r} e^{-ik_0 \sqrt{\epsilon} \mathbf{r}' \cdot \hat{\mathbf{r}}}, \quad (2.39)$$

when Eq. (2.19) is inserted, as $\frac{\mathbf{R}\mathbf{R}}{R^2}$ in the far-field reduces to $\hat{\mathbf{r}}\hat{\mathbf{r}}$.

When considering the far-field it is furthermore relevant to consider the scattering cross section, as it represents the cross sectional area for which the field is prevented from propagating forward. The scattering cross section reveals how well the incident field couples with the corresponding metal nanoparticle, e.g. the antenna, resulting in surface currents that are dissipated in the form of a scattered far-field. The scattering cross section can be much larger than the physical cross section of the scatterer, which is evident in the case of resonant metal nanoparticles in which case the field couples well with the scatterer. The scattering cross section is obtained by normalising the scattered power by the incident power per unit area, and represents how much the scatterer influences the incident field. In the case of no absorption, the *differential scattering cross section* (DSCS) for an incident plane wave propagating along $-\hat{\mathbf{z}}$ with the incident field \mathbf{E}_i may be written

with respect to the electric field as

$$\frac{\partial \sigma}{\partial \Omega}(\mathbf{r}) = \frac{|\mathbf{E}_{\text{scat}}^{(ff)}(\mathbf{r})|^2}{|\mathbf{E}_0|^2} r^2 \quad \text{for } \theta < \pi/2 \quad (2.40a)$$

$$\frac{\partial \sigma}{\partial \Omega}(\mathbf{r}) = \frac{n_3}{n_1} \frac{|\mathbf{E}_{\text{scat}}^{(ff)}(\mathbf{r})|^2}{|\mathbf{E}_0|^2} r^2 \quad \text{for } \theta > \pi/2 \quad (2.40b)$$

where n_1 and n_3 are the indices of refraction above and below the scatterer respectively, which comes from the magnitude of the Poynting vector going as $|\mathbf{S}| = n|\mathbf{E}|^2$, while $\mathbf{E}_{\text{scat}}^{(ff)}(\mathbf{r})$ is the field scattered by the antenna. The scattering cross section is then given by integrating over the DSCS over the upper half of a unit sphere

$$\sigma = \int_0^{\pi/2} \int_0^{2\pi} \frac{\partial \sigma}{\partial \Omega}(\mathbf{r}) \sin \theta d\varphi d\theta. \quad (2.41)$$

2.2.2.3 Reciprocity

The theorem of reciprocity states, in general, that the source and detector of an electromagnetic system may be interchanged without affecting the physical situation. To derive the theorem two spatially separate volumes V_1 and V_2 , with current densities \mathbf{J}_1 and \mathbf{J}_2 , respectively, are considered. For simplicity only monochromatic fields are considered, where \mathbf{J}_1 induces \mathbf{E}_1 and \mathbf{H}_1 , while \mathbf{J}_2 induces \mathbf{E}_2 and \mathbf{H}_2 . The Maxwell curl equations for the two fields (Eq. (2.1c) and Eq. (2.1d)) are then given by

$$\nabla \times \mathbf{E}_1 = i\omega \mathbf{B}_1, \quad (2.42a)$$

$$\nabla \times \mathbf{H}_1 = -i\omega \mathbf{D}_1 + \mathbf{J}_1, \quad (2.42b)$$

$$\nabla \times \mathbf{E}_2 = i\omega \mathbf{B}_2, \quad (2.42c)$$

$$\nabla \times \mathbf{H}_2 = -i\omega \mathbf{D}_2 + \mathbf{J}_2. \quad (2.42d)$$

Multiplying Eq. (2.42a) by \mathbf{H}_2 , Eq. (2.42b) by \mathbf{E}_2 , Eq. (2.42c) by \mathbf{H}_1 and Eq. (2.42d) by \mathbf{E}_1 , all from the left, and then subtracting the sum of Eq. (2.42c) and Eq. (2.42d) from the sum of Eq. (2.42a) and Eq. (2.42b) yields

$$\begin{aligned} & (\mathbf{H}_2 \cdot \nabla \times \mathbf{E}_1 - \mathbf{E}_1 \cdot \nabla \times \mathbf{H}_2) + (\mathbf{E}_2 \cdot \nabla \times \mathbf{H}_1 - \mathbf{H}_1 \cdot \nabla \times \mathbf{E}_2) \\ & = i\omega(\mathbf{H}_2 \cdot \mathbf{B}_1 - \mathbf{H}_1 \cdot \mathbf{B}_2) - i\omega(\mathbf{E}_2 \cdot \mathbf{D}_1 - \mathbf{E}_1 \cdot \mathbf{D}_2) + (\mathbf{E}_2 \cdot \mathbf{J}_1 - \mathbf{E}_1 \cdot \mathbf{J}_2). \end{aligned} \quad (2.43)$$

By using that $\nabla \cdot (\mathbf{A} \times \mathbf{B}) = (\nabla \times \mathbf{A}) \cdot \mathbf{B} - \mathbf{A} \cdot (\nabla \times \mathbf{B})$, along with the scalar product being commutative, in this case $\mathbf{H}_i \cdot (\nabla \times \mathbf{E}_j) = (\nabla \times \mathbf{E}_j) \cdot \mathbf{H}_i$, the LHS can be rewritten as

$$LHS = \nabla \cdot (\mathbf{E}_1 \times \mathbf{H}_2 - \mathbf{E}_2 \times \mathbf{H}_1). \quad (2.44)$$

The first two terms on the RHS cancel, since $\mathbf{H}_2 \cdot \mathbf{B}_1 = \mathbf{H}_1 \cdot \mathbf{B}_2$ and $\mathbf{E}_2 \cdot \mathbf{D}_1 = \mathbf{E}_1 \cdot \mathbf{D}_2$, and Eq. (2.43) therefore reduces to

$$\nabla \cdot (\mathbf{E}_1 \times \mathbf{H}_2 - \mathbf{E}_2 \times \mathbf{H}_1) = (\mathbf{J}_1 \cdot \mathbf{E}_2 - \mathbf{J}_2 \cdot \mathbf{E}_1), \quad (2.45)$$

which is known as the Lorentz reciprocity theorem.

When integrating Eq. (2.45) over a spherical volume with a large radius, assuming that all objects and sources are finite in size, so that the far-fields are transverse to the surface normal of the volume, making the LHS vanish, and furthermore applying Gauss's theorem, the following is obtained

$$\int_{V_1} \mathbf{J}_1 \cdot \mathbf{E}_2 d^3r = \int_{V_2} \mathbf{J}_2 \cdot \mathbf{E}_1 d^3r. \quad (2.46)$$

The fields \mathbf{E}_1 and \mathbf{E}_2 can then be expressed in terms of their source currents by means of the Green's tensor, $\overleftrightarrow{\mathbf{G}}$, using Eq. (2.21a) which leads to

$$\overleftrightarrow{\mathbf{G}}(\mathbf{r}_1, \mathbf{r}_2) = \overleftrightarrow{\mathbf{G}}(\mathbf{r}_2, \mathbf{r}_1). \quad (2.47)$$

From this it can be seen that the theorem of reciprocity, implies that the Green's tensor is symmetric and is therefore unaffected by interchanging the source and detector.

2.3 Surface Integral Equations

The content and derivations within this section are based on [15, Sec. 9.1].

While the current density can be found using the volume integral equations from Eq. (2.22), only the surface current density is relevant due to the approximation that the antenna is a *perfect electric conductor*, or a PEC, as mentioned in Ch. 1. While the surface current density can be found from the total current density, it significantly simplifies the calculations if it is instead found using surface integral equations, as this only requires a mesh on the surface of the antenna rather than a mesh of the entire volume. A further explanation of the finite element mesh used in this project will be given in Sec. 3.1.

2.3.1 Derivation of the Surface Integral Equations

Consider a situation as illustrated in Fig. 2.2, where a scatterer with dielectric constant ε_2 is embedded in a homogeneous region with dielectric constant ε_1 . Furthermore, the region inside the scatterer is designated Ω_2 , the region outside it is designated Ω_1 , and the scatterer is illuminated by an incident field $\mathbf{E}_0(\mathbf{r})$. The vector wave equation for the electric field in a homogeneous region, Ω_i , with the associated dielectric constant ε_i , was found in Eq. (2.3a), while the Green's tensor for the same homogeneous medium was found in Eq. (2.20). These can be recalled as

$$-\nabla \times \nabla \times \mathbf{E}(\mathbf{r}) + k_0^2 \varepsilon_i \mathbf{E}(\mathbf{r}) = -i\omega \mu_0 \mathbf{J}(\mathbf{r}), \quad \mathbf{r} \in \Omega_i,$$

and

$$-\nabla \times \nabla \times \overleftrightarrow{\mathbf{G}}_i(\mathbf{r}, \mathbf{r}') + k_0^2 \varepsilon_i \overleftrightarrow{\mathbf{G}}_i(\mathbf{r}, \mathbf{r}') = -\overleftrightarrow{\mathbf{I}} \delta(\mathbf{r} - \mathbf{r}'),$$

respectively, and from these the surface integral equations will be derived.

By multiplying the vector wave equation for the electric field by $\overleftrightarrow{\mathbf{G}}_i(\mathbf{r}, \mathbf{r}')$ from the right and multiplying the equation for the Green's tensor by $\mathbf{E}(\mathbf{r})$ from the left before then subtracting the

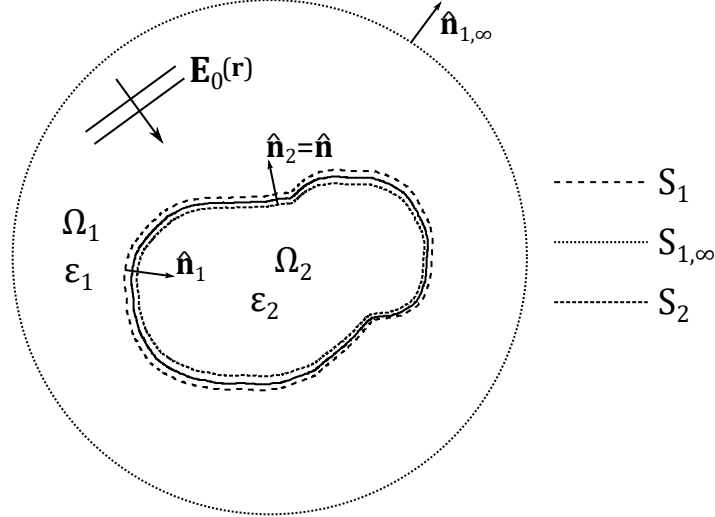


Figure 2.2: Illustration of a three-dimensional scatterer within an otherwise homogeneous medium. S_1 and S_2 denotes a line just outside and inside the scatterer respectively, while $S_{1,\infty}$ represents a spherical line surrounding both media infinitely far away from the scatterer. This illustration is inspired by [15, Fig. 9.1].

newly achieved equation for the Green's tensor from the newly achieved vector wave equation yields

$$\begin{aligned} & (-\nabla \times \nabla \times \mathbf{E}(\mathbf{r})) \cdot \vec{\mathbf{G}}_i(\mathbf{r}, \mathbf{r}') + \mathbf{E}(\mathbf{r}) \cdot (\nabla \times \nabla \times \vec{\mathbf{G}}_i(\mathbf{r}, \mathbf{r}')) \\ & = -i\omega\mu_0 \mathbf{J}(\mathbf{r}) \cdot \vec{\mathbf{G}}_i(\mathbf{r}, \mathbf{r}') + \mathbf{E}(\mathbf{r}) \delta(\mathbf{r} - \mathbf{r}'). \end{aligned} \quad (2.48)$$

Now the LHS and the RHS can be integrated with respect to \mathbf{r} over region Ω_i , which for the RHS yields

$$RHS = -\mathbf{E}_{0,i}(\mathbf{r}') + \mathbf{E}(\mathbf{r}'), \quad \mathbf{r}' \in \Omega_i, \quad (2.49)$$

where the incident field in the region is defined from Eq. (2.21a) as

$$\mathbf{E}_{0,i}(\mathbf{r}') = i\omega\mu_0 \int_{\Omega_i} \vec{\mathbf{G}}_i(\mathbf{r}', \mathbf{r}) \cdot \mathbf{J}(\mathbf{r}) d^3r, \quad (2.50)$$

and the property of reciprocity from Eq. (2.47),

$$\mathbf{J}(\mathbf{r}) \cdot \vec{\mathbf{G}}_i(\mathbf{r}, \mathbf{r}') = \vec{\mathbf{G}}_i(\mathbf{r}', \mathbf{r}) \cdot \mathbf{J}(\mathbf{r}), \quad (2.51)$$

has been utilized.

The integral over Ω_i of the LHS can, using the vector property $\nabla \cdot (\mathbf{A} \times \mathbf{B}) = (\nabla \times \mathbf{A}) \cdot \mathbf{B} - \mathbf{A} \cdot (\nabla \times \mathbf{B})$, be written as

$$\begin{aligned} LHS &= \int_{\Omega_i} \left[-\nabla \cdot (\{\nabla \times \mathbf{E}(\mathbf{r})\} \times \vec{\mathbf{G}}_i(\mathbf{r}, \mathbf{r}')) - (\nabla \times \mathbf{E}(\mathbf{r})) \cdot (\nabla \times \vec{\mathbf{G}}_i(\mathbf{r}, \mathbf{r}')) \right. \\ &\quad \left. - \nabla \cdot (\mathbf{E}(\mathbf{r}) \times \{\nabla \times \vec{\mathbf{G}}_i(\mathbf{r}, \mathbf{r}')\}) + (\nabla \times \mathbf{E}(\mathbf{r})) \cdot (\nabla \times \vec{\mathbf{G}}_i(\mathbf{r}, \mathbf{r}')) \right] d^3r \\ &= \int_{\Omega_i} -\nabla \cdot \left[(\{\nabla \times \mathbf{E}(\mathbf{r})\} \times \vec{\mathbf{G}}_i(\mathbf{r}, \mathbf{r}')) + (\mathbf{E}(\mathbf{r}) \times \{\nabla \times \vec{\mathbf{G}}_i(\mathbf{r}, \mathbf{r}')\}) \right] d^3r, \end{aligned} \quad (2.52)$$

where it in the first term of Eq. (2.48) has been used that $\mathbf{A} = \nabla \times \mathbf{E}(\mathbf{r})$ and $\mathbf{B} = \vec{\mathbf{G}}_i(\mathbf{r}, \mathbf{r}')$ while it in the second term has been used that $\mathbf{A} = \mathbf{E}(\mathbf{r})$ and $\mathbf{B} = \nabla \times \vec{\mathbf{G}}_i(\mathbf{r}, \mathbf{r}')$.

Applying Gauss's theorem, Eq. (A.1a), one can convert Eq. (2.52) to a surface integral over the surface of Ω_i , designated $\partial\Omega_i$, hence

$$LHS = \oint_{\partial\Omega_i} -\hat{\mathbf{n}}_i \cdot \left[\{\nabla \times \mathbf{E}(\mathbf{r})\} \times \vec{\mathbf{G}}_i(\mathbf{r}, \mathbf{r}') + \mathbf{E}(\mathbf{r}) \times \left\{ \nabla \times \vec{\mathbf{G}}_i(\mathbf{r}, \mathbf{r}') \right\} \right] d^2r, \quad (2.53)$$

where $\hat{\mathbf{n}}_i$ is the surface normal vector pointing out from Ω_i . Using the vector property $\mathbf{A} \cdot (\mathbf{B} \times \mathbf{C}) = (\mathbf{A} \times \mathbf{B}) \cdot \mathbf{C}$, Eq. (2.53) can then be further rewritten as

$$LHS = \oint_{\partial\Omega_i} - \left[(\hat{\mathbf{n}}_i \times \{\nabla \times \mathbf{E}(\mathbf{r})\}) \cdot \vec{\mathbf{G}}_i(\mathbf{r}, \mathbf{r}') + (\hat{\mathbf{n}}_i \times \mathbf{E}(\mathbf{r})) \cdot (\nabla \times \vec{\mathbf{G}}_i(\mathbf{r}, \mathbf{r}')) \right] d^2r. \quad (2.54)$$

Now the LHS from Eq. (2.54) can be combined with the RHS from Eq. (2.49), however, before doing so it is convenient to introduce the electric- and the magnetic surface current densities of the surface of Ω_i , which are defined as

$$\mathbf{J}_{s,i}(\mathbf{r}) \equiv -\hat{\mathbf{n}}_i \times \mathbf{H}(\mathbf{r}), \quad \mathbf{r} \text{ on } \partial\Omega_i, \quad (2.55a)$$

$$\mathbf{M}_{s,i}(\mathbf{r}) \equiv \hat{\mathbf{n}}_i \times \mathbf{E}(\mathbf{r}), \quad \mathbf{r} \text{ on } \partial\Omega_i, \quad (2.55b)$$

respectively. By these definitions, along with $\nabla \times \mathbf{E}(\mathbf{r}) = i\omega\mu_0\mathbf{H}(\mathbf{r})$ from Eq. (2.2c), Eq. (2.48) yields

$$\mathbf{E}(\mathbf{r}') = \mathbf{E}_{0,i}(\mathbf{r}') + i\omega\mu_0 \oint_{\partial\Omega_i} \mathbf{J}_{s,i}(\mathbf{r}) \cdot \vec{\mathbf{G}}_i(\mathbf{r}, \mathbf{r}') d^2r - \oint_{\partial\Omega_i} \mathbf{M}_{s,i}(\mathbf{r}) \cdot (\nabla \times \vec{\mathbf{G}}_i(\mathbf{r}, \mathbf{r}')) d^2r. \quad (2.56)$$

Though, here $\mathbf{E}_{0,i}$, \mathbf{E} and the integrals depend on \mathbf{r}' and for convenience this should therefore be rewritten such that $\mathbf{E}_{0,i}$, \mathbf{E} and the integrals instead depend on \mathbf{r} . While this is straightforward for $\mathbf{E}_{0,i}$, \mathbf{E} and the first integral due to the reciprocity condition, previously applied to find Eq. (2.49), the coordinates in the second integral are not as easily interchanged. It can be seen in Eq. (2.36) that $\vec{\mathbf{G}}(\mathbf{r}, \mathbf{r}')$ does not depend on neither \mathbf{r} nor \mathbf{r}' independently. Instead it depends on \mathbf{R} , where it can be recalled that $R = |\mathbf{R}| = |\mathbf{r} - \mathbf{r}'|$, hence

$$\nabla \times \vec{\mathbf{G}}_i(\mathbf{r}, \mathbf{r}') = -\nabla' \times \vec{\mathbf{G}}_i(\mathbf{r}', \mathbf{r}). \quad (2.57)$$

Inserting Eq. (2.57) into the reciprocity condition in Eq. (2.51), yields

$$\begin{aligned} \mathbf{M}_{s,i}(\mathbf{r}) \cdot (\nabla \times \vec{\mathbf{G}}_i(\mathbf{r}, \mathbf{r}')) &= (\nabla' \times \vec{\mathbf{G}}_i(\mathbf{r}', \mathbf{r})) \cdot \mathbf{M}_{s,i}(\mathbf{r}) \\ &= -(\nabla \times \vec{\mathbf{G}}_i(\mathbf{r}, \mathbf{r}')) \cdot \mathbf{M}_{s,i}(\mathbf{r}), \end{aligned} \quad (2.58)$$

which allows for Eq. (2.56) to be rewritten as

$$\mathbf{E}(\mathbf{r}) = \mathbf{E}_{0,i}(\mathbf{r}) + i\omega\mu_0 \oint_{\partial\Omega_i} \vec{\mathbf{G}}_i(\mathbf{r}, \mathbf{r}') \cdot \mathbf{J}_{s,i}(\mathbf{r}') d^2r' - \oint_{\partial\Omega_i} \nabla \times \vec{\mathbf{G}}_i(\mathbf{r}, \mathbf{r}') \cdot \mathbf{M}_{s,i}(\mathbf{r}') d^2r', \quad (2.59)$$

which is known as the surface integral equation for the electric field.

2.3.1.1 Green's Function Surface Integral Equations for a Scatterer Embedded in a Homogeneous Region

For a dielectric or metal scatterer that is not a PEC, (or a *perfect magnetic conductor*, PMC), the tangential electric- and magnetic field must be continuous across the surface of the scatterer. The electric and magnetic currents will therefore be identical on both sides of the scatterer surface, hence for convenience Eq. (2.55a) and Eq. (2.55b) can be redefined in terms of only one of the surface normal vectors, in this case the outward normal vector, leading to $\mathbf{J}_{s,i}$ being replaced by \mathbf{J}_s , and $\mathbf{M}_{s,i}$ being replaced by \mathbf{M}_s . While this change does not affect Eq. (2.55a) and Eq. (2.55b) outside the scatterer, it leads to a change in signs inside the scatterer, due to the opposite sign of $\hat{\mathbf{n}}$.

Furthermore it can be shown that the integrals on the RHS in Eq. (2.59) vanishes when integrating over the spherical surface denoted by $S_{1,\infty}$ in Fig. 2.2 due to the Green's tensor satisfying the radiating boundary condition, as briefly described in Sec. 2.2.2. Lastly it should be noted that, as can be seen in Fig. 2.2, an incident field will only be present in region Ω_1 , hence $\mathbf{E}_{0,2} = 0$ and $\mathbf{E}_{0,1}$ will therefore be replaced by \mathbf{E}_0 .

From Eq. (2.59) it can then be seen that the electric field outside the scatterer in a homogeneous medium at position $\mathbf{r} \in \Omega_1$, is given by the integral over the outer surface of the scatterer, denoted as S_1 in Fig. 2.2, hence

$$\mathbf{E}(\mathbf{r}) = \mathbf{E}_0(\mathbf{r}) + i\omega\mu_0 \oint_{S_1} \vec{\mathbf{G}}_1(\mathbf{r}, \mathbf{r}') \cdot \mathbf{J}_s(\mathbf{r}') d^2r' - \oint_{S_1} \nabla \times \vec{\mathbf{G}}_1(\mathbf{r}, \mathbf{r}') \cdot \mathbf{M}_s(\mathbf{r}') d^2r', \quad (2.60)$$

while the electric field inside the scatterer at position $\mathbf{r} \in \Omega_2$, is given by the integral over the inner surface of the scatterer, denoted as S_2 , yielding

$$\mathbf{E}(\mathbf{r}) = -i\omega\mu_0 \oint_{S_2} \vec{\mathbf{G}}_2(\mathbf{r}, \mathbf{r}') \cdot \mathbf{J}_s(\mathbf{r}') d^2r' + \oint_{S_2} \nabla \times \vec{\mathbf{G}}_2(\mathbf{r}, \mathbf{r}') \cdot \mathbf{M}_s(\mathbf{r}') d^2r'. \quad (2.61)$$

The electric- and magnetic surface currents on the surface of the scatterer are equal to the ones inside the scatterer, and are therefore given by

$$\mathbf{J}_s(\mathbf{r}) = \hat{\mathbf{n}} \times \mathbf{H}(\mathbf{r}), \quad \mathbf{r} \text{ on scatterer surface}, \quad (2.62a)$$

$$\mathbf{M}_s(\mathbf{r}) = -\hat{\mathbf{n}} \times \mathbf{E}(\mathbf{r}), \quad \mathbf{r} \text{ on scatterer surface}, \quad (2.62b)$$

where $\hat{\mathbf{n}}$, once again, is the surface normal vector pointing into Ω_1 , which in Fig. 2.2 is denoted as $\hat{\mathbf{n}}_2$.

By letting the position \mathbf{r} approach the scatterer surface from both sides, the surface currents can be obtained from Eq. (2.60) and Eq. (2.61), which leads to the electric field integral equations

outside and inside the scatterer respectively

$$-\mathbf{M}_s(\mathbf{r}) = \hat{\mathbf{n}} \times \mathbf{E}_0(\mathbf{r}) + i\omega\mu_0 \oint_{S_1} [\hat{\mathbf{n}} \times \overleftrightarrow{\mathbf{G}}_1(\mathbf{r}, \mathbf{r}') \cdot \mathbf{J}_s(\mathbf{r}') d^2r' - \oint_{S_1} [\hat{\mathbf{n}} \times \overleftrightarrow{\mathbf{G}}_1(\mathbf{r}, \mathbf{r}') \cdot \mathbf{M}_s(\mathbf{r}') d^2r',$$

\mathbf{r} infinitesimally outside scatterer surface, (2.63a)

$$-\mathbf{M}_s(\mathbf{r}) = -i\omega\mu_0 \oint_{S_1} [\hat{\mathbf{n}} \times \overleftrightarrow{\mathbf{G}}_1(\mathbf{r}, \mathbf{r}') \cdot \mathbf{J}_s(\mathbf{r}') d^2r' + \oint_{S_1} [\hat{\mathbf{n}} \times \overleftrightarrow{\mathbf{G}}_1(\mathbf{r}, \mathbf{r}') \cdot \mathbf{M}_s(\mathbf{r}') d^2r',$$

\mathbf{r} infinitesimally inside scatterer surface. (2.63b)

Similar expressions can be found using the magnetic field by applying Eq. (2.2c), however, this will only be shown for a PEC in Sec. 2.3.1.2.

2.3.1.2 Derivation of the Surface Current for a Perfect Electric Conductor Using the Magnetic Field Integral Equation

Up until this point a scatterer that is not a PEC has been considered, however, if it is a PEC, as is the case for terahertz antennas, the electric- and the magnetic field are both zero just inside the surface of the scatterer, and all the way through, causing the tangential component of $\mathbf{E}(\mathbf{r})$ to vanish, which leads to Eq. (2.63a) being equal to Eq. (2.63b), hence $\mathbf{M}_s = \mathbf{0}$. Eq. (2.60) therefore reduces to

$$\mathbf{E}(\mathbf{r}) = \mathbf{E}_0(\mathbf{r}) + i\omega\mu_0 \oint_{S_1} \overleftrightarrow{\mathbf{G}}_1(\mathbf{r}, \mathbf{r}') \cdot \mathbf{J}_s(\mathbf{r}') d^2r', \quad (2.64)$$

which is known as the *electric field integral equation*, or EFIE, while Eq. (2.61) becomes irrelevant. Thus, from this point on it will be implicit that the integral is over S_1 .

In Eq. (2.62a) it can be seen that the electric surface current is defined using the magnetic field, and Eq. (2.2c) should therefore be applied to Eq. (2.64) in order to obtain the *magnetic field integral equation*, or MFIE,

$$\mathbf{H}(\mathbf{r}) = \mathbf{H}_0(\mathbf{r}) + \oint \nabla \times \left(\overleftrightarrow{\mathbf{G}}_1(\mathbf{r}, \mathbf{r}') \cdot \mathbf{J}_s(\mathbf{r}') \right) d^2r', \quad (2.65)$$

which has been multiplied by $\frac{1}{i\omega\mu_0}$. This expression can then be written in terms of $\mathbf{J}_s(\mathbf{r})$ by using Eq. (2.62a), yielding

$$\mathbf{J}_s(\mathbf{r}) = \mathbf{J}_0(\mathbf{r}) + \oint \hat{\mathbf{n}} \times \nabla \times \overleftrightarrow{\mathbf{G}}_1(\mathbf{r}, \mathbf{r}') \cdot \mathbf{J}_s(\mathbf{r}') d^2r', \quad (2.66)$$

which can be further rewritten using that $\nabla \times \overleftrightarrow{\mathbf{G}}_1(\mathbf{r}, \mathbf{r}') = \nabla \times \overleftrightarrow{\mathbf{I}}_1 g(\mathbf{r}, \mathbf{r}')$ from Eq. (2.27), along with $\nabla \times (\overleftrightarrow{\mathbf{I}}_1 g(\mathbf{r}, \mathbf{r}') \mathbf{J}_s(\mathbf{r}')) = \nabla g(\mathbf{r}, \mathbf{r}') \times \mathbf{J}_s(\mathbf{r}')$ due to ∇ only affecting the unmarked coordinates and $g(\mathbf{r}, \mathbf{r}')$ being a scalar. This leads to Eq. (2.66) being expressed as

$$\mathbf{J}_s(\mathbf{r}) = \mathbf{J}_0(\mathbf{r}) + \oint \hat{\mathbf{n}} \times (\nabla g(\mathbf{r}, \mathbf{r}') \times \mathbf{J}_s(\mathbf{r}')) d^2r', \quad (2.67)$$

which can then again be rewritten by the vector identity $\mathbf{A} \times (\mathbf{B} \times \mathbf{C}) = \mathbf{B}(\mathbf{A} \cdot \mathbf{C}) - \mathbf{C}(\mathbf{A} \cdot \mathbf{B})$ as

$$\mathbf{J}_s(\mathbf{r}) = \mathbf{J}_0(\mathbf{r}) + \oint (\nabla g(\mathbf{r}, \mathbf{r}') [\hat{\mathbf{n}} \cdot \mathbf{J}_s(\mathbf{r}')] - \mathbf{J}_s(\mathbf{r}') [\hat{\mathbf{n}} \cdot \nabla g(\mathbf{r}, \mathbf{r}')]) d^2r'. \quad (2.68)$$

If then the expression for $g(\mathbf{r}, \mathbf{r}')$ from Eq. (2.19) is inserted the integrand can be found to be

$$\left(ik_0 \sqrt{\varepsilon} - \frac{1}{R} \right) \frac{e^{ik_0 \sqrt{\varepsilon} R}}{4\pi R} \left(\frac{\mathbf{R}}{R} [\hat{\mathbf{n}} \cdot \mathbf{J}_s(\mathbf{r}')] - \mathbf{J}_s(\mathbf{r}') \left[\hat{\mathbf{n}} \cdot \frac{\mathbf{R}}{R} \right] \right), \quad (2.69)$$

where it has been used that $\nabla R = \frac{\mathbf{R}}{R}$, as was the case in Sec. 2.2.2.1.

In order to then evaluate the scalar products, when the surface and the surface current density are smooth, $\mathbf{J}_s(\mathbf{r}')$ and $\frac{\mathbf{R}}{R}$ in the first and second term respectively can be Taylor expanded on the surface with respect to \mathbf{R} . This leads to 0th order terms orthogonal to $\hat{\mathbf{n}}$, hence the scalar product vanishes for these terms, leaving the most divergent terms proportional to $\frac{1}{R}$. Fortunately, the integral in Eq. (2.68) yields a finite contribution as in the limit $R \rightarrow 0$ the contribution from an arbitrarily small circle around the singularity is bounded. However, in this case, the term proportional to $\frac{1}{R^2} \frac{\mathbf{R}}{R} [\hat{\mathbf{n}} \cdot \mathbf{J}_s(\mathbf{r}')] vanishes as the opposite points on the circle will cancel each other for a smooth surface, though this is not the case for the other term. This term may be written as$

$$\begin{aligned} \frac{e^{ik_0 \sqrt{\varepsilon} R}}{4\pi R^2} \mathbf{J}_s(\mathbf{r}') \left[\hat{\mathbf{n}} \cdot \frac{\mathbf{R}}{R} \right] &= \frac{e^{ik_0 \sqrt{\varepsilon} R}}{4\pi a^2 2(1 - \cos \theta)} \mathbf{J}_s(\mathbf{r}') \left[\hat{\mathbf{r}} \cdot \frac{a(1 - \cos \theta) \hat{\mathbf{r}} + a \sin \theta \hat{\mathbf{p}}}{a\sqrt{2(1 - \cos \theta)}} \right] \\ &= \frac{e^{ik_0 \sqrt{\varepsilon} R}}{4\pi a^2 2^{3/2} \sqrt{1 - \cos \theta}} \mathbf{J}_s(\mathbf{r}'), \end{aligned} \quad (2.70)$$

where it has been used that $\mathbf{R} = a(1 - \cos \theta) \hat{\mathbf{r}} + a \sin \theta \hat{\mathbf{p}}$ and $R = a\sqrt{2(1 - \cos \theta)}$ for a sphere with radius a such that $\mathbf{r} = a \hat{\mathbf{r}}$ and $\mathbf{r}' = a \cos \theta \hat{\mathbf{r}} + a \sin \theta \hat{\mathbf{p}}$, where $\hat{\mathbf{n}} = \frac{\mathbf{r}}{|\mathbf{r}|}$ and $\hat{\mathbf{n}} \cdot \hat{\mathbf{p}} = 0$. An illustration of the connection between \mathbf{r} , \mathbf{r}' and θ can be seen in Fig. 2.3.

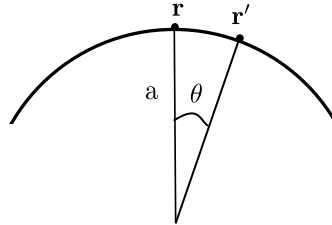


Figure 2.3: Illustration of the points \mathbf{r} and \mathbf{r}' with the angle θ between them.

In the vicinity of the singularity Eq. (2.70) reduces to

$$\lim_{\mathbf{r}' \rightarrow \mathbf{r}} \frac{e^{ik_0 \sqrt{\varepsilon} R}}{4\pi a^2 2^{3/2} \sqrt{1 - \cos \theta}} \mathbf{J}_s(\mathbf{r}') = \frac{1}{8\pi \theta a^2} \mathbf{J}_s(\mathbf{r}), \quad (2.71)$$

where $\cos \theta$ has been Taylor expanded to the 2nd order. When integrating this over a small circle around the singularity, using a fixed θ , a radial density can be found to be $\frac{\mathbf{J}_s(\mathbf{r})}{4a}$, which at the limit infinitely close to the singularity is constant, so this contribution from the singularity is not significant, and will thus be ignored.

Finally, one should consider that \mathbf{r}' is chosen infinitesimally outside the scatterer, such that the function is defined when \mathbf{r}' approaches \mathbf{r} , in which case $\hat{\mathbf{n}} \cdot \frac{\mathbf{R}}{R}$ is nonzero. If instead of integrating around the singularity one integrates over it, then the integral over the LHS in Eq. (2.70) can be

written as

$$\int_{\lim_{\mathbf{r}' \rightarrow \mathbf{r}}} \frac{e^{ik_0 \sqrt{\epsilon} R}}{4\pi R^2} \mathbf{J}_s(\mathbf{r}') \left[\hat{\mathbf{n}} \cdot \frac{\mathbf{R}}{R} \right] d^2 r', \quad (2.72)$$

where $\frac{1}{R^2} \hat{\mathbf{n}} \cdot \frac{\mathbf{R}}{R} d^2 r' = d\Omega$ corresponds to a projection onto a unit sphere, leading to the integral being rewritten in terms of the solid angle as

$$\frac{1}{4\pi} \int_{\lim_{\mathbf{r}' \rightarrow \mathbf{r}}} \mathbf{J}_s(\mathbf{r}) d\Omega. \quad (2.73)$$

Integrating over an infinitesimally small area, in which the singularity is located, corresponds to integrating over a half sphere, as \mathbf{r}' is infinitesimally close to the surface of the scatterer. The integral in Eq. (2.73) therefore becomes

$$\frac{1}{4\pi} \int_0^{\pi/2} \int_0^{2\pi} \sin \theta \mathbf{J}_s(\mathbf{r}) d\theta d\varphi = \frac{1}{2} \mathbf{J}_s(\mathbf{r}). \quad (2.74)$$

This contribution from the singularity may then be subtracted from the original expression in Eq. (2.68) yielding

$$\frac{1}{2} \mathbf{J}_s(\mathbf{r}) = \mathbf{J}_0(\mathbf{r}) + \int (\nabla g(\mathbf{r}, \mathbf{r}') [\hat{\mathbf{n}} \cdot \mathbf{J}_s(\mathbf{r}')] - \mathbf{J}_s(\mathbf{r}') [\hat{\mathbf{n}} \cdot \nabla g(\mathbf{r}, \mathbf{r}')]) d^2 r', \quad (2.75)$$

where the integral is over the entire scatterer surface, as in Eq. (2.68), with the exception of the singularity.

The result in Eq. (2.75) can now be utilised to model the surface current of a scatterer particle in a homogeneous medium, e.g. a vacuum. The implementation and the numerical solving of these integrals is explained in depth in Sec. 3.2.

2.4 Layered Structure

The content and derivations within this section are based on [15, Sec. 6.3].

In Fig. 2.1 the structure of interest throughout this report was shown as multiple scatterers on top of an infinite substrate, however, since Sec. 2.2 and Sec. 2.3 only considered a structure with a scatterer in a homogeneous media, a scatterer on top of an infinite substrate has yet to be discussed, which is therefore the aim of this section. Due to the small size of the terahertz antenna, it is likely to be integrated on the surface of a substrate, which e.g. is the case for a PCA, hence why the substrate must be taken into account for the scattering problem.

2.4.1 Green's Function For a Layered Structure

The scalar Green's function that satisfies the radiating boundary condition and the dyadic Green's tensor in a homogeneous media were in Sec. 2.2.2 found in Cartesian coordinates, and can be

recalled from Eq. (2.19) and Eq. (2.27), respectively, as

$$g(\mathbf{r}, \mathbf{r}') = \frac{e^{ik_0\sqrt{\varepsilon}|\mathbf{r}-\mathbf{r}'|}}{4\pi|\mathbf{r}-\mathbf{r}'|},$$

$$\vec{\mathbf{G}}(\mathbf{r}, \mathbf{r}') = \left(\vec{\mathbf{I}} + \frac{1}{k_0^2\varepsilon}\nabla\nabla \right) g(\mathbf{r}, \mathbf{r}').$$

In the case of a homogeneous medium Cartesian coordinates suffice, however, in the case of a second substrate the calculations can be simplified by using cylindrical coordinates instead. The reason for this is that the wave number does not depend on its orientation within the xy plane, hence an integral in Cartesian coordinates over both k_x and k_y can be replaced by a single integral over k_ρ in cylindrical coordinates. In order to find $g(\mathbf{r}, \mathbf{r}')$ in cylindrical coordinates it should first be expressed as a plane-wave-expansion, which, using the Weyl expansion, yields[15, Eq. 6.53]

$$g(\mathbf{r}, \mathbf{r}') = \frac{i}{2} \frac{1}{(2\pi)^2} \int_{-\infty}^{\infty} \int_{-\infty}^{\infty} \frac{e^{ik_x(x-x')} e^{ik_y(y-y')} e^{ik_{z,1}|z-z'|}}{k_{z,1}} dk_x dk_y, \quad (2.76)$$

where $k_{z,1} = \sqrt{k_1^2 - k_\rho^2}$, $k_1 = k_0\sqrt{\varepsilon_1}$ and $k_\rho = \sqrt{k_x^2 + k_y^2}$. How this expression is derived can be found in App. B, where this expression is written in Eq. (B.7).

This can then be converted into cylindrical coordinates, and thereafter reduced by using the 0th order Bessel function, yielding

$$g(\mathbf{r}, \mathbf{r}') = \frac{i}{4\pi} \int_0^\infty \frac{\mathcal{J}_0(k_\rho\rho_r) e^{ik_{z,1}|z-z'|}}{k_{z,1}} k_\rho dk_\rho. \quad (2.77)$$

By then inserting this into the expression for the direct dyadic Green's tensor in free space and applying the relations between Cartesian and cylindrical coordinates for the unit vectors, the direct dyadic Green's tensor can be found to be

$$\begin{aligned} \vec{\mathbf{G}}^{(d)}(\mathbf{r}, \mathbf{r}') = & \frac{i}{4\pi} \int_0^\infty \left[\hat{\boldsymbol{\rho}}_r \hat{\boldsymbol{\rho}}_r \left(\mathcal{J}_0(k_\rho\rho_r) + \frac{k_\rho^2}{k_1^2} \mathcal{J}_0''(k_\rho\rho_r) \right) + (\hat{\mathbf{z}}\hat{\boldsymbol{\rho}}_r + \hat{\boldsymbol{\rho}}_r\hat{\mathbf{z}}) \frac{ik_{z,1}k_\rho}{k_1^2} \frac{z-z'}{|z-z'|} \mathcal{J}_0'(k_\rho\rho_r) \right. \\ & \left. + \hat{\mathbf{z}}\hat{\mathbf{z}} \frac{k_\rho^2}{k_1^2} \mathcal{J}_0(k_\rho\rho_r) + \hat{\boldsymbol{\varphi}}_r \hat{\boldsymbol{\varphi}}_r \left(\mathcal{J}_0(k_\rho\rho_r) + \frac{k_\rho^2}{k_1^2} \frac{\mathcal{J}_0'(k_\rho\rho_r)}{k_\rho\rho_r} \right) \right] e^{ik_{z,1}|z-z'|} \frac{k_\rho}{k_{z,1}} dk_\rho, \quad (2.78) \end{aligned}$$

where k_ρ , φ_k , ρ_r and φ_r are defined such that

$$k_x = k_\rho \cos \varphi_k, \quad k_y = k_\rho \sin \varphi_k,$$

$$x - x' = \rho_r \cos \varphi_r, \quad y - y' = \rho_r \sin \varphi_r,$$

while

$$\hat{\boldsymbol{\rho}}_r = \hat{\mathbf{x}} \cos \varphi_r + \hat{\mathbf{y}} \sin \varphi_r,$$

$$\hat{\boldsymbol{\varphi}}_r = -\hat{\mathbf{x}} \sin \varphi_r + \hat{\mathbf{y}} \cos \varphi_r.$$

By then assuming that the interface between the homogeneous media and the infinite substrate is in $z = 0$ one can find the incoming, the reflected and the transmitted electric field. This is done by taking the scalar products of the direct Green's tensor with the unit vectors and then dividing the field contributions into s- and p-polarisation for which the corresponding reflected and transmitted

field contributions are determined with the Fresnel equations. Finally, the Green's tensors in reflected and transmitted form are reassembled by adding the corresponding unit vector that was initially used. These will respectively be referred to as the indirect and the transmitted Green's tensors and are given as

$$\begin{aligned} \vec{\mathbf{G}}^{(i)}(\mathbf{r}, \mathbf{r}') = & \frac{i}{4\pi} \int_0^\infty \left\{ r^{(p)}(k_\rho) \left(\hat{\mathbf{z}}\hat{\mathbf{z}}\mathcal{J}_0(k_\rho\rho_r) \frac{k_\rho^2}{k_1^2} + \hat{\varphi}_r\hat{\varphi}_r \frac{\mathcal{J}'_0(k_\rho\rho_r)}{k_\rho\rho_r} \frac{k_{z,1}^2}{k_1^2} + \right. \right. \\ & \left. \left. \hat{\rho}_r\hat{\rho}_r\mathcal{J}_0''(k_\rho\rho_r) \frac{k_{z,1}^2}{k_1^2} - (\hat{\mathbf{z}}\hat{\rho}_r - \hat{\rho}_r\hat{\mathbf{z}}) \frac{ik_\rho k_{z,1}}{k_1^2} \mathcal{J}'_0(k_\rho\rho_r) \right) \right. \\ & \left. - r^{(s)}(k_\rho) \left(\hat{\varphi}_r\hat{\varphi}_r\mathcal{J}_0''(k_\rho\rho_r) + \hat{\rho}_r\hat{\rho}_r \frac{\mathcal{J}'_0(k_\rho\rho_r)}{k_\rho\rho_r} \right) \right\} e^{ik_{z,1}(z+z')} \frac{k_\rho}{k_{z,1}} dk_\rho, \end{aligned} \quad (2.79a)$$

$$\begin{aligned} \vec{\mathbf{G}}^{(t)}(\mathbf{r}, \mathbf{r}') = & \frac{i}{4\pi} \int_0^\infty \left\{ t^{(p)}(k_\rho) \frac{\varepsilon_1}{\varepsilon_2} \left(\hat{\mathbf{z}}\hat{\mathbf{z}}\mathcal{J}_0(k_\rho\rho_r) \frac{k_\rho^2}{k_1^2} - \hat{\varphi}_r\hat{\varphi}_r \frac{\mathcal{J}'_0(k_\rho\rho_r)}{k_\rho\rho_r} \frac{k_{z,1}k_{z,3}}{k_1^2} \right. \right. \\ & \left. \left. - \hat{\rho}_r\hat{\rho}_r\mathcal{J}_0''(k_\rho\rho_r) \frac{k_{z,1}k_{z,3}}{k_1^2} - \left(\hat{\mathbf{z}}\hat{\rho}_r + \hat{\rho}_r\hat{\mathbf{z}} \frac{k_{z,3}}{k_{z,1}} \right) i \frac{k_\rho k_{z,1}}{k_{z,1}^2} \mathcal{J}'_0(k_\rho\rho_r) \right) \right. \\ & \left. - t^{(s)}(k_\rho) \left(\hat{\varphi}_r\hat{\varphi}_r\mathcal{J}_0''(k_\rho\rho_r) + \hat{\rho}_r\hat{\rho}_r \frac{\mathcal{J}'_0(k_\rho\rho_r)}{k_\rho\rho_r} \right) \right\} e^{ik_{z,1}z'} e^{-ik_{z,3}z} \frac{k_\rho}{k_{z,1}} dk_\rho. \end{aligned} \quad (2.79b)$$

A more in-depth derivation of these expressions can be found in App. C, with an outset in Eq. (2.76).

2.4.2 The Far-Field Green's Tensor

As was the case for a homogeneous media it is essential to be able to find the far-field radiation patterns and the DSCS for a layered structure. In order to calculate these, the far-field Green's tensor is needed, which will thus be derived with an outset in the indirect and the transmitted Green's tensor in Eq. (2.79).

First, consider the zz -component of the indirect Green's tensor. In the far-field, z is very large and thus the integration interval can be reduced to $0 \leq k_\rho \leq k_1$, as if $k_\rho > k_1$ then $k_{z,1}$ must be completely imaginary, since $k_1^2 = k_{z,1}^2 + k_\rho^2$, and the exponential term will go to zero and terminate the integral. By then converting the coordinates into spherical coordinates, and using the Bessel function for large input arguments the integral variable may be substituted for the angle α where $k_{z,1} = k_1 \cos \alpha$ and $k_\rho = k_1 \sin \alpha$. It is then found that the only contributions from the integral are for $\alpha \approx \theta$ or $\alpha + \theta \approx \pi$ due to fast variations of a complex exponent. The exponent may resultingly be Taylor expanded, such that the integral may be determined analytically resulting in

$$\mathbf{G}_{zz}^{(i,ff)} = \frac{e^{ik_1 r}}{4\pi r} e^{-ik_\rho \mathbf{r}' \cdot \hat{\rho}} e^{ik_{z,1} z'} r^{(p)}(k_\rho) \frac{k_\rho^2}{k_1^2}. \quad (2.80)$$

Now the indirect far-field Green's tensor can be obtained from Eq. (2.79a) by using that $\hat{\varphi}_r \approx \hat{\varphi}$ and $\hat{\rho}_r \approx \hat{\rho}$ in the limit of far-field. The $\hat{\varphi}_r\hat{\varphi}_r$ term from the p-polarised part of the indirect Green's tensor and the $\hat{\rho}_r\hat{\rho}_r$ term from the s-polarised part vanishes faster than $\frac{1}{\rho}$ in the far-field

since they go as $\frac{1}{\rho^{3/2}}$, while the remaining terms can be approximated in a similar fashion as the zz -component stated above. Thus the indirect far-field Green's tensor can be expressed as

$$\mathbf{G}^{(i,ff)}(\mathbf{r}, \mathbf{r}') = \frac{e^{ik_1 r}}{4\pi r} e^{-ik_\rho \hat{\boldsymbol{\rho}} \cdot \mathbf{r}'} e^{ik_{z,1} z'} \left(r^{(s)}(k_\rho) \hat{\boldsymbol{\varphi}} \hat{\boldsymbol{\varphi}} - r^{(p)}(k_\rho) \hat{\boldsymbol{\theta}} \left(\hat{\mathbf{z}} \frac{k_\rho}{k_1} + \hat{\boldsymbol{\rho}} \frac{k_{z,1}}{k_1} \right) \right), \quad (2.81)$$

where $k_\rho = k_1 \sin \theta$ and $k_{z,1} = k_1 \cos \theta$.

For the transmitted Green's tensor a far-field approximation can be found by a similar approach, where the integration interval in Eq. (2.79b) is reduced to $0 \leq k_\rho \leq k_3$, where $k_3 = k_0 \sqrt{\varepsilon_3}$, as the integrand, once again, will vanish for $k_\rho > k_3$ when $z \ll 0$, due to the exponential term. This yields the expression for the far-field transmitted Green's tensor,

$$\begin{aligned} \overleftrightarrow{\mathbf{G}}^{(t,ff)}(\mathbf{r}, \mathbf{r}') &= \frac{e^{ik_3 r}}{4\pi r} e^{-ik_\rho \hat{\boldsymbol{\rho}} \cdot \mathbf{r}'} e^{ik_{z,1} z'} \frac{k_{z,3}}{k_{z,1}} \left(t^{(s)}(k_\rho) \hat{\boldsymbol{\varphi}} \hat{\boldsymbol{\varphi}} + \right. \\ &\quad \left. t_{1,3}^{(p)}(k_\rho) \frac{\varepsilon_1}{\varepsilon_3} \left[\hat{\mathbf{z}} \hat{\mathbf{z}} \frac{k_\rho^2}{k_1^2} + \hat{\boldsymbol{\rho}} \hat{\boldsymbol{\rho}} \frac{k_{z,1} k_{z,3}}{k_1^2} + \left(\hat{\mathbf{z}} \hat{\boldsymbol{\rho}} + \hat{\boldsymbol{\rho}} \hat{\mathbf{z}} \frac{k_{z,3}}{k_{z,1}} \right) \frac{k_{z,1} k_\rho}{k_1^2} \right] \right). \end{aligned} \quad (2.82)$$

Like what was the case for the derivation of the Green's tensors in Sec. 2.4.1, a more in-depth derivation of the far-field Green's tensors can be found in App. C.1.

2.4.3 The Magnetic Field Integral Equation for a Layered Structure

For a layered structure, the MFIE for a scatterer in a homogeneous media in Eq. (2.66) can be restated with the inclusion of the indirect Green's tensor for the electric field from Eq. (2.79a) as

$$\mathbf{J}_s(\mathbf{r}) = \mathbf{J}_0(\mathbf{r}) + \oint \hat{\mathbf{n}} \times \nabla \times \left(\overleftrightarrow{\mathbf{G}}^{(d)}(\mathbf{r}, \mathbf{r}') + \overleftrightarrow{\mathbf{G}}^{(i)}(\mathbf{r}, \mathbf{r}') \right) \cdot \mathbf{J}_s(\mathbf{r}') d^2 r', \quad (2.83)$$

which, as previously done in Sec. 2.3.1.2, may be rewritten in order to obtain an expression similar to Eq. (2.68), hence

$$\begin{aligned} \mathbf{J}_s &= \mathbf{J}_0(\mathbf{r}) + \oint \left\{ \nabla g(\mathbf{r}, \mathbf{r}') [\hat{\mathbf{n}} \cdot \mathbf{J}_s(\mathbf{r}')] - \mathbf{J}_s(\mathbf{r}') [\hat{\mathbf{n}} \cdot \nabla g(\mathbf{r}, \mathbf{r}')] \right. \\ &\quad \left. + \hat{\mathbf{n}} \times \nabla \times \overleftrightarrow{\mathbf{G}}^{(i)}(\mathbf{r}, \mathbf{r}') \cdot \mathbf{J}_s(\mathbf{r}') \right\} d^2 r'. \end{aligned} \quad (2.84)$$

In order to evaluate this, one has to find the curl of the indirect Green's tensor, which has been done in App. C.2, where it in Eq. (C.42) was found that

$$\begin{aligned} \nabla \times \mathbf{G}^{(i)} &= \frac{i}{4\pi} \int_0^\infty \left(r^{(s)}(k_\rho) \left\{ -k_\rho \mathcal{J}'_0(k_\rho \rho_r) \hat{\mathbf{z}} \hat{\boldsymbol{\varphi}}_r - ik_{z,1} \mathcal{J}''_0(k_\rho \rho_r) \hat{\boldsymbol{\rho}}_r \hat{\boldsymbol{\varphi}}_r + ik_{z,1} \frac{\mathcal{J}'_0(k_\rho \rho_r)}{k_\rho \rho_r} \hat{\boldsymbol{\varphi}}_r \hat{\boldsymbol{\rho}}_r \right\} \right. \\ &\quad \left. + r^{(p)}(k_\rho) \left\{ -k_\rho \mathcal{J}'_0(k_\rho \rho_r) \hat{\boldsymbol{\varphi}}_r \hat{\mathbf{z}} - ik_{z,1} \frac{\mathcal{J}'_0(k_\rho \rho_r)}{k_\rho \rho_r} \hat{\boldsymbol{\rho}}_r \hat{\boldsymbol{\varphi}}_r + ik_{z,1} \mathcal{J}''_0(k_\rho \rho_r) \hat{\boldsymbol{\varphi}}_r \hat{\boldsymbol{\rho}}_r \right\} \right) \\ &\quad \times e^{ik_{z,1}(z+z')} \frac{k_\rho}{k_{z,1}} dk_\rho. \end{aligned} \quad (2.85)$$

2.4.3.1 Evaluation of Singularities

The asymptotic behaviour of the integrand in Eq. (2.85) when $k_\rho \rightarrow \infty$ will now be examined using the asymptotic expansion of the Bessel function[15, Eq. C.8]

$$J_m(x) \rightarrow \sqrt{\frac{2}{\pi x}} \cos\left(x - \frac{m\pi}{2} - \frac{\pi}{4}\right), \quad x \rightarrow \infty, \quad (2.86)$$

which has the upper boundary of $\sqrt{\frac{2}{\pi x}}$ for all m . The Fresnel reflection coefficients in the limit of $k_\rho \rightarrow \infty$ then go as

$$r^{(s)}(k_\rho) = \frac{k_{z,1} - k_{z,3}}{k_{z,1} + k_{z,3}} \rightarrow \frac{-\frac{1}{2} \frac{k_0^2}{k_\rho^2} (\varepsilon_1 - \varepsilon_3)}{2 - \frac{1}{2} \frac{k_0^2}{k_\rho^2} (\varepsilon_1 + \varepsilon_3)} \rightarrow \frac{k_0^2 (\varepsilon_3 - \varepsilon_1)}{4k_\rho^2}, \quad (2.87a)$$

$$r^{(p)}(k_\rho) = \frac{\varepsilon_3 k_{z,1} - \varepsilon_1 k_{z,3}}{\varepsilon_3 k_{z,1} + \varepsilon_1 k_{z,3}} \rightarrow \frac{\varepsilon_3 - \varepsilon_1}{\varepsilon_3 + \varepsilon_1}, \quad (2.87b)$$

where it has been used that

$$k_{z,i} = \sqrt{k_0^2 \varepsilon_i - k_\rho^2} \rightarrow ik_\rho \left(1 - \frac{1}{2} \frac{k_0^2 \varepsilon_i}{k_\rho^2}\right), \quad (2.88)$$

which has been obtained by using a Taylor expansion. This Taylor expansion can furthermore be used to find that the exponential term in Eq. (2.85) in this limit will go as $e^{-k_\rho(z+z')}$. This causes the integral to go to zero as the remaining factors of the integrand only goes as powers of k_ρ , hence the exponent dominates. However, this does not hold if $z + z' = 0$, in which case it will be determined whether the integral is bounded, which is equivalent to examine whether the tails of the integral at $k_\rho \rightarrow \infty$ is bounded as the integrand itself is bounded. In the case where it is not bounded it will lead to a singularity which has to be accounted for in order to avoid errors in the numerical evaluations of the integral.

By using the identity[17, p. 160, Eq. 27.90]

$$\int_0^\infty \mathcal{J}_n(bx) e^{-ax} dx = \frac{(\sqrt{a^2 + b^2} - a)^n}{b^n \sqrt{a^2 + b^2}}, \quad (2.89)$$

for $n \geq 0$, the integrals may be approximated by using the results for the limit $k_\rho \gg k_0$ throughout the entire integration interval in order to capture the singular behaviour of the tails of the integrals. By inserting the expressions for the reflection coefficients from Eq. (2.87), the s-polarised $\hat{\mathbf{z}}\hat{\varphi}_r$ component is seen to go as

$$\int_0^\infty \frac{\mathcal{J}_0'(k_\rho \rho_r)}{k_\rho} e^{-k_\rho(z+z')} dk_\rho = \int_{0^+}^{\rho_r} \int_0^\infty \mathcal{J}_0''(k_\rho \rho_r') e^{-k_\rho(z+z')} dk_\rho d\rho_r', \quad (2.90)$$

which can be found by differentiating and integrating with respects to ρ_r , where the limits used in the integral ensures that the upper limit yields the expression on the LHS, while the lower limit

yields 0, since $\mathcal{J}'_0(0) = 0$. This can then be rewritten using Eq. (C.37b) and Eq. (2.89), yielding

$$\begin{aligned}
LHS &= \frac{1}{2} \int_{0^+}^{\rho_r} \int_0^\infty (\mathcal{J}_2(k_\rho \rho'_r) - \mathcal{J}_0(k_\rho \rho'_r)) e^{-k_\rho(z+z')} dk_\rho d\rho'_r \\
&= \frac{1}{2} \int_{0^+}^{\rho_r} \left(\frac{(\tilde{R}' - (z+z'))^2}{\rho_r^2 \tilde{R}'} - \frac{1}{\tilde{R}'} \right) d\rho'_r \\
&= -\frac{\tilde{R} - (z+z')}{\rho_r}, \tag{2.91}
\end{aligned}$$

where $\tilde{R} = \sqrt{\rho_r^2 + (z+z')^2}$, while the integral has been solved computationally. From this it can be seen that the integral is discontinuous and bounded when \tilde{R} approaches 0.

For the s-polarised $\hat{\rho}_r \hat{\varphi}_r$ term, a similar procedure is used, where the antiderivative wrt. ρ_r is taken to act as an inverse function to the derivative, where C is an integration constant, due to a singularity as $\tilde{R} \rightarrow 0$, such that

$$\begin{aligned}
\int_0^\infty \frac{\mathcal{J}''_0(k_\rho \rho_r)}{k_\rho} e^{-k_\rho(z+z')} dk_\rho &= \int \int_0^\infty \mathcal{J}'''_0(k_\rho \rho_r) e^{-k_\rho(z+z')} dk_\rho d\rho_r \\
&= \frac{1}{4} \int \int_0^\infty (-\mathcal{J}_3(k_\rho \rho_r) + 3\mathcal{J}_1(k_\rho \rho_r)) e^{-k_\rho(z+z')} dk_\rho d\rho_r \\
&= \frac{1}{4} \int \left(-\frac{(\tilde{R} - (z+z'))^3}{\rho_r^3 \tilde{R}} + 3\frac{\tilde{R} - (z+z')}{\rho_r \tilde{R}'} \right) d\rho_r \\
&= \frac{1}{2} \ln(\tilde{R} + z + z') - \frac{z+z'}{2(\tilde{R} + z + z')} + C, \tag{2.92}
\end{aligned}$$

where the recurrence relation in Eq. (C.38) has been used in order to find an expression for $\mathcal{J}'''_0(k_\rho \rho_r)$. In this case it can be seen that the singularity when $\tilde{R} \rightarrow 0$ is logarithmic.

For the s-polarised $\hat{\varphi}_r \hat{\rho}_r$ term it can, by the same approach as the one used for the s-polarised $\hat{\rho}_r \hat{\varphi}_r$ term, be found that

$$\begin{aligned}
\int_0^\infty \frac{\mathcal{J}'_0(k_\rho \rho_r)}{k_\rho^2 \rho_r} e^{-k_\rho(z+z')} dk_\rho &= -\int_0^\infty \frac{\mathcal{J}_2(k_\rho \rho_r) + \mathcal{J}_0(k_\rho \rho_r)}{2k_\rho} e^{-k_\rho(z+z')} dk_\rho \\
&= \frac{1}{4} \int \int_0^\infty (\mathcal{J}_3(k_\rho \rho_r) + \mathcal{J}_1(k_\rho \rho_r)) e^{-k_\rho(z+z')} dk_\rho d\rho_r \\
&= \frac{1}{2} \ln(\tilde{R} + z + z') + \frac{z+z'}{2(\tilde{R} + z + z')} + C \tag{2.93}
\end{aligned}$$

where an expression for $\frac{\mathcal{J}'_0(k_\rho \rho_r)}{k_\rho \rho_r}$ has been found using Eq. (C.37a) along with the recurrence formula $\mathcal{J}_{m+1}(x) = \frac{2m}{x} \mathcal{J}_m(x) - \mathcal{J}_{m-1}(x)$, while the last integral can be solved with the trigonometric substitution $\rho_r = (z+z') \tan(u)$. Here it can be seen that this term results in a similar singularity as the s-polarised $\hat{\rho}_r \hat{\varphi}_r$ term.

In conclusion, the $\hat{z} \hat{\varphi}_r$ term of the indirect Green's tensor for s-polarisation is almost well behaved with no singularity, however it does contain a discontinuity, while the $\hat{\rho}_r \hat{\varphi}_r$ and $\hat{\varphi}_r \hat{\rho}_r$ term in the limit of $\tilde{R} \rightarrow 0$ go respectively as $\pm \frac{k_0^2(\varepsilon_3 - \varepsilon_1)}{32\pi} \ln(\tilde{R} + z + z')$, when the constants from the indirect Green's tensor and the reflection coefficient for s-polarisation has been taken into account.

Now the terms for p-polarisation are examined, where it is helpful to recall from Eq. (2.87b) that

$r^{(p)}$ does not depend on k_ρ in the limit where $k_\rho \rightarrow \infty$. If first the $\hat{\varphi}_r \hat{\mathbf{z}}$ term is evaluated it can be found that

$$\begin{aligned} \int_0^\infty k_\rho \mathcal{J}'_0(k_\rho \rho_r) e^{-k_\rho(z+z')} dk_\rho &= \frac{\partial}{\partial \rho_r} \int_0^\infty \mathcal{J}_0(k_\rho \rho_r) e^{-k_\rho(z+z')} dk_\rho \\ &= \frac{\partial}{\partial \rho_r} \frac{1}{\tilde{R}} \\ &= -\frac{\rho_r}{\tilde{R}^3}, \end{aligned} \quad (2.94)$$

which includes a singularity for $z + z' = 0$ going as $\frac{1}{\rho_r^2}$.

By a similar procedure, the $\hat{\varphi}_r \hat{\rho}_r$ term is evaluated as

$$\begin{aligned} \int_0^\infty k_\rho \mathcal{J}''_0(k_\rho \rho_r) e^{-k_\rho(z+z')} dk_\rho &= -\frac{\partial}{\partial \rho_r} \int_0^\infty \mathcal{J}_1(k_\rho \rho_r) e^{-k_\rho(z+z')} dk_\rho \\ &= -\frac{\partial}{\partial \rho_r} \frac{\tilde{R} - (z+z')}{\rho_r \tilde{R}} \\ &= \frac{1}{\rho_r^2} \left(1 - \frac{z+z'}{\tilde{R}} \right) - \frac{z+z'}{\tilde{R}^3}, \end{aligned} \quad (2.95)$$

which includes a singularity going as $\frac{1}{\rho_r^2}$ for $z + z' = 0$, as well as a singularity for $\rho_r = 0$ going as $\frac{1}{(z+z')^2}$.

Lastly, the $\hat{\rho}_r \hat{\varphi}_r$ term is evaluated using the defining differential equation for Bessel functions given by (C.40a) for \mathcal{J}_0 such that

$$\begin{aligned} \int_0^\infty k_\rho \frac{\mathcal{J}'_0(k_\rho \rho_r)}{k_\rho \rho_r} e^{-k_\rho(z+z')} dk_\rho &= -\int_0^\infty k_\rho (\mathcal{J}''_0(k_\rho \rho_r) + \mathcal{J}_0(k_\rho \rho_r)) e^{-k_\rho(z+z')} dk_\rho \\ &= \frac{\partial}{\partial \rho_r} \int_0^\infty \mathcal{J}_1(k_\rho \rho_r) e^{-k_\rho(z+z')} dk_\rho + \frac{\partial}{\partial z} \int_0^\infty \mathcal{J}_0(k_\rho \rho_r) e^{-k_\rho(z+z')} dk_\rho \\ &= \frac{\partial}{\partial \rho_r} \frac{\tilde{R} - (z+z')}{\rho_r \tilde{R}} + \frac{\partial}{\partial z} \frac{1}{\tilde{R}} \\ &= -\frac{1}{\rho_r^2} \left(1 - \frac{z+z'}{\tilde{R}} \right) \end{aligned} \quad (2.96)$$

which, like the previously two terms, has a singularity that goes as $\frac{1}{\rho_r^2}$ for $z + z' = 0$.

As has been shown multiple singularities arise when $z + z' = 0$ for both polarisations, and in order to avoid these the scatterer has been placed slightly above the substrate such that $z + z' > 0$.

2.5 Multiple Scatterers

In Fig. 2.1 the figure of interest within this project was illustrated with two scatterers on top of a substrate, however, there is no set limit on the number of scatterers that may be considered. One example of a structure where two antennas are placed on top of a substrate is, as mentioned in Ch. 1, a PCA.

While the equations up until this point has only considered a single scatterer they can easily be extended to multiple scatterers, where the derivation of the MFIE is almost the same, where, similarly to Eq. (2.52), the LHS for a PEC may be written as the integral over multiple scatterers,

yielding

$$\begin{aligned} LHS &= - \int_{\sum_i \Omega_i} \nabla \cdot \left[\left(\{\nabla \times \mathbf{E}(\mathbf{r})\} \times \vec{\mathbf{G}}(\mathbf{r}, \mathbf{r}') \right) + \left(\mathbf{E}(\mathbf{r}) \times \{\nabla \times \vec{\mathbf{G}}(\mathbf{r}, \mathbf{r}')\} \right) \right] d^2r \\ &= - \sum_i \oint_{\partial\Omega_i} \hat{\mathbf{n}}_i \cdot \left[\{\nabla \times \mathbf{E}(\mathbf{r})\} \times \vec{\mathbf{G}}(\mathbf{r}, \mathbf{r}') + \mathbf{E}(\mathbf{r}) \times \{\nabla \times \vec{\mathbf{G}}(\mathbf{r}, \mathbf{r}')\} \right] d^2r, \end{aligned} \quad (2.97)$$

where Gauss's theorem from Eq. (A.1a) has been used. In the case of multiple scatterers in a homogeneous medium $\vec{\mathbf{G}}(\mathbf{r}, \mathbf{r}') = \vec{\mathbf{G}}^{(d)}(\mathbf{r}, \mathbf{r}')$, while in the case of a layered structure $\vec{\mathbf{G}}(\mathbf{r}, \mathbf{r}') = \vec{\mathbf{G}}^{(d)}(\mathbf{r}, \mathbf{r}') + \vec{\mathbf{G}}^{(i)}(\mathbf{r}, \mathbf{r}')$ for $z + z' \geq 0$ and $\vec{\mathbf{G}}(\mathbf{r}, \mathbf{r}') = \vec{\mathbf{G}}^{(t)}(\mathbf{r}, \mathbf{r}')$ for $z + z' < 0$. From this, the surface current can be found by a similar approach as was used in Sec. 2.3.1, yielding

$$\mathbf{J}_s(\mathbf{r}) = \mathbf{J}_0(\mathbf{r}) + \sum_i \oint_{\partial\Omega_i} \hat{\mathbf{n}} \times \nabla \times \vec{\mathbf{G}}(\mathbf{r}, \mathbf{r}') \cdot \mathbf{J}_s(\mathbf{r}') d^2r'. \quad (2.98)$$

In the case where the scatterers are evenly displaced from one another by $\Delta\mathbf{r}$, such that $k_1\Delta r \gg 1$, the current at \mathbf{r} may be assumed independent from the currents of the other scatterers, in which case they are uncoupled such that

$$\mathbf{J}_0(\mathbf{r}) = \mathbf{J}_0(\mathbf{r} + \Delta\mathbf{r}) \Rightarrow \mathbf{J}_s(\mathbf{r}) = \mathbf{J}_s(\mathbf{r} + \Delta\mathbf{r}), \quad (2.99)$$

which is the case if the incoming field is a plane wave propagating perpendicular to $\Delta\mathbf{r}$ when a scatterer is located at \mathbf{r} and $\mathbf{r} + \Delta\mathbf{r}$ with the current of each scatterer corresponding to that of just a single scatterer. In this case, the far-field may be derived from Eq. (2.60), which can be recalled for a PEC as

$$\mathbf{E}(\mathbf{r}) = \mathbf{E}_0(\mathbf{r}) + i\omega\mu_0 \oint \vec{\mathbf{G}}(\mathbf{r}, \mathbf{r}') \cdot \mathbf{J}_s(\mathbf{r}') d^2r'.$$

By only considering the scattered field and replacing the Green's tensor by the far-field Green's tensor, from Eq. (2.39) for a homogeneous medium, and from Eq. (2.81) from Eq. (2.82) for a layered structure, then the far-field for N scatterers can be written as

$$\begin{aligned} \mathbf{E}_{\text{scat}}^{(ff)}(\mathbf{r}) &= i\omega\mu_0 \oint_{\sum_{i=1}^N \partial\Omega_i} \vec{\mathbf{G}}^{(ff)}(\mathbf{r}, \mathbf{r}') \cdot \mathbf{J}_s(\mathbf{r}') d^2r' \\ &= \begin{cases} i\omega\mu_0 \oint_{\partial\Omega} \left(\vec{\mathbf{G}}^{(d,ff)}(\mathbf{r}, \mathbf{r}') \sum_{n=0}^{N-1} e^{-ink_1\Delta\mathbf{r}\cdot\hat{\mathbf{r}}} \right. \\ \quad \left. + \vec{\mathbf{G}}^{(i,ff)}(\mathbf{r}, \mathbf{r}') \sum_{n=0}^{N-1} e^{in(-k_\rho\hat{\rho}\cdot\Delta\mathbf{r} + k_{z,1}\hat{\mathbf{z}}\cdot\Delta\mathbf{r})} \right) \cdot \mathbf{J}_s(\mathbf{r}') d^2r' & \text{for } z + z' \geq 0 \\ i\omega\mu_0 \oint_{\partial\Omega} \left(\vec{\mathbf{G}}^{(t,ff)}(\mathbf{r}, \mathbf{r}') \sum_{n=0}^{N-1} e^{in(-k_\rho\hat{\rho}\cdot\Delta\mathbf{r} + k_{z,1}\hat{\mathbf{z}}\cdot\Delta\mathbf{r})} \right) \cdot \mathbf{J}_s(\mathbf{r}') d^2r' & \text{for } z + z' < 0 \end{cases} \end{aligned}$$

where the sum over the scatterers has been interchanged with a single scatterer, due to their surface current being equal to one another, however, the Green's tensor is displaced by a phase factor, and it is therefore necessary to sum over these. In the case of $\Delta\mathbf{r}$ being confined in the xy plane, the far-field simplifies to

$$\mathbf{E}_{\text{scat}}^{(ff)}(\mathbf{r}) = i\omega\mu_0 \sum_{n=0}^{N-1} e^{ink_1\hat{\mathbf{r}}\cdot\Delta\mathbf{r}} \oint_{\partial\Omega} \vec{\mathbf{G}}^{(ff)}(\mathbf{r}, \mathbf{r}') \cdot \mathbf{J}_s(\mathbf{r}') d^2r'. \quad (2.100)$$

due to the phase factor being equal for all three Green's tensors. For all purposes within this report this is the case, while it is furthermore the case for any layered structure where all scatterers are

placed on the surface of the interface between the two media. Here it is seen that when N is large, one should achieve resonance when $k_1 \hat{\mathbf{r}} \cdot \Delta \mathbf{r} = m2\pi$ with $m \in \mathbb{N}$, which is only the case for $m = 0$ if $\lambda_1 > \Delta r$, in which case $\hat{\mathbf{r}} \perp \Delta \mathbf{r}$.

Method

In Ch. 2 relevant theory regarding the evaluation of terahertz antennas using the GFIE and the GFSIE was presented, and while the actual evaluation of said antennas will be presented in Ch. 4 this chapter will present the methods used in the modelling and numerical calculations that allows for accurate models of the scatterers. Within this chapter one will therefore find a detailed description of the finite element mesh that is used, where the current is expanded in polynomials defined on each element with corresponding parametric variables and tangent vectors dependent on the geometry. Furthermore, the implementation of the MFIE with the approximation of the integrals used in order to find the surface current will be covered.

3.1 Finite Element Mesh

The content and derivations within this section are based on [6, Ch. 8] and [15, Sec. 4.2.1, Sec. 8.3 and Sec. 8.4].

When computing integrals numerically, in this case in order to determine the surface current, it is useful to approximate the solution space in which the exact solution can be reasonably approximated. This can be done by subdividing the computational domain into smaller elements and providing each element with a number of polynomials, which will be further discussed in Sec. 3.1.2. This is known as the *finite element method*, FEM. One of the advantages of using a FEM is that the distribution of elements and mesh points for the surface are entirely customisable, which allows for a good representation of the scatterer surface. This is in contrast to e.g. a finite difference method, where the mesh points are evenly distributed in a grid with each point representing a portion of space that may be shared with different media.

As an example of the use of FEM, the surface of a particle can be approximated by dividing it into triangles and using linear expansion functions, hence 1st order polynomials. Each triangle on the surface, denoted k , has three corners, denoted $\mathbf{r}_n^{(k)}$, $n = 1, 2, 3$, and the position on the triangle can then be parameterised by

$$\mathbf{r}^{(k)}(u_1, u_2) = \sum_{n=1}^3 \mathbf{r}_n^{(k)} f_n(u_1, u_2), \quad 0 \leq u_1 \leq 1, \quad 0 \leq u_2 \leq 1 - u_1, \quad (3.1)$$

where the 1st order polynomials in two dimensions are given as

$$f_1(u_1, u_2) = 1 - u_1 - u_2, \quad (3.2a)$$

$$f_2(u_1, u_2) = u_1, \quad (3.2b)$$

$$f_3(u_1, u_2) = u_2. \quad (3.2c)$$

Furthermore, a linear expansion of the surface current on the triangle can be expressed as

$$\mathbf{J}_s(\mathbf{r}^{(k)}(u_1, u_2)) = \sum_{n=1}^3 \mathbf{J}_{k,n} f_n(u_1, u_2), \quad (3.3)$$

where the coefficient $\mathbf{J}_{k,n}$ represent the value of \mathbf{J}_s at the corners of the triangle k . The functions \mathbf{J}_s on the entire particle surface can then be expressed as

$$\mathbf{J}(\mathbf{r}) = \sum_k \sum_{n=1}^3 \mathbf{J}_{k,n} f_n(\mathbf{r}), \quad (3.4)$$

where $\mathbf{r} = \mathbf{r}^{(k)}(u_1, u_2)$ is a position on the particle surface and

$$f_{k,n}(\mathbf{r}) = \begin{cases} f_n(u_1, u_2), & \mathbf{r} \in k \\ 0, & \text{otherwise} \end{cases}. \quad (3.5)$$

An approach for approximating a cylindrical surface with triangles is to generate a two-dimensional mesh and then map this onto a three-dimensional surface. Consider a rectangle in the (t_1, t_2) -plane within the region $0 \leq t_1 \leq 2\pi a$ and $0 \leq t_2 \leq H$, where a is the radius of the cylinder, while H is its height. The rectangular region can then be mapped onto a cylindrical surface using the rule

$$\mathbf{r}(t_1, t_2) = \mathbf{r}_0 + \hat{\mathbf{x}}a \cos\left(\frac{t_1}{a} + \varphi_0\right) + \hat{\mathbf{y}}a \sin\left(\frac{t_1}{a} + \varphi_0\right) + \hat{\mathbf{z}}t_2. \quad (3.6)$$

Likewise, the surface of a quarter of a half-sphere can be mapped from two dimensions to a three-dimensional surface by expressing a position on said surface as

$$\mathbf{r} = \mathbf{r}_c + \hat{\mathbf{z}}a \cos\left(\frac{t_1}{a}\right) + a \sin\left(\frac{t_1}{a}\right) \hat{\rho}(t_1, t_2), \quad (3.7)$$

where

$$\hat{\rho}(t_1, t_2) = \hat{\mathbf{x}}a \cos\left(\frac{t_2}{a \sin \frac{t_1}{a}} + \alpha_0\right) + \hat{\mathbf{y}}a \sin\left(\frac{t_2}{a \sin \frac{t_1}{a}} + \alpha_0\right). \quad (3.8)$$

It should be noted that the notation used within this introduction is the same as the notation used in Sec. 3.2, due to its simplicity compared to the notation used in the remainder of this section, however, it does not provide the same level of detail, hence why another notation has been used throughout the rest of this section.

3.1.1 Parameterisation of Triangular Elements

Every triangular element of the surface mesh can be parameterised as $\mathbf{r}(u_1, u_2)$ such that $\mathbf{r}(0, 0) = \mathbf{r}_1$, $\mathbf{r}(1, 0) = \mathbf{r}_2$ and $\mathbf{r}(0, 1) = \mathbf{r}_3$, where \mathbf{r}_1 , \mathbf{r}_2 and \mathbf{r}_3 corresponds to the corners of the triangle, and $0 \leq u_1 \leq 1$ and $0 \leq u_2 \leq 1$ with $u_1 + u_2 \leq 1$.

3.1.1.1 Parameterisation of Planar Elements

On a planar surface, the position on the element can be written as

$$\mathbf{r}(u_1, u_2) = \mathbf{r}_1 + \frac{\partial \mathbf{r}}{\partial u_1} u_1 + \frac{\partial \mathbf{r}}{\partial u_2} u_2, \quad (3.9)$$

given that the partial derivatives are constant. In this case, the derivatives may then be written with finite differences as

$$\begin{aligned} \frac{\partial \mathbf{r}}{\partial u_1} &= \frac{\mathbf{r}_2 - \mathbf{r}_1}{u_{1,2} - u_{1,1}} = \mathbf{r}_2 - \mathbf{r}_1, \\ \frac{\partial \mathbf{r}}{\partial u_2} &= \frac{\mathbf{r}_3 - \mathbf{r}_1}{u_{2,3} - u_{2,1}} = \mathbf{r}_3 - \mathbf{r}_1, \end{aligned} \quad (3.10)$$

since $u_{1,2} = 1$, $u_{1,1} = 0$, $u_{2,1} = 0$ and $u_{2,3} = 1$, as can be seen in Fig 3.1. Thus the position on the planar element can be expressed as

$$\mathbf{r}(u_1, u_2) = \mathbf{r}_1 + (\mathbf{r}_2 - \mathbf{r}_1)u_1 + (\mathbf{r}_3 - \mathbf{r}_1)u_2, \quad (3.11)$$

which can be found to be equal to Eq. (3.1) when the two-dimensional polynomials in Eq. (3.2) are inserted. Furthermore it can be seen in Fig. 3.1 that each element has two local orthonormal

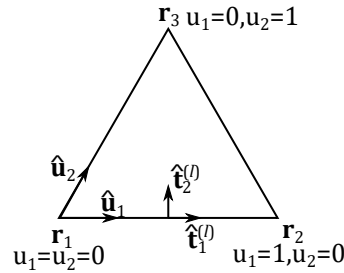


Figure 3.1: An example of a triangular mesh element. $\hat{\mathbf{t}}_1^{(l)}$ is defined along $\frac{\partial \mathbf{r}}{\partial u_1}$ and $\hat{\mathbf{t}}_2^{(l)}$ is defined perpendicular to $\hat{\mathbf{t}}_1^{(l)}$.

tangential vectors, $\hat{\mathbf{t}}_1^{(l)}$ and $\hat{\mathbf{t}}_2^{(l)}$, which may be defined as

$$\hat{\mathbf{t}}_1^{(l)} = \frac{\frac{d\mathbf{r}}{du_1}}{\left| \frac{d\mathbf{r}}{du_1} \right|} \quad (3.12a)$$

$$\hat{\mathbf{t}}_2^{(l)} = \hat{\mathbf{t}}_1^{(l)} \times \hat{\mathbf{n}}, \quad (3.12b)$$

where

$$\hat{\mathbf{n}} = \frac{\frac{d\mathbf{r}}{du_1} \times \frac{d\mathbf{r}}{du_2}}{\left| \frac{d\mathbf{r}}{du_1} \times \frac{d\mathbf{r}}{du_2} \right|}. \quad (3.13)$$

Here the superscript (l) indicates that the tangential vectors are local, hence they are defined for each element.

3.1.1.2 Parameterisation of Cylindrical Elements

An element on a cylindrical surface oriented in e.g. the z direction can be parameterised as

$$\mathbf{r}(u_1, u_2) = a \cos \varphi \hat{\mathbf{x}} + a \sin \varphi \hat{\mathbf{y}} + \mathbf{z} \hat{\mathbf{z}}, \quad (3.14)$$

where the position is dependent on both z and φ , which can be expressed in similar manner as for a planar element as

$$\begin{bmatrix} \varphi \\ z \end{bmatrix} = \begin{bmatrix} \varphi_1 \\ z_1 \end{bmatrix} + \begin{bmatrix} \frac{\partial \varphi}{\partial u_1} & \frac{\partial \varphi}{\partial u_2} \\ \frac{\partial z}{\partial u_1} & \frac{\partial z}{\partial u_2} \end{bmatrix} \begin{bmatrix} u_1 \\ u_2 \end{bmatrix}, \quad (3.15)$$

where the derivatives are set constant as the cylinder surface can be thought of as a wrapped up planar surface, with finite differences $\frac{\partial \varphi}{\partial u_1} = \frac{\varphi_2 - \varphi_1}{u_{1,2} - u_{1,1}} = \varphi_2 - \varphi_1$ and likewise for $\frac{\partial \varphi}{\partial u_2}$, $\frac{\partial z}{\partial u_1}$ and $\frac{\partial z}{\partial u_2}$.

3.1.1.3 Parameterisation of Spherical Elements

The shape of a triangular element on a sphere is defined by the geodesics which is the shortest path, between the corner points. Here the geodesics are given by great circles and the geodesic between \mathbf{r}_1 and \mathbf{r}_2 may be parameterised with uniform speed as

$$\mathbf{r}(\tau) = \mathbf{r}_1 \cos \gamma \tau + \mathbf{w} \sin \gamma \tau \quad (3.16)$$

where γ is a constant that determines the speed of the parameterisation and τ is an arbitrary parametric variable, while \mathbf{r}_1 and \mathbf{w} are orthogonal, which may be ensured by

$$\mathbf{w} = \hat{\mathbf{n}} \times \mathbf{r}_1, \quad (3.17)$$

where $\hat{\mathbf{n}} = \frac{\mathbf{r}_1 \times \mathbf{r}_2}{|\mathbf{r}_1 \times \mathbf{r}_2|}$, while γ is the angle between \mathbf{r}_1 and \mathbf{r}_2 such that $\mathbf{r}(1) = \mathbf{r}_2$, hence

$$\gamma = \sin^{-1} \left(\frac{|\mathbf{r}_1 \times \mathbf{r}_2|}{a^2} \right). \quad (3.18)$$

This can further be done for the remaining two sides of the element by a similar approach.

While this is sufficient on the boundary of the element it does not suffice within the triangle and a subtriangle can therefore be introduced, as seen in Fig. 3.2. For a subtriangle u_1 and u_2 are

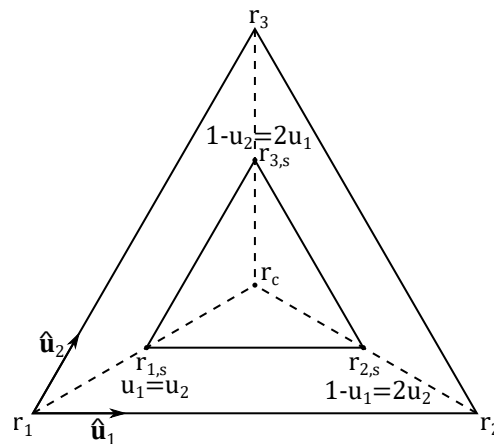


Figure 3.2: Here the subtriangle is shown with corners $\mathbf{r}_{1,s}$, $\mathbf{r}_{2,s}$ and $\mathbf{r}_{3,s}$, located along $u_1 = u_2$, $1 - u_1 = 2u_2$ and $1 - u_2 = 2u_1$ respectively with the relative arc length, s , from the center of the element, \mathbf{r}_c .

expressed as variables $s(u_1, u_2)$ and $t(u_1, u_2)$, where s determines the distance between the center

of the element, \mathbf{r}_c , that is when $u_1 = u_2 = \frac{1}{3}$, and the corners of the subtriangle, that is $s \in [0; 1]$, while t expresses where along the edge of the subtriangle a given point u_1, u_2 is located.

Like what was done for the element the geodesic for the subtriangle can be parameterised as

$$\mathbf{r}_{i,s} = \mathbf{r}_c \cos \gamma_{ci}s + \mathbf{w}_{ci} \sin \gamma_{ci}s \quad (3.19)$$

where $r_{i,s}$ corresponds to a subtriangle corner for $i \in \{1, 2, 3\}$ while

$$\mathbf{r}_c = a \frac{\mathbf{r}_1 + \mathbf{r}_2 + \mathbf{r}_3}{|\mathbf{r}_1 + \mathbf{r}_2 + \mathbf{r}_3|}. \quad (3.20)$$

Here \mathbf{w}_{ci} and γ_{ci} can be expressed similarly to \mathbf{w} and γ in Eq. (3.16).

The position on the boundary of the subtriangle may then be expressed, similarly to Eq. (3.16), with respect to s and t as

$$\mathbf{r}(s, t) = \mathbf{r}_{i,s} \cos \gamma_{ij}t + \mathbf{w}_{ij} \sin \gamma_{ij}t, \quad (3.21)$$

where

$$i = \begin{cases} 1, & \text{if } u_1 \geq u_2 \wedge 1 - u_1 > 2u_2 \\ 2, & \text{if } 1 - u_2 \geq 2u_1 \wedge 1 - u_1 < 2u_2 \\ 3, & \text{if } u_1 < u_2 \wedge 1 - u_2 \geq 2u_1 \end{cases}, \quad (3.22a)$$

$$j = \text{mod}(i, 3) + 1. \quad (3.22b)$$

Now it can be recalled that $s = 1$ at the element edge and $s = 0$ at the center, while t , like τ , can be found requiring it to be 0 or 1 at the subtriangle corners such that

$$s(u_1, u_2) = \begin{cases} 1 - 3u_2, & \text{if } i = 1 \\ 1 - 3(1 - u_1 - u_2), & \text{if } i = 2 \\ 1 - 3u_1, & \text{if } i = 3 \end{cases}, \quad (3.23a)$$

$$t(u_1, u_2) = \begin{cases} \frac{u_1 - u_2}{s}, & \text{if } i = 1 \\ \frac{2u_2 - (1 - u_1)}{s}, & \text{if } i = 2 \\ \frac{1 - u_2 - 2u_1}{s}, & \text{if } i = 3 \end{cases}. \quad (3.23b)$$

As an example, the described parameterisation is compared to the parameterisation of a planar triangle projected onto the surface of the sphere along a line connected to the center of the sphere, as can be seen in Fig. 3.3. Here the rather exaggerated element is a quarter half sphere, while the 11×11 points are evenly distributed along u_1 and u_2 . As it is evidently seen, the points are significantly more evenly distributed for the parameterisation where subtriangles has been used, as can be seen in Fig. 3.3b, compared to the projected parameterisation, seen in Fig. 3.3a.

It should be noted that in a case where both s and t are varied, the speed of the parameterisation in Eq. (3.21), that is $|\frac{\partial \mathbf{r}}{\partial u_1}|$ and $|\frac{\partial \mathbf{r}}{\partial u_2}|$, is not uniform unlike in the case of a planar or cylindrical

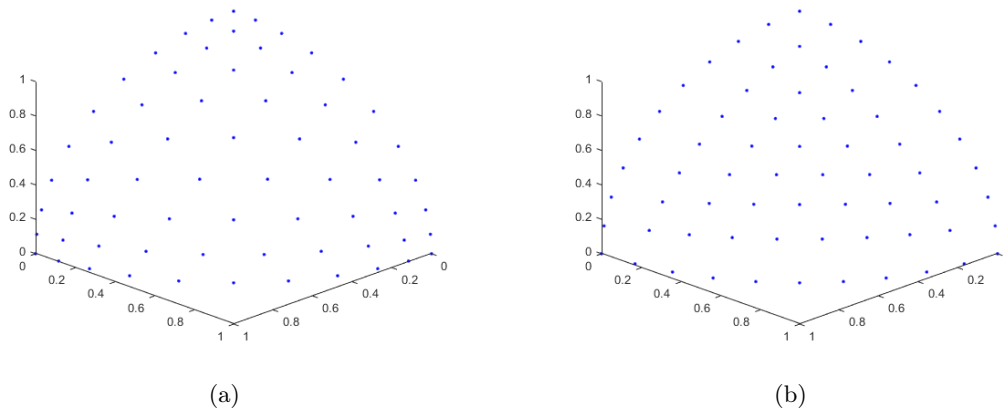


Figure 3.3: A comparison between **a**) a projected parameterisation and **b**) a parameterisation using subtriangles, both for a unit quarter hemisphere.

element, or a geodesic path on a spherical element. This is due to Gauss' Theorema Egregium[18, Ch.10], which states that the Gaussian curvature is conserved for a local isometry¹, which implies that the mapping from a sphere to a plane is not a local isometry, since the Gaussian curvature for a sphere is positive, while it is zero for a plane.

3.1.2 Polynomials

As was described in the beginning of Sec. 3.1, the surface of a particle can be divided into elements which is then provided with an m^{th} order polynomial. In the given example 1st order polynomials in two dimensions were used, where the mesh points were evenly spaced and for any $m > 0$ it was required that every corner had an associated mesh point, however, by using a higher order polynomial, the surface current could be approximated more accurately. This is due to the increase in mesh points as the order of polynomial is increased, as can be seen in Fig. 3.4. Here a two-dimensional triangular element can be seen for the first four orders of polynomials, hence from the 0th order to the 3rd order. However, this can easily be extended into the m^{th} order polynomial by adding more mesh points and while these points in this figure is evenly spaced, this is not a requirement. Besides the order of polynomial the dimension of the polynomials also affects the number of mesh points, however, this will be further discussed in Sec. 3.1.2.1, Sec. 3.1.3 and App. D.

By choosing a basis of polynomials on each element that are 1 in their corresponding mesh point and 0 in the remaining mesh points, e.g. the ones presented in Eq. (3.2), the surface current may simply be determined everywhere on the surface by summation over these polynomials, where each polynomial is weighted by the current in the associated mesh point. The polynomials along the u_1 -axis for the 1st, 2nd and 3rd order has been plotted and can be seen in Fig. 3.5, while the polynomial for the 0th order has been omitted due to it being 1 everywhere on the element. Here it can be seen that the number of polynomials increase as the order increases, however, it can further be noted

¹A local isometry is a mapping where the metric, that is the distance between any two points, is preserved.

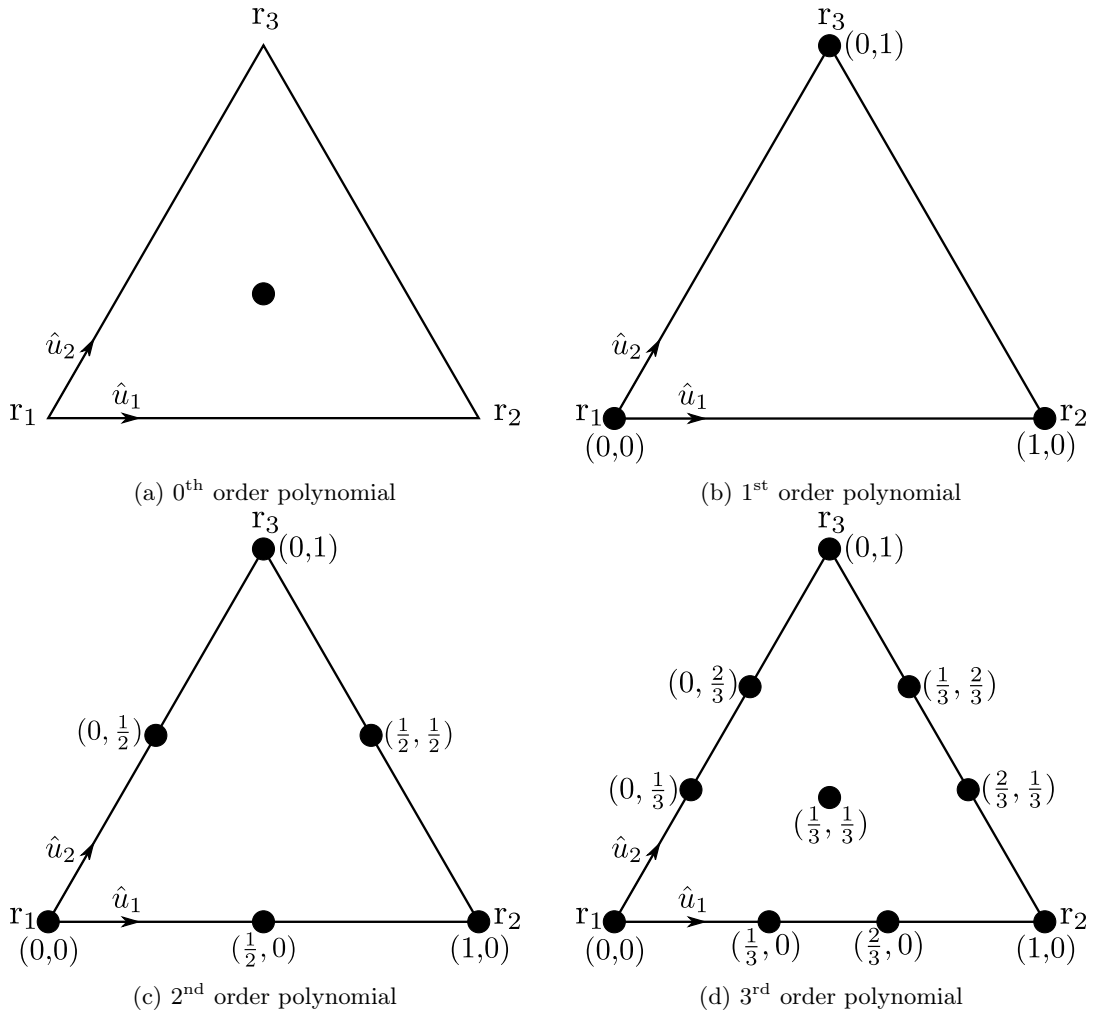


Figure 3.4: Triangular two-dimensional elements for the four first orders of polynomials, where the mesh points for each polynomial and their coordinates, (u_1, u_2) , can be seen. It should be noted that while the mesh point in Fig. 3.4a is centered within the element, this is not a requirement, as the current in this case will be constant over the entire element due to the single mesh point.

that some polynomials are mirror images of each other, e.g. the polynomial that takes on the value 1 in $(\frac{1}{3}, 0)$ and the polynomial that takes on the value 1 in $(\frac{2}{3}, 0)$ for the 3rd order. In general this may be explained by reflective- and rotational symmetry. Let $f_{(\nu_1, \nu_2)}$ denote the polynomial that is 1 in mesh point $(\frac{\nu_1}{m}, \frac{\nu_2}{m})$, where ν_i is an index that indicates the position of the mesh point in the u_i direction, then due to reflective symmetry $f_{(\nu_1, \nu_2)}(u_1, u_2) = f_{(m-\nu_1, \nu_2)}(1-u_1, u_2)$, $f_{(\nu_1, \nu_2)}(u_1, u_2) = f_{(\nu_1, m-\nu_2)}(u_1, 1-u_2)$ and $f_{(\nu_1, \nu_2)}(u_1, u_2) = f_{(\nu_2, \nu_1)}(u_2, u_1)$ must hold. Hereby rotational symmetry also follows by the use of two reflections.

Furthermore it can be seen for the 3rd order polynomials that some polynomials take on the value 1 more than once, however, since it is only 1 in a single mesh point, while it is 1 in some other point that is not a mesh point, this does not conflict with its definition.

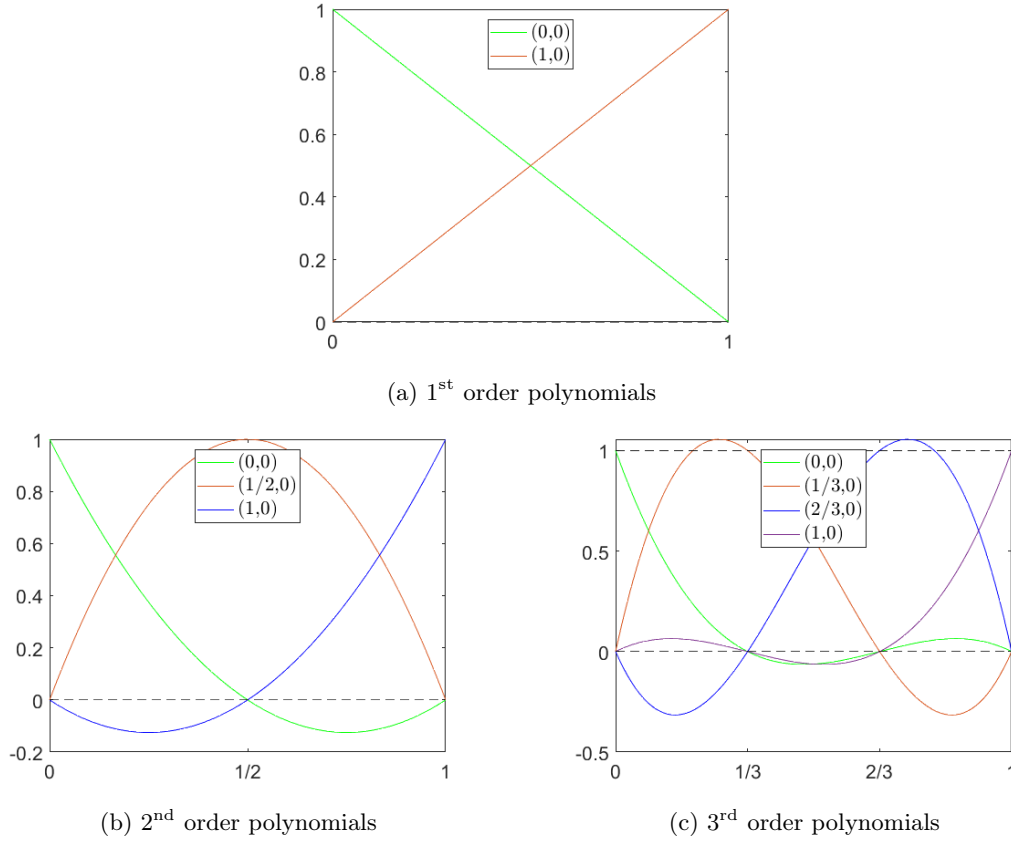


Figure 3.5: Plots of the polynomials along the u_1 -axis for the **a)** 1st, **b)** 2nd and **c)** 3rd order polynomials. The coordinate in the legend denotes the associated mesh point in which the polynomial takes on the value 1, while it can be seen that it is 0 in the remaining mesh points.

3.1.2.1 One-Dimensional Polynomials

One-dimensional polynomials only depend on a single parameter, e.g. u_1 , and will therefore present itself as a line, where the subscripts i on u and ν can be omitted, hence u_1 can be denoted simply as u . Higher-order one-dimensional polynomials of the m^{th} order, also referred to as degree m , can be obtained by defining $m + 1$ mesh points on each element, where two of the points are at the ends of the element. If the mesh points are denoted u_ν , where $\nu = 0, 1, \dots, m$ and ordered such that $u_\nu = \frac{\nu}{m}$, hence the first mesh point will be in $u_0 = 0$, while the last mesh point will be in $u_m = 1$, and it is furthermore required that the polynomial functions must equal 1 at one mesh point and zero at all other points, as has been described previously, then the polynomials can be constructed as

$$f_\nu(u) = \frac{\prod_{j=0, j \neq \nu}^m (u_j - u)}{\prod_{j=0, j \neq \nu}^m (u_j - u_\nu)}, \quad \nu = 0, 1, \dots, m, \quad x_0 \leq x \leq x_m. \quad (3.24)$$

These polynomials are said to be defined in element 1, due to the placement of the first and the last mesh point being at $u = 0$ and $u = 1$, respectively, however, they can easily be defined to any interval corresponding to element k , e.g. element 2 which will range from $u = 1$ to $u = 2$, by

scaling the input as

$$f_{k,\nu}(t) = \begin{cases} f_{\nu} \left(\frac{t-t^{(s,k)}}{t^{(e,k)}-t^{(s,k)}} \right), & t^{(s,k)} \leq t \leq t^{(e,k)} \\ 0, & \text{otherwise} \end{cases}, \quad (3.25)$$

where t is the distance from the start of element 1 and the indices s, k and e, k represent the start and end of the k^{th} element, respectively. Using these higher-order polynomials, the tangential current along a surface parameterised by \mathbf{s} can be expanded as

$$J(\mathbf{s}(t)) = \sum_k \sum_{\nu=0}^m J_{k,\nu} f_{k,\nu}(t), \quad (3.26)$$

similarly to what was done in Eq. (3.4).

3.1.3 Two-Dimensional Polynomials

In this report it is only necessary to consider the two-dimensional polynomials as the GFSIEM is used in order to calculate the current on triangular surface elements, however, if the volume was considered rather than the surface, three-dimensional polynomials would be required. A detailed general description of how the polynomials can be expressed in higher dimensions can be found in App. D, and will therefore not be covered in this section, however, while the 1st order polynomials were determined as shown in Eq. (3.2), the 2nd order polynomials can be found by using Eq. (D.10), yielding

$$f_{(0,0)}(u_1, u_2) = 2(1 - u_1 - u_2) \left(\frac{1}{2} - u_1 - u_2 \right), \quad (3.27a)$$

$$f_{(1,0)}(u_1, u_2) = 4u_1(1 - u_1 - u_2), \quad (3.27b)$$

$$f_{(2,0)}(u_1, u_2) = 2u_1 \left(u_1 - \frac{1}{2} \right), \quad (3.27c)$$

$$f_{(0,1)}(u_1, u_2) = 4u_2(1 - u_1 - u_2), \quad (3.27d)$$

$$f_{(1,1)}(u_1, u_2) = 4u_1u_2, \quad (3.27e)$$

$$f_{(0,2)}(u_1, u_2) = 2u_2 \left(u_2 - \frac{1}{2} \right). \quad (3.27f)$$

In Fig. 3.6 the polynomials in Eq. (3.27a) and Eq. (3.27b) have been plotted, where it can be seen that they only take on the value of 1 in a single mesh point, and 0 in all other mesh points, as was the case in Fig. 3.5. While this is only two of the polynomials, the remaining polynomials will be similar to these two, due to rotational symmetry, where Eq. (3.27a), Eq. (3.27c) and Eq. (3.27f) take on the value of 1 in the corners, while Eq. (3.27b), Eq. (3.27d) and Eq. (3.27e) take on the value of 1 inbetween two corners.

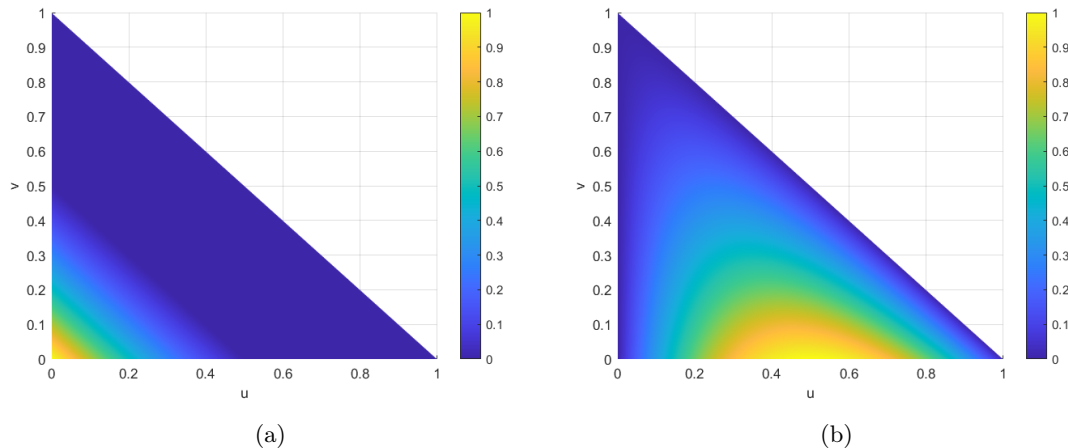


Figure 3.6: Graphic plots of the 2nd order polynomials in a) Eq. (3.27a) and b) Eq. (3.27b).

3.2 Implementation

Within this section and throughout the rest of this report a new notation will be adopted, where ν_1, \dots, ν_N will be noted as a single index, $n = 1, \dots, N_m$, in which the mesh points on an element may be enumerated, such that the polynomial coefficients for the current may be written as $J_{i,k,n}$, where i refers to one of the two components in the two-dimensional case, the tangential vectors as $\hat{\mathbf{t}}_{i,k}(\mathbf{r})$ and the polynomial as $f_{k,n}(\mathbf{r})$, where the u_1, \dots, u_N dependence is implicitly defined if \mathbf{r} is located on the element and is otherwise set to zero. Furthermore, the current may be labelled with just two indices as $J_{i,p}$, with p referring to a global reference to a mesh point by demanding that the current is continuous between elements, so the coefficients for a point must agree on surrounding elements.

In order to solve the integral equation for the surface current in Eq. (2.75), the surface of the scatterer is discretised into a number of triangular elements on which mesh points $\mathbf{r}_1, \dots, \mathbf{r}_M$ are defined, as described in Sec. 3.1, where M is the total number of mesh points. In order to store which point belongs to which element, a connectivity function $T(k, n) = q$ is defined, which maps the enumeration of the element, k , and the enumeration of the point on the element, n , to the global reference of the point q . This function is simply implemented as a two-dimensional array with entry k, n being q .

By Eq. (2.75), the integral equation for the current on the surface of a scatterer can be recalled as

$$\frac{1}{2}\mathbf{J}_s(\mathbf{r}) = \mathbf{J}_0(\mathbf{r}) + \int (\nabla g(\mathbf{r}, \mathbf{r}') [\hat{\mathbf{n}} \cdot \mathbf{J}_s(\mathbf{r}')] - \mathbf{J}_s(\mathbf{r}') [\hat{\mathbf{n}} \cdot \nabla g(\mathbf{r}, \mathbf{r}')]) d^2r',$$

where the unmarked coordinates will be referred to with the global references, while the marked coordinates will be referred to with the local references.

Due to the hairy ball theorem[19, p. 77], which states that a sphere, and thereby any shape homeomorphic to a sphere, does not have a nonvanishing continuous tangential vector field, one

may define continuous local tangential vectors $\hat{\mathbf{t}}_i^{(l)}(\mathbf{r}')$ and local currents $J_{i,k,n}^{(l)}$ on each element, instead of using their global components. The global reference to quantities may then be stored in the mesh points with the global tangent vector $\hat{\mathbf{t}}_{i,q}^{(g)}$ and current $J_{i,q}^{(g)}$, and the local surface currents may then be related to the global surface currents as

$$J_{i,k,n}^{(l)} = \hat{\mathbf{t}}_{i,k,n}^{(l)} \cdot \sum_{j=1}^2 \hat{\mathbf{t}}_{j,k,n}^{(g)} J_{j,k,n}^{(g)}, \quad (3.28)$$

where the short-hand notation $\hat{\mathbf{t}}_{i,k,n}^{(l)} = \hat{\mathbf{t}}_i^{(l)}(\mathbf{r}_{T(k,n)})$ has been utilised, hence

$$J_{1,k,n}^{(l)} = \hat{\mathbf{t}}_{1,k,n}^{(l)} \cdot (\hat{\mathbf{t}}_{1,k,n}^{(g)} J_{1,k,n}^{(g)} + \hat{\mathbf{t}}_{2,k,n}^{(g)} J_{2,k,n}^{(g)}) \quad (3.29a)$$

$$J_{2,k,n}^{(l)} = \hat{\mathbf{t}}_{2,k,n}^{(l)} \cdot (\hat{\mathbf{t}}_{1,k,n}^{(g)} J_{1,k,n}^{(g)} + \hat{\mathbf{t}}_{2,k,n}^{(g)} J_{2,k,n}^{(g)}). \quad (3.29b)$$

The surface current may then be expressed with polynomials as in Eq. (D.11), hence

$$\mathbf{J}_s(\mathbf{r}') = \sum_{k,n} f_{k,n}(\mathbf{r}') \left(\hat{\mathbf{t}}_1^{(l)}(\mathbf{r}') J_{1,k,n}^{(l)} + \hat{\mathbf{t}}_2^{(l)}(\mathbf{r}') J_{2,k,n}^{(l)} \right). \quad (3.30)$$

By inserting this expression into the integral equation for the surface current, and then replacing the expressions for $J_{i,k,n}^{(l)}$ by Eq. (3.28), before applying the scalar product with $\hat{\mathbf{t}}_{i,p}^{(g)}$, it can be found that

$$\begin{aligned} \hat{\mathbf{t}}_{i,p}^{(g)} \cdot \left(\frac{1}{2} \mathbf{J}_s(\mathbf{r}) - \mathbf{J}_0(\mathbf{r}) \right) &= \\ & \sum_{j,k,n} \int_{\Omega_k} \hat{\mathbf{n}} \cdot \left[\hat{\mathbf{t}}_1^{(l)}(\mathbf{r}') \left(\hat{\mathbf{t}}_1^{(l)}(\mathbf{r}') \cdot \hat{\mathbf{t}}_{j,k,n}^{(g)} \right) + \hat{\mathbf{t}}_2^{(l)}(\mathbf{r}') \left(\hat{\mathbf{t}}_2^{(l)}(\mathbf{r}') \cdot \hat{\mathbf{t}}_{j,k,n}^{(g)} \right) \right] \hat{\mathbf{t}}_{i,p}^{(g)} \cdot \nabla g(\mathbf{r}_p, \mathbf{r}') \\ & - \hat{\mathbf{n}} \cdot \nabla g(\mathbf{r}_p, \mathbf{r}') \left[\left(\hat{\mathbf{t}}_{i,p}^{(g)}(\mathbf{r}) \cdot \hat{\mathbf{t}}_1^{(l)}(\mathbf{r}') \right) \left(\hat{\mathbf{t}}_1^{(l)}(\mathbf{r}') \cdot \hat{\mathbf{t}}_{j,k,n}^{(g)} \right) \right. \\ & \quad \left. + \left(\hat{\mathbf{t}}_{i,p}^{(g)} \cdot \hat{\mathbf{t}}_2^{(l)}(\mathbf{r}') \right) \left(\hat{\mathbf{t}}_2^{(l)}(\mathbf{r}') \cdot \hat{\mathbf{t}}_{j,k,n}^{(g)} \right) \right] f_{k,n}(\mathbf{r}') J_{j,k,n}^{(g)} d^2 r' \\ & = \sum_{j,k,n} J_{j,k,n}^{(g)} \int_{\Omega_k} \kappa_{i,j,n}(\mathbf{r}_p, \mathbf{r}') d^2 r'. \end{aligned} \quad (3.31)$$

In order to obtain a matrix equation, \mathbf{J}_s is related to \mathbf{J}_0 by a matrix consisting of the integrals in Eq. (3.31). Here, the i^{th} component of the integral equation may be related to the contribution from the j^{th} component of \mathbf{J}_s from the integral through the block matrix $K^{(i,j)}$, where the total matrix is accordingly stated as

$$\bar{\bar{K}} = \begin{bmatrix} \bar{\bar{K}}^{(1,1)} & \bar{\bar{K}}^{(1,2)} \\ \bar{\bar{K}}^{(2,1)} & \bar{\bar{K}}^{(2,2)} \end{bmatrix}, \quad (3.32)$$

where for one of the block matrices, entry p, q is given by

$$\bar{\bar{K}}_{p,q}^{(i,j)} = \sum_{\substack{k,n \\ T(k,n)=q}} \int_{\Omega_k} \kappa_{i,j,n}(\mathbf{r}_p, \mathbf{r}') d^2 r', \quad (3.33)$$

where the sum is over every element that is constituted by point q for which $J_{i,q}^{(g)}$ has a contribution.

A matrix equation for the integral equation can then be obtained using that $\bar{\bar{A}}\mathbf{J} = \mathbf{J}_0$, where

$\bar{\bar{A}} = \frac{1}{2}\bar{\bar{I}} - \bar{\bar{K}}$, hence

$$\begin{bmatrix} \frac{1}{2}\bar{\bar{I}} - \bar{\bar{K}}^{(1,1)} & -\bar{\bar{K}}^{(1,2)} \\ -\bar{\bar{K}}^{(2,1)} & \frac{1}{2}\bar{\bar{I}} - \bar{\bar{K}}^{(2,2)} \end{bmatrix} \begin{bmatrix} \mathbf{J}^{(1)} \\ \mathbf{J}^{(2)} \end{bmatrix} = \begin{bmatrix} \mathbf{J}_0^{(1)} \\ \mathbf{J}_0^{(2)} \end{bmatrix}, \quad (3.34)$$

where $\mathbf{J}_q^{(j)} = J_{j,q}^{(g)}$ and $\mathbf{J}_{0,p}^{(i)} = J_{0,i,p}^{(g)}$.

While this matrix equation can straight forwardly be used in order to find \mathbf{J}_0 it is still, as indicated by the integral equation, the current \mathbf{J}_s that is unknown. In order to find the current from this matrix equation one can use Eq. (2.62a) in order to analytically find an expression for J_0 , which for a plane wave is given as

$$\mathbf{J}_0 = \hat{\mathbf{n}} \times \mathbf{H}_0 e^{i\mathbf{k}\cdot\mathbf{r}}, \quad (3.35)$$

while $\bar{\bar{A}}$ can be found numerically, as will be described in Sec. 3.2.1, and \mathbf{J}_s can then be found by inversion.

3.2.1 Numerical Integration

As briefly mentioned in Sec. 3.2 the matrix $\bar{\bar{A}}$ in Eq. (3.34) can be found numerically, which will be the aim of this section.

The integrals in Eq. (3.33) can be solved numerically by submeshing each element into even smaller elements, due to the use of the FEM, where the local tangential vectors are calculated in the center of each subelement. An example of such submeshing can be seen in Fig 3.7.

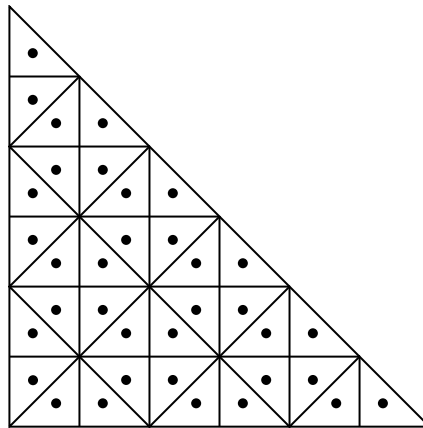


Figure 3.7: An element of the scatterer surface submeshed into smaller triangular elements with their respective centers in the shown dots.

This allows for efficient numerical integration thus the integral in Eq. (3.33) can be replaced by

the following sum,

$$\begin{aligned} & \sum_{s,k} \hat{\mathbf{n}}(\mathbf{r}_p) \cdot \left(\hat{\mathbf{t}}_1^{(l)}(\mathbf{r}'_{s,k}) (\hat{\mathbf{t}}_1^{(l)}(\mathbf{r}'_{s,k}) \cdot \hat{\mathbf{t}}_{j,k,n}^{(g)}) + \hat{\mathbf{t}}_2^{(l)}(\mathbf{r}'_{s,k}) (\hat{\mathbf{t}}_2^{(l)}(\mathbf{r}'_{s,k}) \cdot \hat{\mathbf{t}}_{j,k,n}^{(g)}) \right) \hat{\mathbf{t}}_{i,p} \cdot \nabla g(\mathbf{r}_p, \mathbf{r}'_{s,k}) \\ & - \hat{\mathbf{n}}(\mathbf{r}_p) \cdot \nabla g(\mathbf{r}_p, \mathbf{r}'_{s,k}) \left(\hat{\mathbf{t}}_{i,p}^{(g)} \cdot \hat{\mathbf{t}}_1^{(l)}(\mathbf{r}') (\hat{\mathbf{t}}_1^{(l)}(\mathbf{r}'_{s,k}) \cdot \hat{\mathbf{t}}_{j,k,n}^{(g)}) + (\hat{\mathbf{t}}_{i,p}^{(g)} \cdot \hat{\mathbf{t}}_2^{(l)}(\mathbf{r}'_{s,k})) (\hat{\mathbf{t}}_2^{(l)}(\mathbf{r}'_{s,k}) \cdot \hat{\mathbf{t}}_{j,k,n}^{(g)}) \right) \mathcal{A}_{s,k}, \end{aligned} \quad (3.36)$$

where $\mathbf{r}'_{s,k}$ represents the point in the middle of subelement s on element k , and $\mathcal{A}_{s,k}$ is the area of the subelement as will be described in Sec. 3.2.1.1. As discussed in Sec. 2.3.1.2, the singularity of the integral can be neglected and is thus ignored in this numerical calculation.

3.2.1.1 Area of Triangular Subelements

The area of subelement s of element k , used in Eq. (3.36), can be expressed as

$$\mathcal{A}_{s,k} = \begin{cases} \frac{1}{2} \left| \frac{d\mathbf{r}}{du} \times \frac{d\mathbf{r}}{dv} \right|, & \text{for a triangle on a plane or a cylinder,} \\ (A + B + C - \pi)R^2, & \text{for a triangle on a sphere,} \end{cases} \quad (3.37)$$

where A , B and C are the angles at the corners of the triangle, found by the spherical law of cosines, $\cos A = \frac{\cos \alpha - \cos \beta \cos \gamma}{\sin \beta \sin \gamma}$, and likewise for B and C , through cyclical permutations, while R is the radius of the sphere the mesh is defined upon.

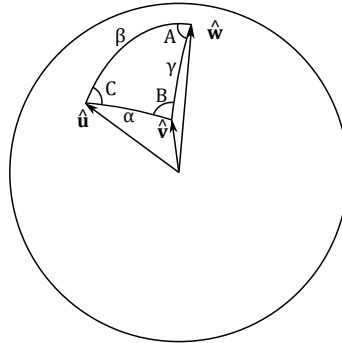


Figure 3.8: Illustration of triangle on a spherical surface.

The spherical law of cosines can be shown by letting $\hat{\mathbf{u}}$, $\hat{\mathbf{v}}$ and $\hat{\mathbf{w}}$ denote unit vectors from the center of a unit sphere to the corners of a triangle on the surface of the sphere. Then $\hat{\mathbf{u}} \cdot \hat{\mathbf{u}} = 1$, $\hat{\mathbf{u}} \cdot \hat{\mathbf{v}} = \cos \alpha$, $\hat{\mathbf{u}} \cdot \hat{\mathbf{w}} = \cos \beta$ and $\hat{\mathbf{v}} \cdot \hat{\mathbf{w}} = \cos \gamma$. The vectors resulting from the cross products $\hat{\mathbf{u}} \times \hat{\mathbf{v}}$ and $\hat{\mathbf{u}} \times \hat{\mathbf{w}}$ have the lengths $\sin \alpha$ and $\sin \beta$, respectively, and the angle between them is C , thus

$$\sin \alpha \sin \beta \cos C = (\hat{\mathbf{u}} \times \hat{\mathbf{v}}) \cdot (\hat{\mathbf{u}} \times \hat{\mathbf{w}}) = (\hat{\mathbf{u}} \cdot \hat{\mathbf{u}})(\hat{\mathbf{v}} \cdot \hat{\mathbf{w}}) - (\hat{\mathbf{u}} \cdot \hat{\mathbf{v}})(\hat{\mathbf{u}} \cdot \hat{\mathbf{w}}) = \cos \gamma - \cos \alpha \cos \beta. \quad (3.38)$$

The distance between two points on a spherical surface corresponds $a \cos \theta$ where a is the radius and θ is the angle between two points \mathbf{r}_1 and \mathbf{r}_2 , while the center of the j th subelement on element k may be found by

$$\mathbf{r}_c = \frac{\mathbf{r}_{1,j,k} + \mathbf{r}_{2,j,k} + \mathbf{r}_{3,j,k}}{|\mathbf{r}_{1,j,k} + \mathbf{r}_{2,j,k} + \mathbf{r}_{3,j,k}|} a, \quad (3.39)$$

where $\mathbf{r}_{i,j,k}$ is the i^{th} corner point in the j^{th} subelement on the k^{th} element. Here the corner points

themselves are contained in a list, where another connectivity function T_{sub} is used to relate the local subelements and subpoints to the global subpoints.

3.2.2 Implementation of the Indirect Green's Tensor

As described in Sec. 2.4.3.1 singularities occur for both s- and p-polarisation when $\tilde{R} \rightarrow 0$, however, in order to avoid them they can be subtracted from the original expression for the indirect Green's tensor in Eq. (2.79a).

By combining the terms derived in Eq. (2.92) and Eq. (2.93) the s-polarised indirect Green's tensor can be found, while the p-polarised indirect Green's tensor can be found by combining Eq. (2.94), Eq. (2.95) and Eq. (2.96), which yields

$$\nabla \times \mathbf{G}^{(i,s)} \approx \frac{\varepsilon_3 - \varepsilon_1}{32\pi} k_0^2 \ln(\tilde{R} + z + z') (\hat{\rho}_r \hat{\varphi}_r - \hat{\varphi}_r \hat{\rho}_r) \quad (3.40a)$$

$$\nabla \times \mathbf{G}^{(i,p)} \approx \frac{1}{4\pi} \frac{\varepsilon_3 - \varepsilon_1}{\varepsilon_3 + \varepsilon_1} \left(\frac{\rho_r}{\tilde{R}^3} \hat{\varphi}_r \hat{\mathbf{z}} - \frac{1}{\rho_r^2} \left(1 - \frac{z + z'}{\tilde{R}} \right) (\hat{\varphi}_r \hat{\rho}_r + \hat{\rho}_r \hat{\varphi}_r) + \frac{z + z'}{\tilde{R}^3} \hat{\varphi}_r \hat{\rho}_r \right), \quad (3.40b)$$

near the singularity. These expressions for the singularities, may be separated from the remaining indirect Green's tensor which should then be well behaved. Then the Green's tensor may be determined by tabulating and interpolating the well behaved part and then adding the singular terms separately. Here it should be noted that the discontinuity found for the $z\varphi$ -component for s-polarisation in Eq. (2.91) has not been subtracted as this does not prevent discontinuities in the tabulation.

For the tabulation, values are determined in a triangular lattice with

$$\begin{bmatrix} \rho_r \\ z + z' \end{bmatrix} = \begin{bmatrix} \Delta\rho_r & 0 \\ \Delta z/2 & \Delta z \end{bmatrix} \begin{bmatrix} t_1 \\ t_2 \end{bmatrix} \quad (3.41)$$

for $t_1 \in \mathbb{N}$ and $t_2 \in \mathbb{Z}$, where $\Delta\rho_r$ is the discretisation relative to ρ_r , while Δz is the discretisation relative to $z + z'$. Here the first and second column in the 2×2 matrix corresponds to the first and second lattice vector, respectively.

For the interpolation, one may define cells with lattice points corresponding to points at mt_1 and mt_2 , where m can be recalled to be the order of the polynomial, however, the value of m chosen for the interpolation does not have to be the same m used in order to find the current. Given a position, $(\rho_r, z + z')$, one may find the coefficients for the corresponding lattice vectors as

$$\begin{bmatrix} a_1 \\ a_2 \end{bmatrix} = \frac{1}{m} \begin{bmatrix} \Delta\rho_r & 0 \\ \Delta z/2 & \Delta z \end{bmatrix}^{-1} \begin{bmatrix} \rho_r \\ z + z' \end{bmatrix}, \quad (3.42)$$

where in the case ρ_r and $z + z'$ are zero, a small value is added to ρ_r in order to avoid tabulating at the singularity. The limit with $z + z' = 0$ and $\rho_r \rightarrow 0$ is specifically chosen as this case is prevalent, which is relevant as the integrals may be discontinuous around the origin.

Now a cell may be subdivided into two triangles, for which the value on the triangle may be determined by the polynomials, in the same manner as the current has been interpolated with the tabulated values corresponding to mesh points on an element as seen in App. D. In order to find these polynomials u_1 and u_2 have to be found and may be determined as

$$\begin{cases} u_1 = \text{mod}(a_1, 1), u_2 = \text{mod}(a_2, 1), & \text{if } \text{mod}(a_1, 1) + \text{mod}(a_2, 1) \leq 1 \\ u_1 = 1 - \text{mod}(a_1, 1), u_2 = 1 - \text{mod}(a_2, 1), & \text{if } \text{mod}(a_1, 1) + \text{mod}(a_2, 1) > 1 \end{cases}, \quad (3.43)$$

depending on which triangle is in question.

In Fig. 3.9 and Fig. 3.11 the s- and p-polarised components of the indirect Green's tensor are shown respectively, where in both figures the first row is the terms where the singularities have been included, where an upper limit has been set for the colorbar to 1, while they in the last row have been subtracted. For both polarisations it can be seen that the expressions without

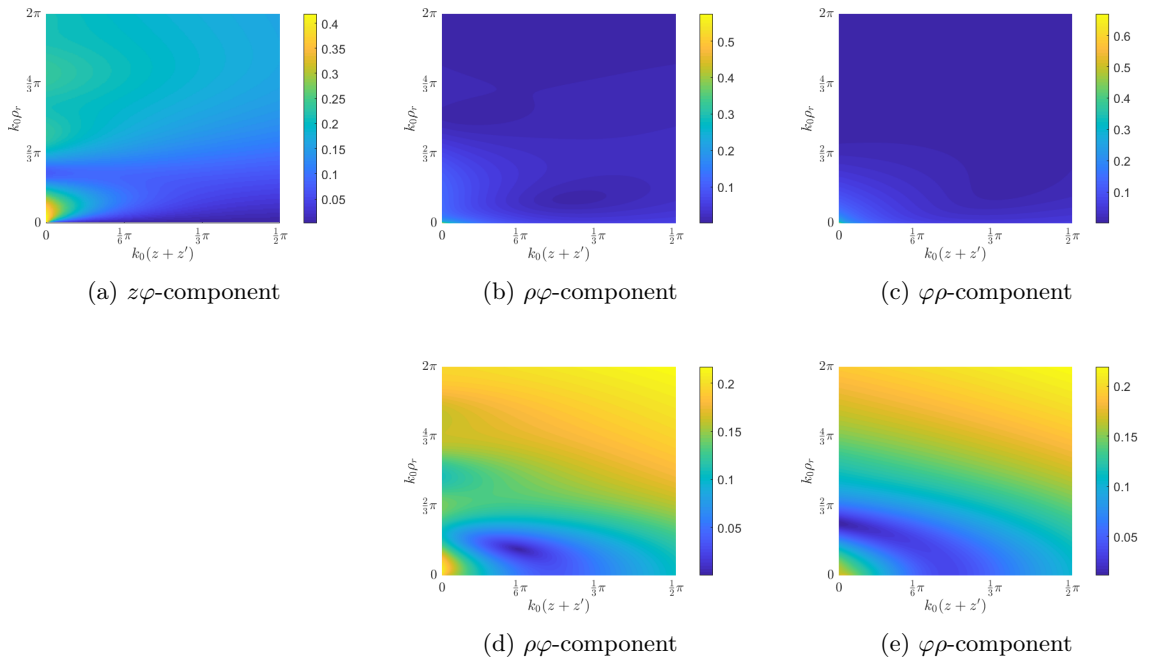


Figure 3.9: Plots of the different terms of the indirect Green's tensor for s-polarisation before (a - c) and after (d - e) the singularities have been subtracted. It should be noted that the discontinuity found in the $z\varphi$ -component has not been subtracted.

singularities are well behaved compared to the expressions where the singularities are included, due to the more even distribution, however, in order to see this for s-polarisation Fig. 3.10 has to be consulted, in order to see the singularity in the lower left corner from the plots in Fig. 3.9b and Fig. 3.9c. This is furthermore a confirmation that the derived analytic expressions for the singularities are correct.

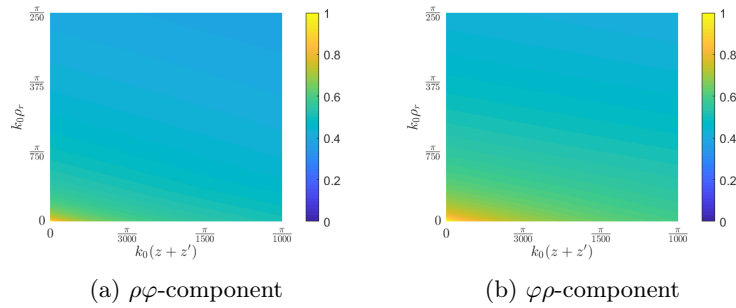


Figure 3.10: Zoom in on the singularities in the lower left corner for s-polarisation.

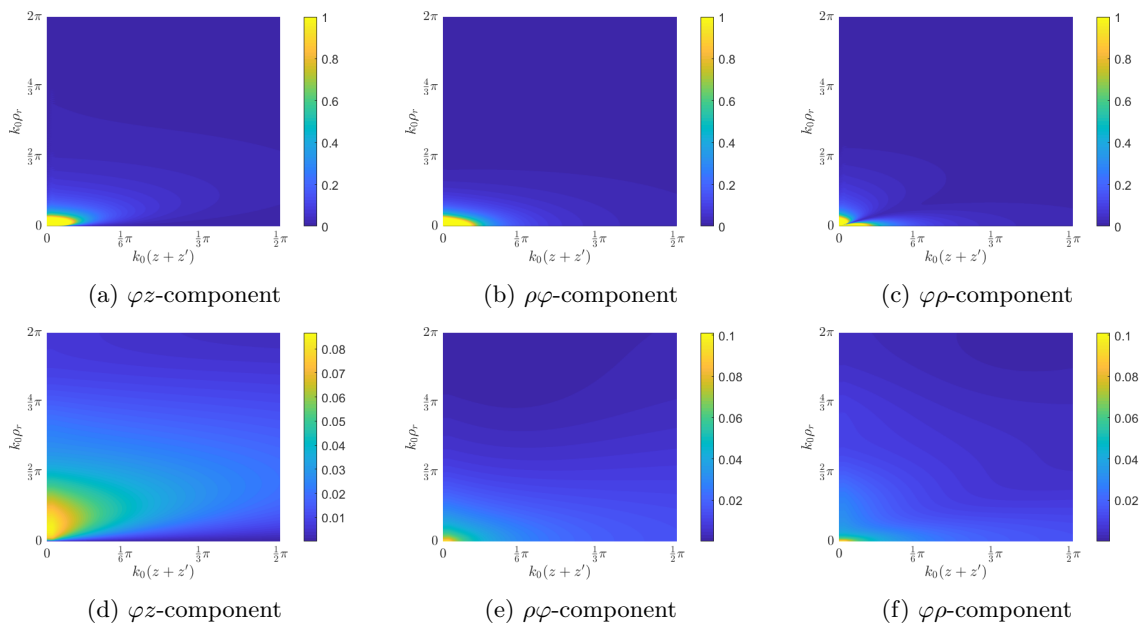


Figure 3.11: Plots of the different terms of the indirect Green's tensor for p-polarisation before (a - c) and after (d - f) the singularities have been subtracted.

Results and Analysis

Within this chapter the results from the different simulations obtained for different PEC antennas in different structures, using the theory from Ch. 2 along with the implementation described in Ch. 3, will be presented and analysed. This chapter will be split into sections based on the shape of the scatterer and the environment surrounding it. It should be noted that the incident field has been normalised to $1 \frac{\text{V}}{\text{m}}$ and is propagating in the z -direction and polarised along the x -direction for the calculations for the current on a spherical scatterer, and in the $-z$ -direction, with polarisation along the $-x$ -direction for all other calculations. All far-field plots presented in this chapter show differential scattering cross sections, normalised by dividing with $(4a)^2$ for the spherical antennas, where a is the radius of the sphere, and $(2l)^2$ for the box-antenna, where l is the length of the box.

4.1 Differential Scattering Cross Section of a Dipole

The most common type of antenna is the dipole antenna [20, pp.21], and it is therefore interesting to compare the far-field radiation patterns of the antennas produced within this report to that of a dipole antenna.

The far-field can be expressed by Eq. (2.21a) as

$$\mathbf{E}^{(d,ff)}(\mathbf{r}) = i\omega\mu_0 \oint \overleftrightarrow{\mathbf{G}}^{(d,ff)}(\mathbf{r}, \mathbf{r}') \cdot \mathbf{J}(\mathbf{r}') d^3r', \quad (4.1)$$

where for a dipole at the origin $\mathbf{J}(\mathbf{r}') = \delta(\mathbf{r}') \frac{d}{dt} \mathbf{p}$, with $\mathbf{p} = p\hat{\mathbf{p}}$ being the dipole moment. Thus

$$\begin{aligned} \mathbf{E}^{(d,ff)}(\mathbf{r}) &= \omega^2 \mu_0 p \overleftrightarrow{\mathbf{G}}^{(d,ff)}(\mathbf{r}, \mathbf{0}) \cdot \hat{\mathbf{p}} \\ &= \omega^2 \mu_0 p (\hat{\boldsymbol{\theta}}\hat{\boldsymbol{\theta}} \cdot \hat{\mathbf{p}} + \hat{\boldsymbol{\varphi}}\hat{\boldsymbol{\varphi}} \cdot \hat{\mathbf{p}}) \frac{e^{ik_0\sqrt{\epsilon}r}}{4\pi r}. \end{aligned} \quad (4.2)$$

Fig. 4.1 shows the far-field radiation pattern from a dipole, calculated by taking the absolute value of $\mathbf{E}^{(d,ff)}$, yielding

$$\left| \mathbf{E}^{(d,ff)}(\mathbf{r}) \right| = \frac{\omega^2 \mu_0 p}{4\pi r} \sqrt{(\hat{\boldsymbol{\theta}} \cdot \hat{\mathbf{p}})^2 + (\hat{\boldsymbol{\varphi}} \cdot \hat{\mathbf{p}})^2}. \quad (4.3)$$

Here $\hat{\boldsymbol{\varphi}} = \hat{\mathbf{y}} \cos \varphi \sin \theta - \hat{\mathbf{x}} \sin \varphi \sin \theta$ and $\hat{\boldsymbol{\theta}} = \hat{\mathbf{z}} \sin \theta + \hat{\mathbf{y}} \sin \varphi \cos \theta + \hat{\mathbf{x}} \cos \varphi \cos \theta$, hence

$$\left| \mathbf{E}^{(d,ff)}(\mathbf{r}) \right| = \frac{\omega^2 \mu_0 p}{4\pi r} |\sin \alpha|, \quad (4.4)$$

where α is the angle between $\hat{\mathbf{p}}$ and $\hat{\mathbf{r}}$.

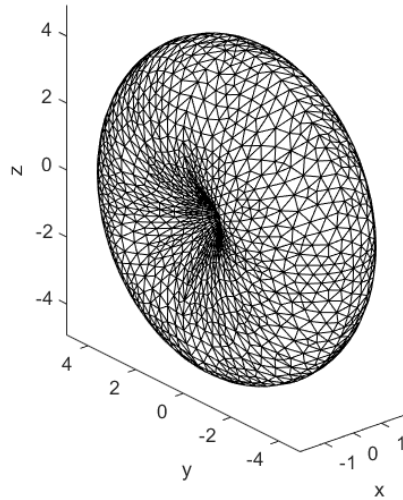


Figure 4.1: The far-field radiation pattern of a dipole which is placed in the x -direction, which can be seen to take on the form of a torus. Here the units are arbitrary.

4.2 Evaluation of the Spherical Scatterer in Free Space

In all the results involving the analytical solution of the surface current for a spherical scatterer in free space, the summations in Eq. (E.15) are approximated by 30 summations as discussed in App. E, while all numerical results for the surface current has been obtained using Eq. (2.75).

4.2.1 Comparison of Parameters

In this section, different parameters used when calculating the numerical surface current are examined. In order to do this, the numerically obtained results should be compared to an analytical solution in order to evaluate the accuracy of the numerical results, which is possible for a sphere. Furthermore, plots of the θ - and φ -components will be presented for different combinations of parameters, where in all plots with fixed wavelength it has been used that $\frac{\lambda}{a} = 4$, while $\varphi = 0$ for the θ - component, and $\varphi = \frac{\pi}{2}$ for the φ -component.

m	# Elements	# Subelements	Faceted	Normalised Error	Normalised Time
Reference Combination					
2	480	121	No	1	1

Table 4.1 – continued on next page

Table 4.1 – continued from previous page					
m	# Elements	# Subelements	Faceted	Normalised Error	Normalised Time
Varying the Order of the Polynomial, m					
0	480	121	No	14.70	0.09
1	480	121	No	3.57	0.13
3	480	121	No	0.98	3.76
Varying the Number of Elements					
2	48	121	No	8.56	0.01
2	208	121	No	2.06	0.18
2	800	121	No	0.55	2.72
Varying the Number of Subelements					
2	480	25	No	1.89	0.23
2	480	441	No	0.90	3.56
2	480	961	No	0.83	7.29
Faceted Elements					
2	480	121	Yes	1121	0.99

Table 4.1: The results from numerical simulations made in order to test which combination of parameters results in the best result for the least amount of computation time.

In Tab. 4.1 different parameter combinations, their errors, calculated as the RMSE deviation from the analytical result, and their associated computation time are shown. Here the compared points correspond to the ones at the element vertices, edge midpoints and face midpoints in the case of 480 elements. The error and computation time are both normalised by dividing with the values of the chosen reference configuration. To give an idea of the actual computation time to find the current, the reference configuration for a sphere took 1.7 hours to complete on one of the applied personal computers, while it took 8.5 hours to complete the current for a box-shaped scatterer in a homogeneous media for the same combination. If the reference combination is compared to the analytical results, as can be seen in Fig. 4.2, it is clear that the numerical result for this combination does correspond to the analytically obtained results, thus the results obtained using this combination are assumed to be accurate. Here the numerical result is achieved by finding the

element and its corresponding parametric variables, given a position on the sphere, from which the current may be found.

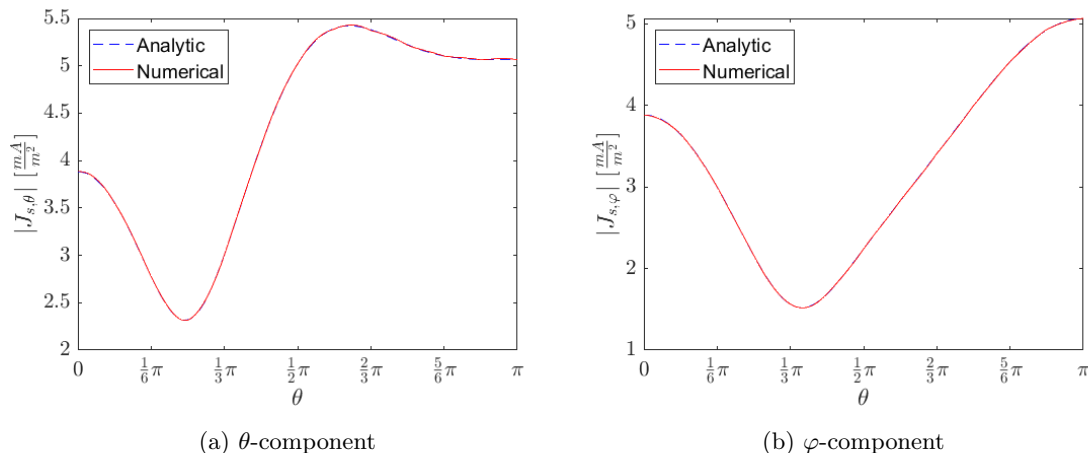


Figure 4.2: The numerically obtained surface current of a spherical scatterer using the reference combination, compared to the analytical results for said scatterer.

Before looking further into the relevance of the different parameters, and how they affect the normalised error and computation time, the computation time should be evaluated further.

The time needed for calculating the surface current, is dependent on the number of integrals over elements in Eq. (3.33) that must be solved, which is in turn dependent on the number of elements, N_k , the total number of mesh points N_p , and the amount of points on each element, N_m , hence

$$\#integrals = 4N_p N_m N_k, \quad (4.5)$$

where the factor 4 arrives due to the four combinations of the contribution from the two components of \mathbf{J}_s to the two components of the integral. The time needed to compute each integral is proportional to the amount of subelements, N_{sub} . Thus the time, t , needed to complete the calculations is

$$t \propto 4N_p N_m N_k N_{\text{sub}}. \quad (4.6)$$

The number of points on each element can be determined by considering the Euler characteristic, $\chi = V + F - E$, where V is the number of vertexes, F is the number of faces and E is the number of edges of the triangulation of a surface. For a sphere or a box it holds that $\chi = 2$, and in this case $F = N_k$. Each edge is shared by two elements and each element has three edges, which leads to the relation $\frac{1}{3}E = \frac{1}{2}N_k \Rightarrow E = \frac{3}{2}N_k$, thus $V = 2 + \frac{1}{2}N_k$. For $m \neq 0$, the total amount of mesh points N_p can be expressed as

$$N_p = V + E(m-1) + \left(\binom{m+2}{2} - 3m \right) N_k, \quad (4.7)$$

where the second term represent the points along the edges of the elements and the third term represent the interior points on the elements. Substituting the expressions for E and V into Eq.

(4.7) yields

$$N_p = 2 + \frac{1}{2}N_k + \frac{3}{2}N_k(m-1) + \left(\binom{m+2}{2} - 3m \right) N_k. \quad (4.8)$$

Thus $N_p = \mathcal{O}(N_k m^2)$, as $\binom{m+2}{2} = \frac{1}{2}m^2 + \frac{3}{2}m + 1$.

In the case where $m = 0$, then $N_p = N_k$ as each element will only have a single unshared point, as seen in Fig. 3.4a.

From this it can be seen that the worst case computation time can be found to be

$$t = \mathcal{O}(N_k^2 m^2 N_m N_{\text{sub}}), \quad \text{for } m \neq 0, \quad (4.9a)$$

$$t \propto N_k^2 N_m N_{\text{sub}}, \quad \text{for } m = 0. \quad (4.9b)$$

Now, the results presented in Tab. 4.1 can be discussed. First off, it is noticeable that the faceted model has a normalised error that is more than a 1000 times worse than the reference combination, and almost 80 times worse than the otherwise poorest combination, where 0th order polynomials are used. When Fig. 4.3 is considered it becomes even clearer how poorly the model using faceted

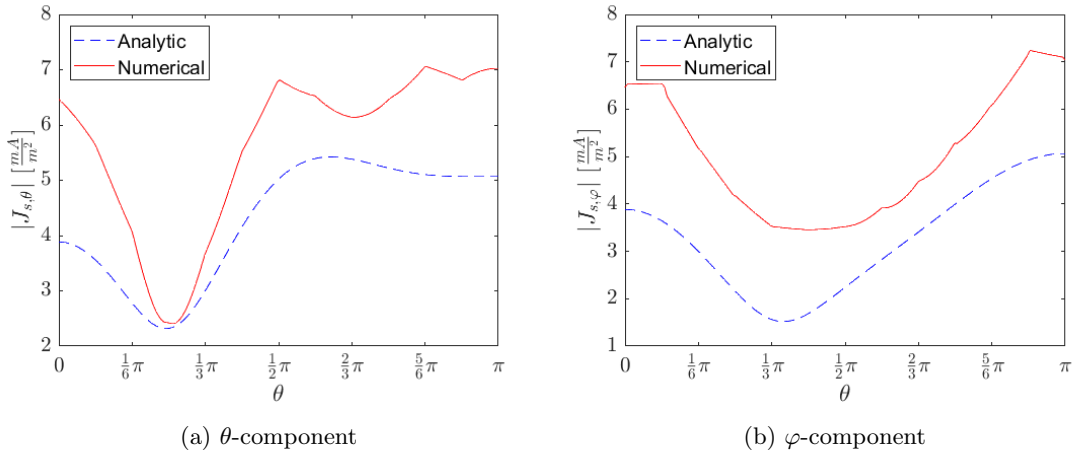


Figure 4.3: The numerically obtained surface current as calculated by a model with faceted elements compared to the analytical result.

elements relate to the analytical results, and it must therefore be concluded that this model is inferior to the models using curved elements.

Secondly, it can be seen that the polynomial degree does affect the normalised error quite significantly. From Fig. 4.4 it is easily observed that both a model using 2nd order and 3rd polynomials fit the analytical result considerably in comparison to the models using 0th and 1st order polynomials. A part of the reason for the poor performance of the first order polynomials for the complex valued currents is, that unlike in the case of real numbers, the magnitude of a sum of complex numbers is equal to or less than the sum of the magnitudes. As a result, the magnitude of the current dips between each mesh point, as shown in Fig. 4.4b. This could potentially be accounted

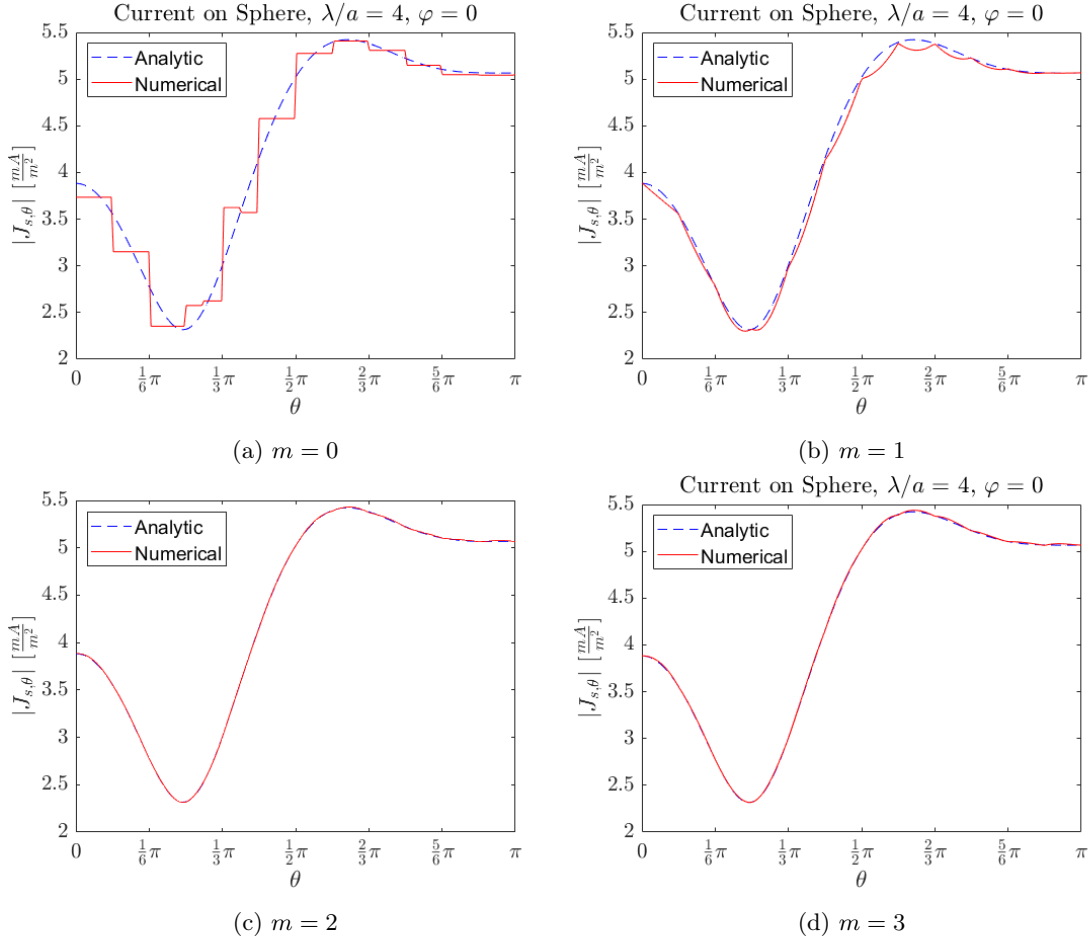


Figure 4.4: A comparison of the θ -component of the surface current, where the numerical results are calculated using different degrees of polynomials.

for by linearly varying the phase and the amplitude of the current separately, however, this has not been prioritised, since a higher order polynomial has been used.

This is also what can be deduced from the normalised error in the table, however, it is furthermore relevant to discuss the computation time. In order to predict the normalised computation time from the equations presented previously, Eq. (4.6) can be used, hence

$$\text{normalised time} = \frac{t}{t_0} = \frac{N_p N_m N_k N_{\text{sub}}}{N_{p,0} N_{m,0} N_{k,0} N_{\text{sub},0}}, \quad (4.10)$$

where t_0 is the computation time for the reference combination, and N_p can be found using Eq. (4.8), or by $N_p = N_k$ if $m = 0$. This yields the normalised computation times

$$\begin{aligned} m = 0 & : 0.08, \\ m = 1 & : 0.13, \\ m = 3 & : 3.75, \end{aligned}$$

which is relatively close to the normalised computation times presented in the table. To summarise, one should use polynomials of at least 2nd order to obtain the most accurate results, however, while

a further increase in the degree of the polynomial does not significantly decrease the normalised error it does increase the normalised computation time considerably, thus polynomials of the 2nd order is the most cost effective.

Next, the numerical results using different numbers of elements can be evaluated. From Fig. 4.5

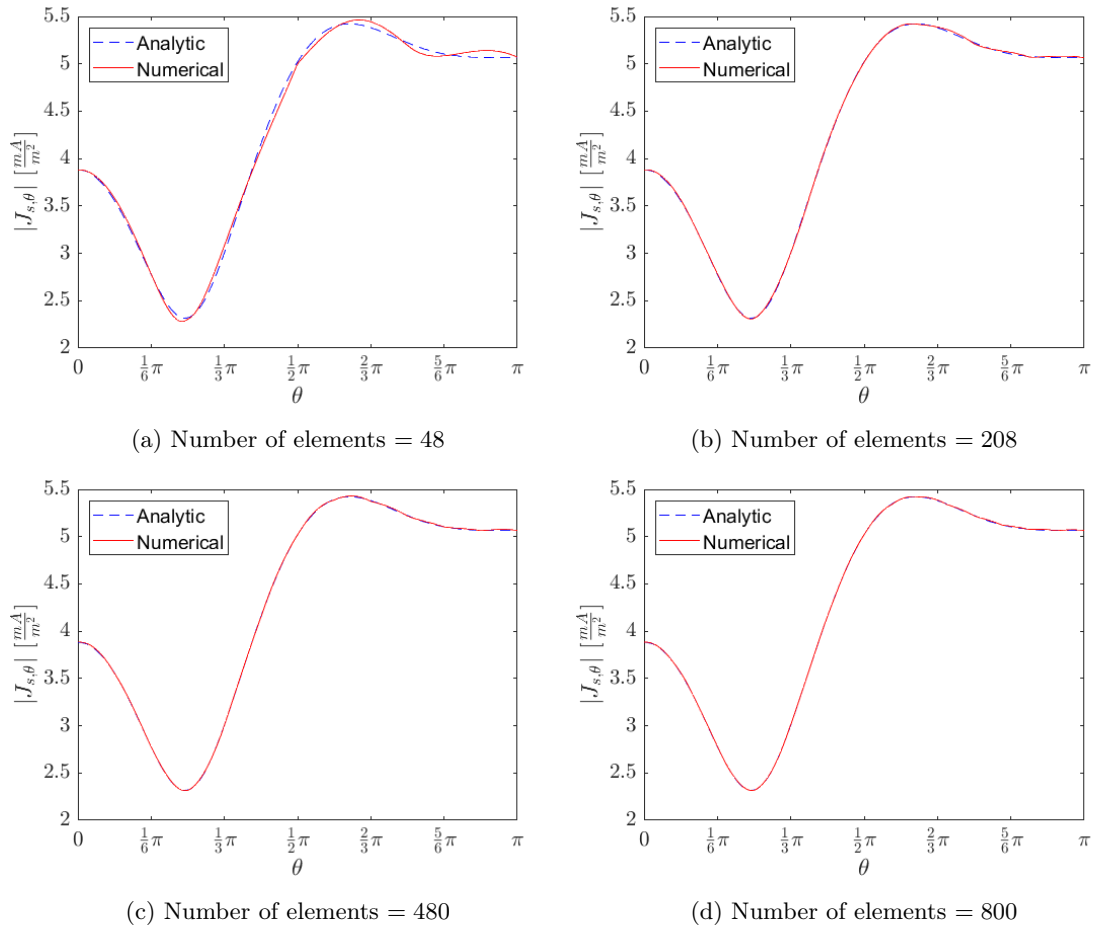


Figure 4.5: A comparison of the θ component of the surface current calculated using different numbers of elements.

it can be seen that even the model using only 48 elements can be used to produce decent results, while a model using 208 elements, or more, will produce results that seemingly correspond to the analytical results. However, by consulting the table it can be seen that the normalised error does get approximately twice as good every time the number of elements is increased by approximately two. The reason why the plots and the table do not seem to correspond is likely due to the normalised error being calculated for multiple values of φ , while the plots only uses $\varphi = \frac{\pi}{2}$, thus, a small error in one direction that can barely be seen in the plots may result in a noticeable error when summed up over all directions.

When the normalised computation time is considered, it could be predicted by Eq. (4.9a) that the computation time would depend on the number of elements squared, hence the normalised

computation times could be predicted to be

$$\begin{aligned} N_k = 48 & : 0.01, \\ N_k = 208 & : 0.19, \\ N_k = 800 & : 2.78, \end{aligned}$$

which is slightly larger than the values in the table, however, these predicted values are the worst case normalised computation times, thus it would be expected that the values from the table would be less than the predicted values. In summary, while the reference combination uses 480 elements it might be sufficient to use 208, as the difference between the normalised error for these two is a factor of two, while the difference in normalised computation time is a factor of five. However, in this project the additional accuracy has been valued higher than the longer computation time, hence why the number of elements in the reference combination has been chosen to be 480.

Lastly, the number of subelements on each element is considered. In Fig. 4.6 it can be seen that

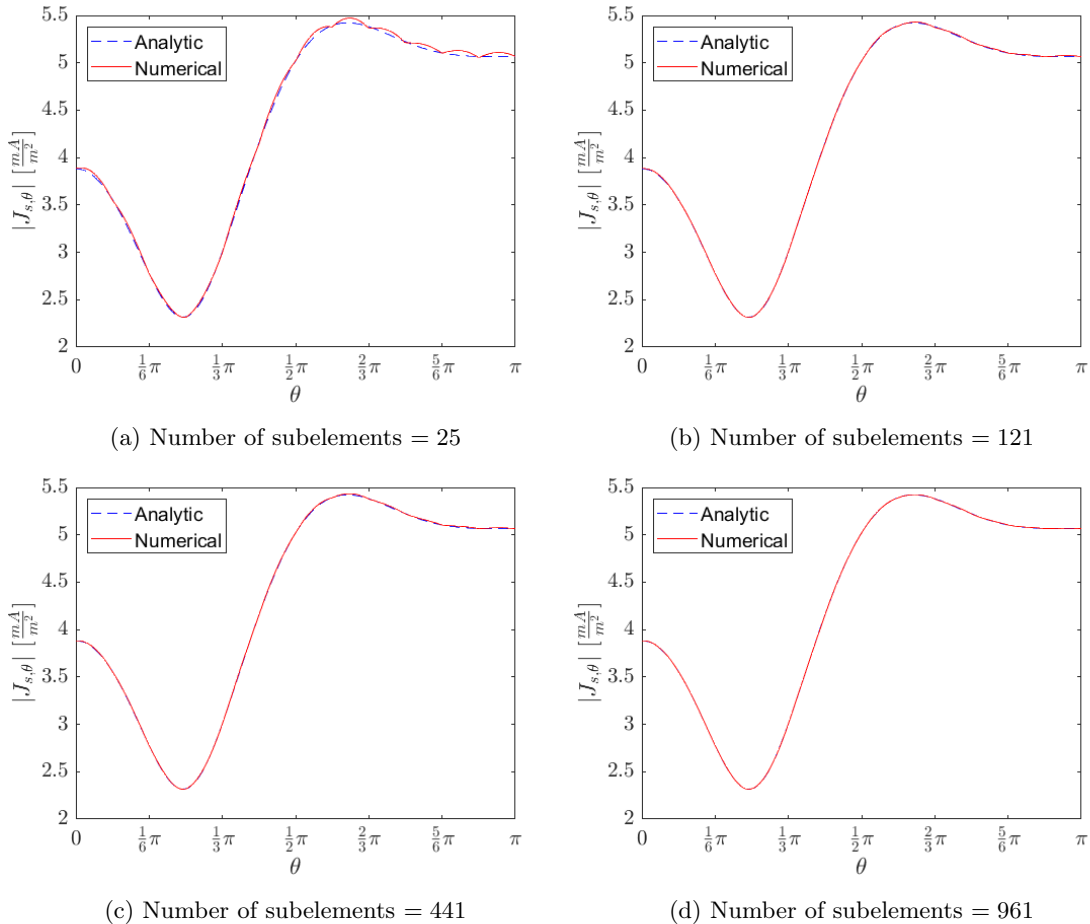


Figure 4.6: A comparison of the θ component of the surface current calculated using different numbers of subelements.

already at a small number of subelements the numerical model seems to match with the analytical result. However, as was discussed when the number of elements was varied the values for the

normalised error from the table does not entirely correspond to what is seen in the plots when few subelements are used, likely due to similar reasoning. Though, from both the plots and the table an increase in the number of subelements beyond 121 does not suggest that the normalised error should improve significantly.

From Eq. (4.9a) it was predicted that the normalised computation time would depend linearly on the number of subelements, hence the normalised computation time could be predicted to be

$$\begin{aligned} N_{\text{sub}} = 25 & : 0.21, \\ N_{\text{sub}} = 441 & : 3.64, \\ N_{\text{sub}} = 961 & : 7.94, \end{aligned}$$

which, like what was the case when the number of elements was varied, is larger than the values from the table, however, once again these predicted normalised computation times are the worst case computation times, thus this is expected. To summarise, at least 121 subelements, as in the reference configuration, should be used, however, due to the significant increase in computation time it has, for the purpose of this report, been deemed sufficient to use 121 subelements.

In conclusion, the values of the parameters used in the reference combination have been appropriately chosen for this project in order to obtain the most accurate results that are still cost effective with regards to the computation time.

4.2.2 Evaluation of the Surface Current

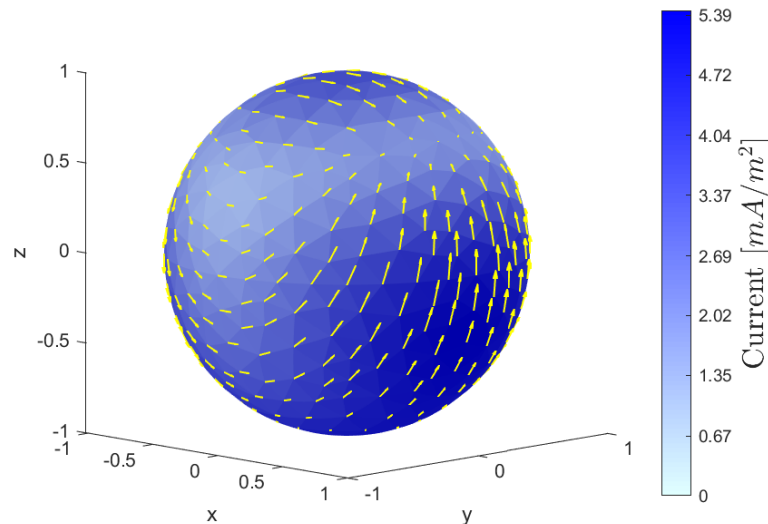


Figure 4.7: The surface current on a spherical scatterer where the arrows indicate the direction of the current.

The calculated surface current for a spherical scatterer is shown in Fig. 4.7, where the arrows indicate the direction of the current at an arbitrary phase and the color indicates the magnitude.

The distribution of the current is symmetrical, and there are two 'node points', where the current runs to and from.

In Fig. 4.7 and in all subsequent surface current plots, the absolute value of the current is shown as constant within each element, which is not the case, as a weighted average is used from the current defined at the mesh points on the element. Here mesh points placed on the edges of the element are weighted 8/3 times as heavily since this corresponds to how much greater the average value of the corresponding polynomial is on the element.

4.2.3 Evaluating the Stability as a Function of the Wavelength

In Sec. 4.2.1 the ratio between the wavelength of the incoming light and the radius of the sphere was chosen such that $\frac{\lambda}{a} = 4$, however, it should be noted that it can be difficult to calculate the surface current accurately if this ratio becomes small. This is due to an increase in the frequency, thus the numerical calculations become more "rough" as it struggles to process the rapid oscillations, as can be seen from Eq. (2.19), where it can be recalled that the exponential term goes as

$$g(\mathbf{r}, \mathbf{r}') \propto e^{ik_0\sqrt{\epsilon}|\mathbf{r}-\mathbf{r}'|},$$

hence the phase is proportional to k_0 . Though, this instability can be reduced by increasing the number of elements and/or the number of subelements.

In order to test this, results from simulations of varying wavelengths will be conducted with different numbers of elements and subelements. In this case, the error is measured only in points corresponding to the element vertices for 480 elements as opposed to what was done in Sec. 4.2.1 in order to limit computation time.

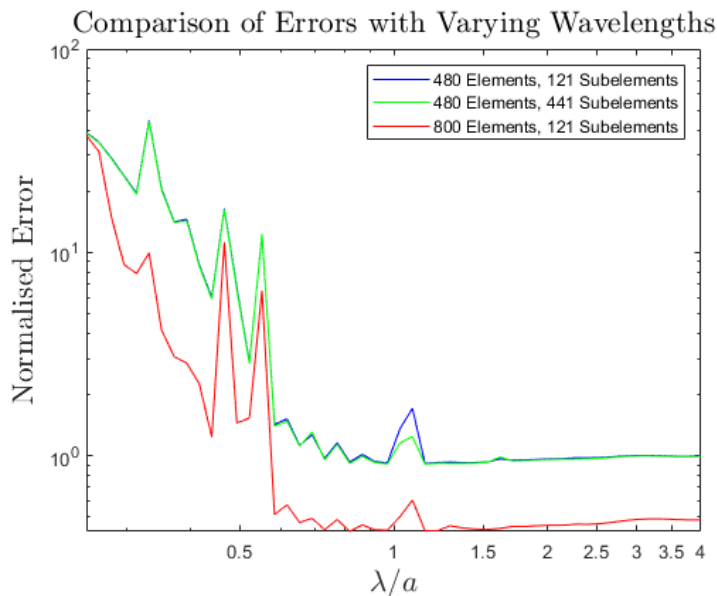


Figure 4.8: The error of a spherical scatterer compared to the analytical results for differing wavelengths.

From Fig. 4.8 it can be seen that the model for all three combinations of the number of elements and subelements used is relatively stable down to a ratio of around 0.6, after which the error spikes greatly. Furthermore, it is seen that increasing the amount of subelements offers little to no change in stability, while the number of elements, seem to have some positive effect on the stability of the method at low wavelengths, however the instability is still large.

4.2.4 Evaluation of the Differential Scattering Cross Section

The results from the simulations of the far-field for a spherical scatterer are shown in Fig. 4.9, for the ratios 4, 8 and 64 between the wavelength of the incident field and the radius of the scatterer, where it can be seen that the far-field radiation patterns do depend on this ratio. This result is somewhat consistent with those found in e.g. [21], though in the article the far-field is found to resemble a dipole, i.e. a torus, for small spheres, as discussed in Sec. 4.1, however, the results from our model seem to converge to a contorted torus, which is likely due to the simulation in this report being made for a perfectly conducting sphere, unlike the scatterer in the article.

From these far-field radiation patterns it can be seen that a small scatterer relative to the wavelength seem to scatter more of the incident field back relative to any other direction, while for a relatively large scatterer, the scattered field seems to propagate forward.

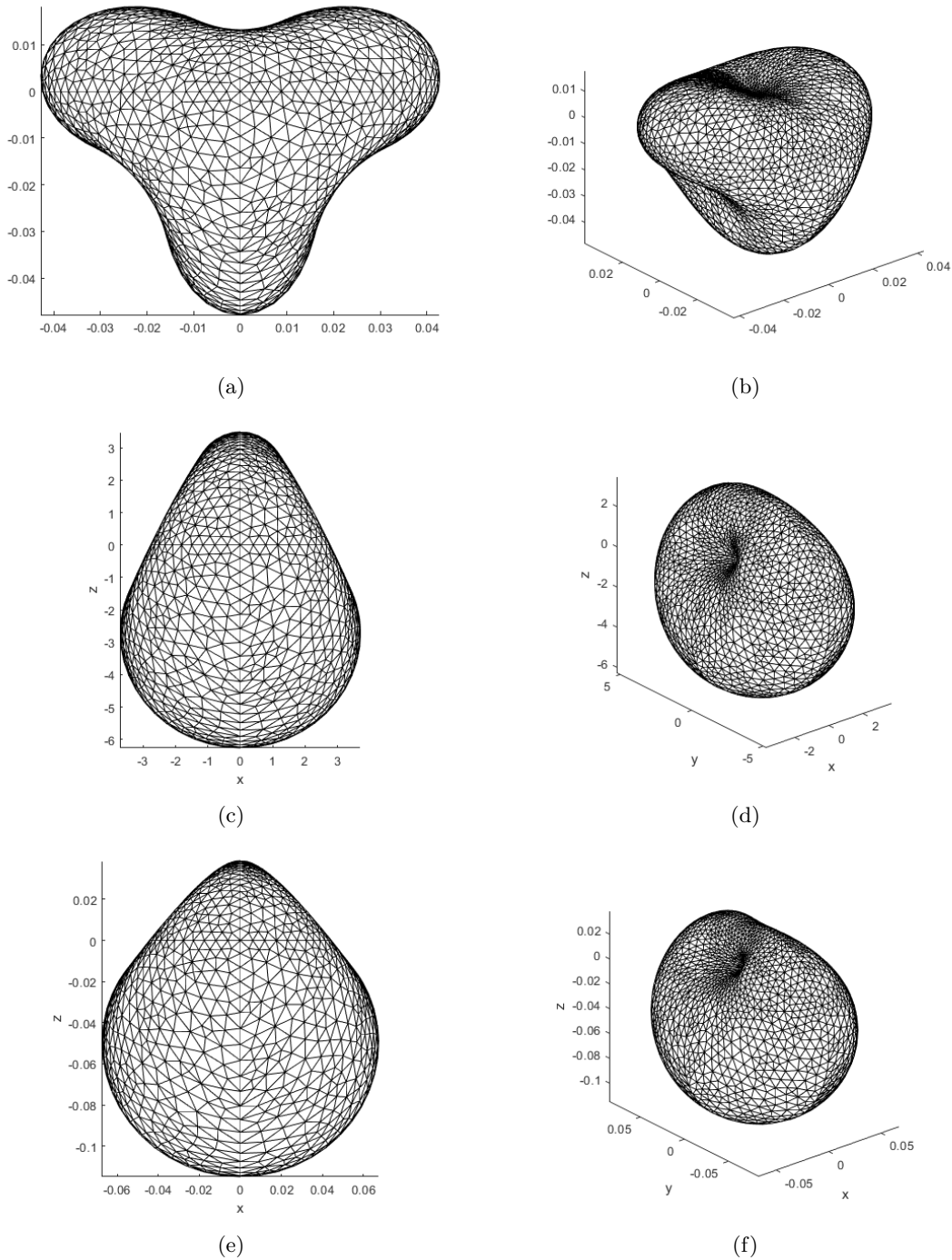


Figure 4.9: The far-field of a spherical scatterer with wavelength to radius ratio of 4, 8 and 64, and scattering cross sections 0.0073 , 0.0691 and $1.1666 \cdot 10^{-5}$ for **a)** and **b)**, **c)** and **d)**, and **e)** and **f)**, respectively.

4.3 Evaluation of a Single Box-shaped Scatterer in Free Space

A more realistic terahertz antenna is a box antenna, which in this case is approximated to assume the shape of a rounded box. The box is constructed by replacing the edges with cylinders and the corners with quarter spheres, thus the height of the box is dictated by the radius of the sphere used when constructing the box. This section explores the results from the simulations of such a

box both in a homogeneous medium. For all simulations made in this section, where the relative wavelength has been held constant, the box has dimensions $l = 20a$, $w = 5a$ and $h = 2a$, where a is the rounding radius.

4.3.1 Evaluation of Resonance

In order to find the optimal wavelength, i.e. when the scattered field is maximised, for a give antenna, it is worth looking at which relative wavelength resonances occur given a normal incident field. Naturally, for a thin wire one would expect resonances for ratios $l = n\frac{\lambda}{2}$ for odd integers n as the opposing currents will largely cancel the fields for the even cases, hence the resonances are expected to be strongest for small n .

In Fig 4.10 the scattering cross section of antennas with varying ratios is plotted. It is seen that the scattering cross section seems to peak at a ratio of around 2.4, indicating a resonance. If interpreted as the $n = 1$ peak, this would correspond to an effective length of $l^* = \frac{2.4}{2}l = 1.2l$. The second resonance appears to peak about a ratio of 0.7, which may be interpreted as the $n = 3$ peak with an effective length $l^* = \frac{3 \cdot 0.7}{2} = 1.05l$, which is closer to the expected length. This is likely due to the antenna not being a thin wire but a rounded box, hence an effective length may be defined, as will be further discussed in Sec. 4.3.2.

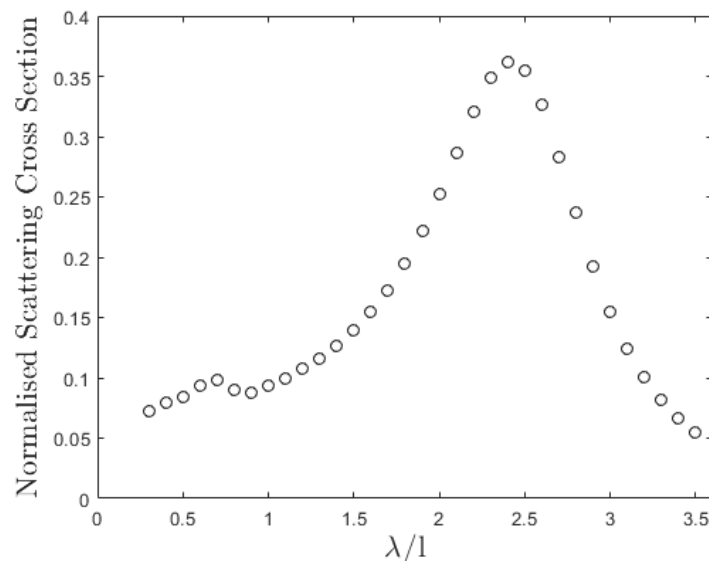


Figure 4.10: The normalised scattering cross section as a function of the ratio between the wavelength of the incoming light and the length of the antenna. Here, the length of the antenna has been held constant and the wavelength has varied.

4.3.2 Evaluation of the Surface Current

In Fig. 4.11a, the calculated surface current on a box in resonance is shown. The direction of the current changes as the phase varies. The current along the path represented by the black line, which wraps all the way around the antenna, is illustrated in Fig. 4.11b. Here it can be seen that

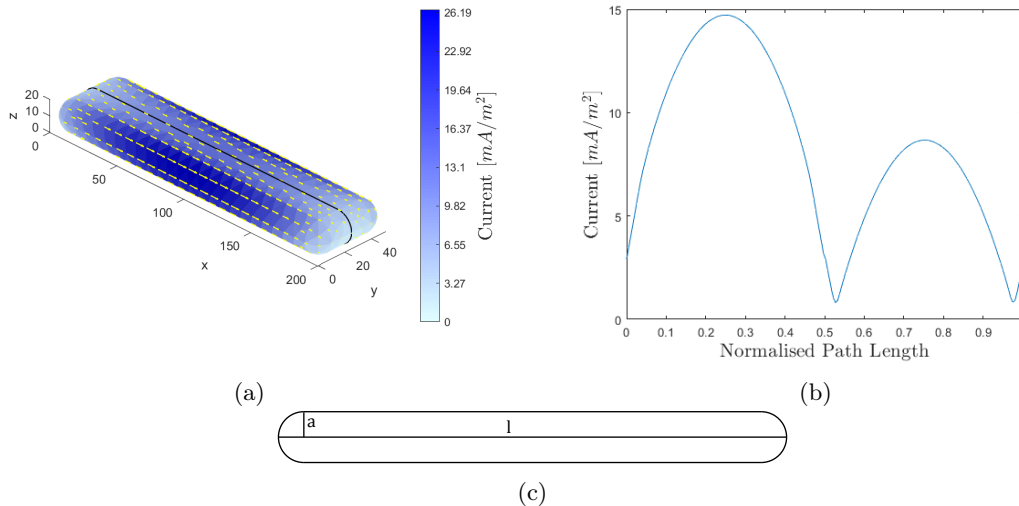


Figure 4.11: **a)** The surface current of a box antenna at wavelength to length ratio 2.4, **b)** the current density along the path shown in Fig. 4.11a, where the large resonance corresponds to the top of the box and the smaller one to the bottom, and **c)** cross section of the antenna at the path shown in Fig. 4.11a.

the current takes the form of half a sinusoidal wave on each side of the antenna. The effective length of the antenna can be calculated by multiplying the normalised distance between the node points, i.e. where the current changes direction, in this case 0.553 for the large resonance, with the path length of the entire revolution, given by $L = 2(l - 2a) + 2\pi a = 0.9l + \frac{\pi l}{10}$. In Fig. 4.11c the geometry of the path is illustrated. This results in an effective length given by

$$l^* = 0.553 \cdot L = 1.168l,$$

corresponding nicely to around half of the resonance wavelength at $\lambda = 2.4l$, which fits nicely, although a more accurate location of the peak could be obtained with more data points for the scattering cross section.

4.3.3 Evaluation of the Differential Scattering Cross Section

In Fig. 4.12 the far-field for two antennas of different length has been modelled. It is seen that the far-field is dependent on length of the antenna and for short antennas the radiation pattern resembles that of a spherical scatterer. Furthermore it can be seen that the pattern tends fairly quickly towards a torus shape, which is somewhat to be expected as a longer antenna can be approximated as a thin wire antenna, which acts as a dipole since for a thin wire the induced current can only run along a single direction.

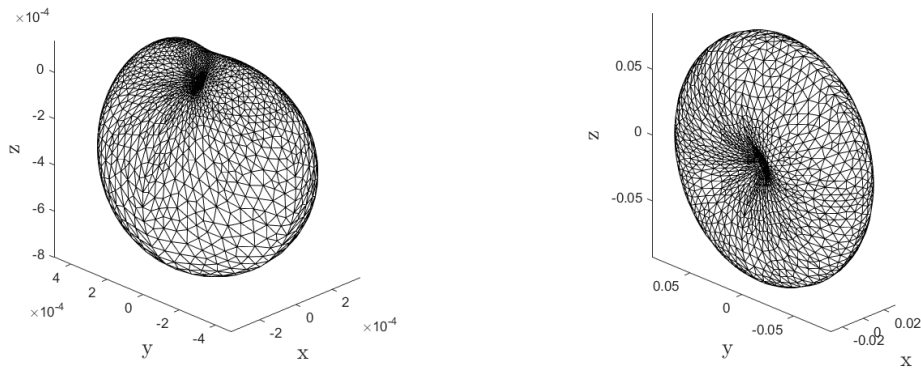


Figure 4.12: The far-field of box antennas with length to wavelength ratio 1/16 and 7/16, and scattering cross sections $8.90 \cdot 10^{-4}$ and 0.349, respectively.

4.4 Evaluation of a Single Box-shaped Scatterer on a Layered Structure

In this section, the box antenna is examined when placed on a substrate with a refractive index $n = 3.4$ corresponding to that of silicon[22] in the case of terahertz radiation. Due to numerical instability of the indirect Green’s tensor, the scatter is placed $\frac{a}{100}$ above the substrate. The ratio chosen for examination is $\frac{\lambda}{l} = 2.4$ in order to be able to compare this surface current with the corresponding result without a substrate shown in Fig. 4.11b.

4.4.1 Evaluation of the Surface Current

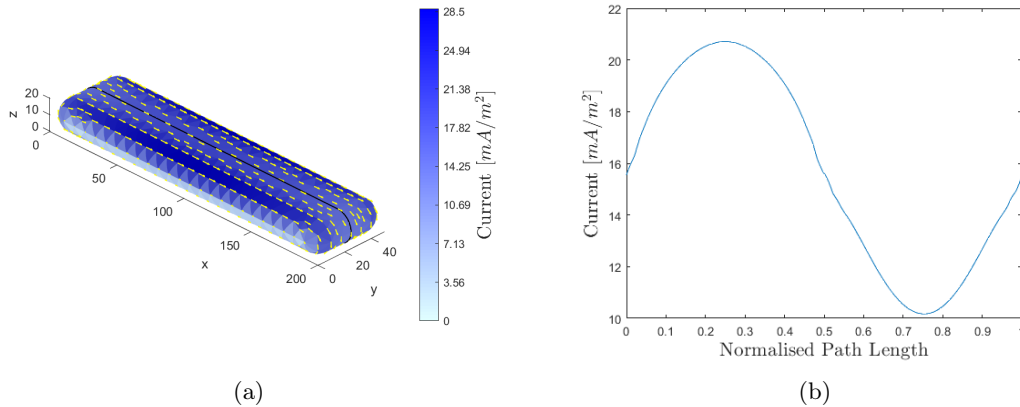


Figure 4.13: **a)** The surface current of a box antenna placed on a dielectric substrate, at wavelength to length ratio 2.4 and **b)** the current along the path shown in Fig. 4.13a.

In Fig. 4.13 the current for a substrate is shown to have a rather different behaviour than without the silicon substrate. Rather than having nodes at the endpoints, the current seems to make a full oscillation around the box with a minimum on the midpoint of the face in contact with the substrate, where the current instead goes to zero on the side of the box. Despite these differences, the maximum current density between the two cases are relatively close.

4.4.2 Evaluation of the Differential Scattering Cross Section

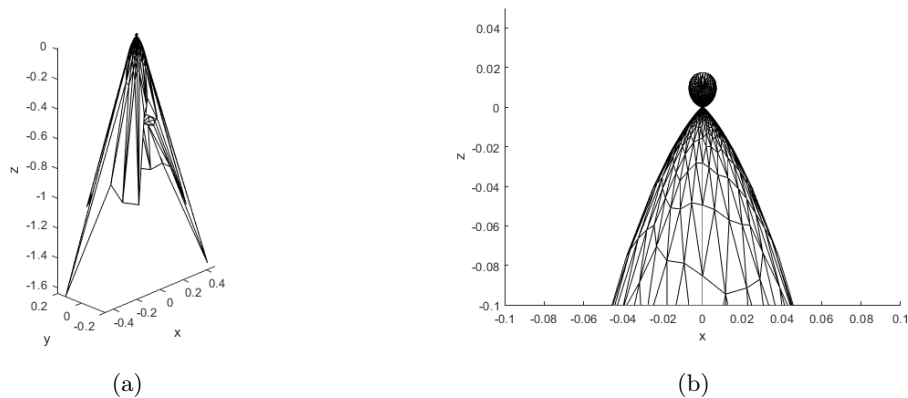


Figure 4.14: The differential scattering cross section of a box antenna placed on a dielectric substrate is seen **a** from the side and **b** zoomed in around the top where the backscattered part is shown.

In Fig. 4.14 it can be seen that most of the scattered field is coupled into the substrate with just 9.95% of the energy scattered backwards. Most of the transmitted power is at an angle of 16.85° from the substrate normal. The meshing of the DSCS is quite rough for the transmitted part and could have been calculated more accurately, however, due to time constraints, and highly time consuming computation as described in Sec. 4.2.1, this has not been feasible.

4.5 Evaluation of Multiple Box-shaped Scatterers

4.5.1 Comparison Between Two Coupled and Two Duplicated Scatterers

In this section, results from simulations of different approaches are compared. One approach involves calculating the surface current on a single box and then duplicating said box as an approximation of a coupled system. The other approach involves calculating the coupled system directly, however, this approach is around four times as time consuming as the duplication approach, as there are twice the amount of points that must be integrated over, which can be calculated as in Sec. 4.2.1.

4.5.1.1 Evaluation of the Surface Current

From Fig. 4.15 it can be seen that the current for a coupled system is larger and more concentrated around the middle of the antenna with a slight inclination towards the side that is facing the other antenna. The current distributions are, however, very similar for the two cases, but the coupled case has a larger current density roughly scaled by $\frac{23.6}{19.5} = 1.21$. To determine whether or not the duplication approximation is viable it is also necessary to examine the differential scattering cross section.

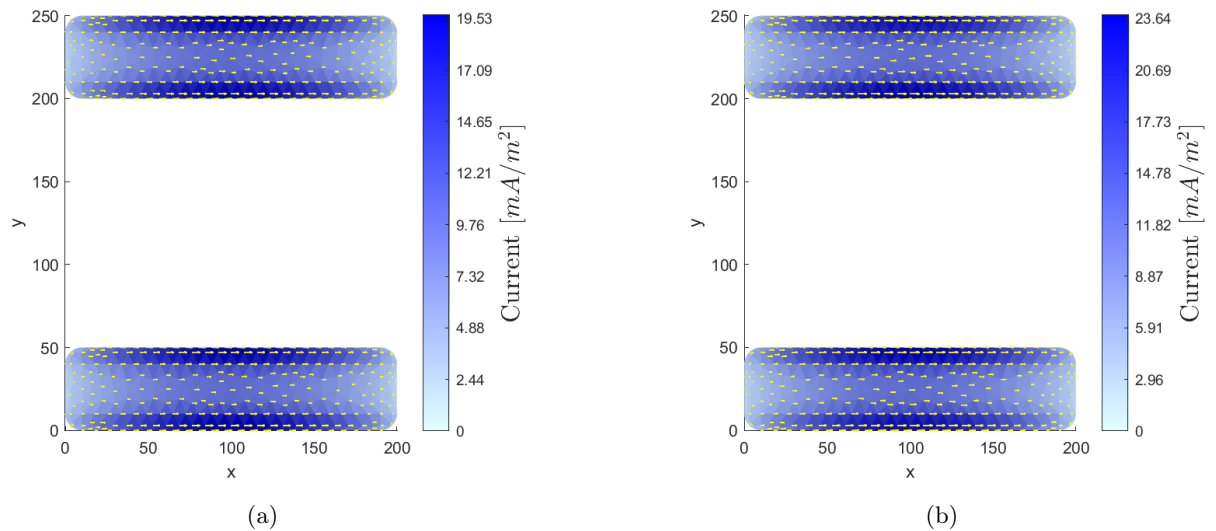


Figure 4.15: The surface current of **a)** duplicated box antennas and **b)** coupled box antennas.

4.5.1.2 Evaluation of the Differential Scattering Cross Section

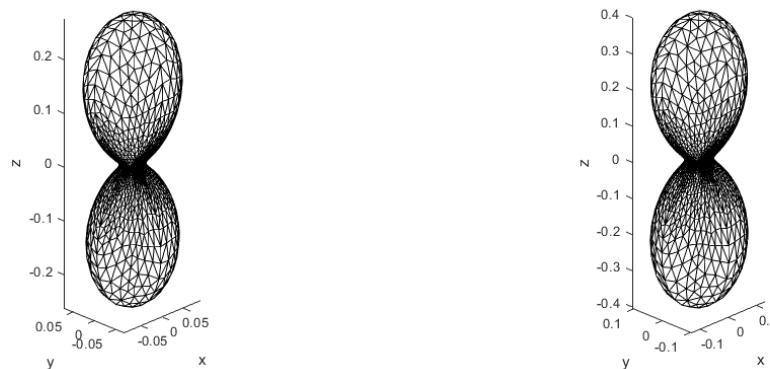


Figure 4.16: The differential scattering cross section of **a)** duplicated box antennas and **b)** coupled box antennas. Here the scattering cross section is 0.164 for two duplicated antennas and 0.630 for the coupled antennas

In Fig. 4.16 it can be seen that the magnitude of the scattering differential cross section of the duplication approximation is 26.0% of that of the coupled antennas. With the field being proportional to the current, while the scattering cross section being proportional to the field squared, the coupled case may be expected to have a DSCS scaled by $(23.6/19.5)^2 = 1.47$. This is seen in the z -direction, where they are respectively 0.278 and 0.401, which have a ratio of 1.45, which is in good correspondence. However, this match is not as good in other directions as seen by the scattering cross sections as the coupled case has a wider DSCS, which may be due to less cancellation of the fields, likely due to a translational asymmetry.

Thus the duplication approximation can be said to give a similar pattern as the coupled case,

albeit with a lower magnitude.

4.5.2 Multiple Box Antennas on a Layered Structure

4.5.2.1 Evaluation of the Surface Current

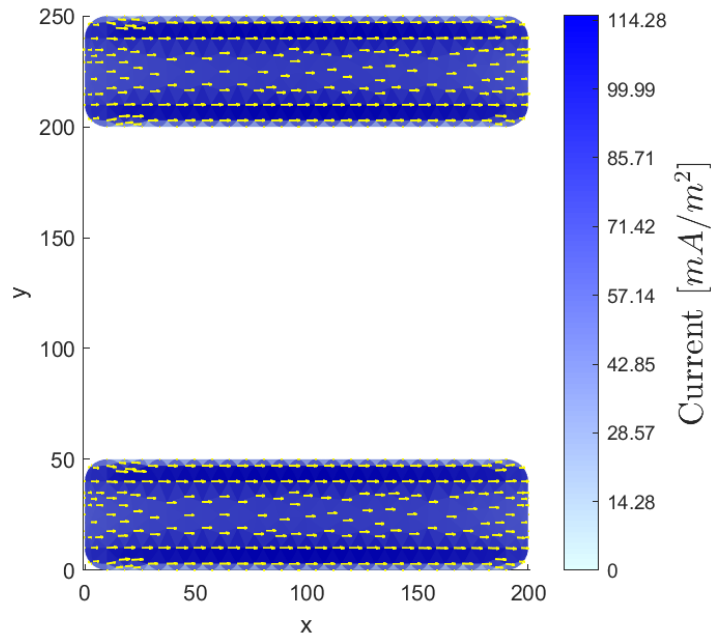


Figure 4.17: The surface current on two coupled box antennas on a dielectric substrate.

For the case of two coupled antennas placed on a dielectric substrate, where the ratio $\frac{\lambda}{l} = 2$ in order to compare with the corresponding configuration with no substrate. Here It is seen that the surface current is greatly increase as opposed to the coupled case without a substrate seen in Fig. 4.15. Otherwise, the current distribution looks similar as for a single scatterer on a substrate.

4.5.2.2 Evaluation of the Differential Scattering Cross Section

Here around 21.6% is scattered away form the substrate, while the rest is transmitted into the substrate. Most of the transmitted power is at an angle 16.9° from the substrate normal exactly as in the case for a single scatterer, while the smaller secondary lobes are about at an angle of 39.4° from the substrate normal.

4.5.3 Evaluation of the Differential Scattering Cross Section for Multiple Duplicated Scatterers

This section focuses on exploring the effects on the differential scattering cross section of multiple box antennas, both by multiple evenly distributed antennas and two antennas at varying distances. For all calculations the duplication approximation has been used in order to save on computation time, which is fair as the patterns will be roughly same, but the magnitude of the differential

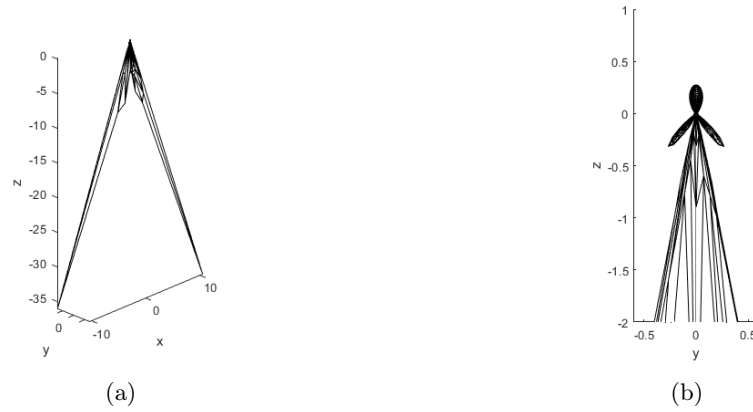


Figure 4.18: The differential scattering cross section of two coupled box antennas on a dielectric substrate seen **a** from the side and **b** zoomed in around the top where the backscattered part is shown.

scattering cross section will be somewhat smaller.

4.5.3.1 Evaluation of the Differential Scattering Cross Section Dependence of the Number of Scatterers

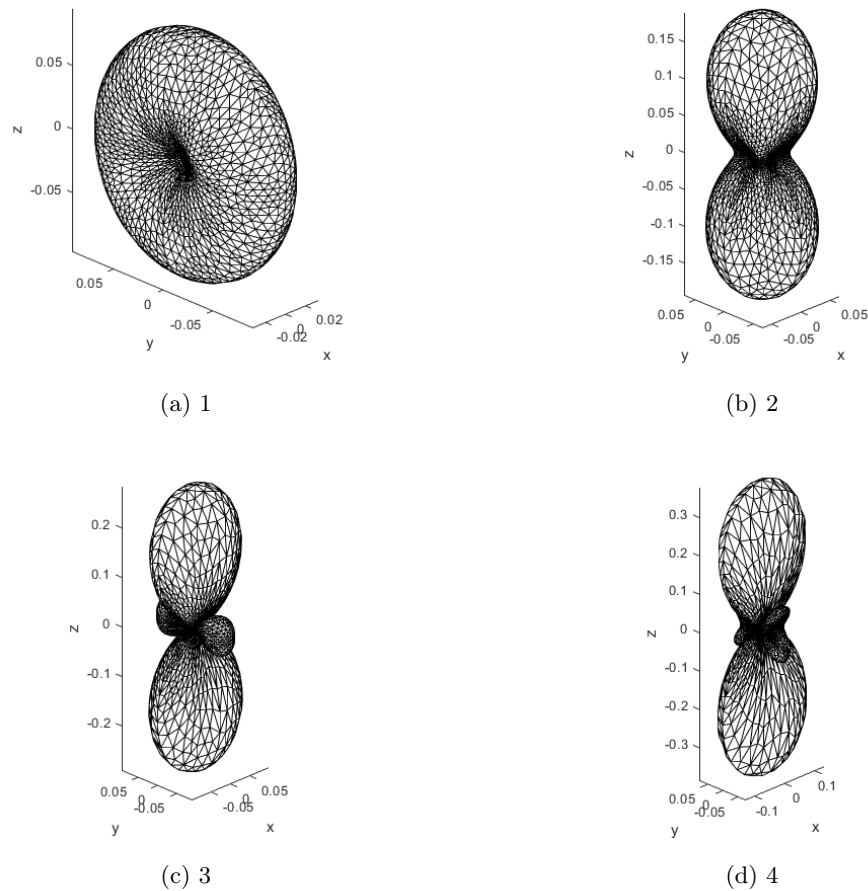


Figure 4.19: The differential scattering cross section of 1-4 duplicated box antennas placed a distance of $\lambda/2$ from each other.

From Fig. 4.19 it can be seen that when the amount of antennas is increased the differential scattering cross section becomes more narrow and more directionalised, which means that it is possible to direct the field in a specific direction, which is a useful property for an antenna. For even numbers of antennas destructive interference is observed in the y -direction, however for uneven numbers there will always be an antenna contribution that is not cancelled by another antenna.

4.5.3.2 Evaluation of the Differential Scattering Cross Section dependence of the Distance Between the Scatterers

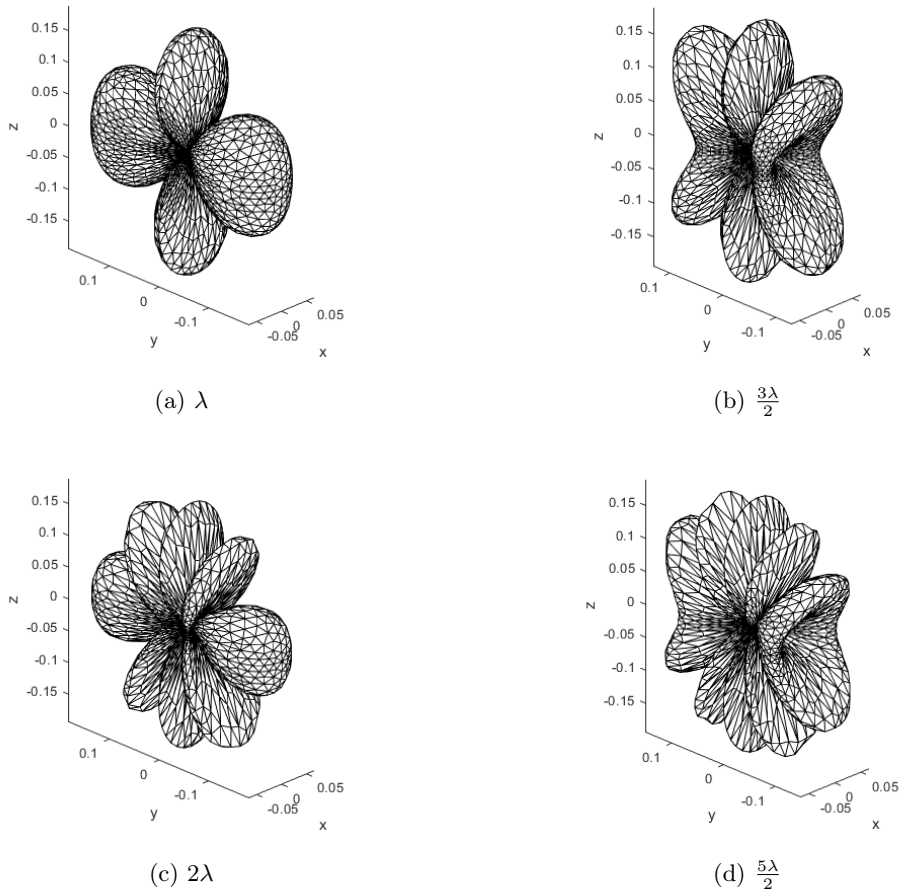


Figure 4.20: The differential scattering cross section of 2 duplicated box antennas placed a varying distance of λ to $5\lambda/2$ apart.

The results in Fig. 4.20 corresponds very well to the theoretical results obtained in Sec. 2.5, as there is constructive interference in the z -direction in every case as this is when $\hat{\mathbf{r}} \perp \Delta\mathbf{r}$. Furthermore the only cases where there is a contribution along in y -direction is for distances of integer times λ . The angles of the lobes can be determined by considering the scalar product $k_1 \hat{\mathbf{r}} \cdot \Delta\mathbf{r} = n2\pi \Leftrightarrow n = \frac{\Delta r}{\lambda} \cos \alpha \Leftrightarrow \alpha = \cos^{-1} \frac{n\lambda}{\Delta r}$. In the simulation the angle can be determined by determining the coordinates at the tip of the lobe in the yz -plane and using $\alpha = \tan^{-1} z/y$. Theoretically the second lobe, i.e the 1st order, in Fig. 4.20c should appear at the angle $\alpha = \cos^{-1} \frac{1}{2} = 60^\circ$,

since $\Delta r = 2\lambda$, while for the simulation the angle is $\alpha = \tan^{-1} 16.5/10 = 58.8^\circ$, which is a fair correspondence.

Conclusion

In this report, the Green's Function Surface Integral Equation Method has been examined and implemented to obtain a method for calculating the surface current and far-field radiation patterns for different scatterers in different geometries.

Within the theory, the Green's tensor for the different geometries was found and used in order to obtain the surface current for the scatterer(s) in question. In the process of deriving an expression for the Green's tensors for the layered structure, multiple singularities were found, which could be subtracted and solved analytically.

In the far-field limit, modified Green's tensors were found and in turn used to find the surface current and differential scattering cross section, which were modelled and evaluated for a number of scattering problems.

Based on the simulations of the spherical PEC scatterer it has been observed that the GFSIEM is able to produce highly accurate results when the numerically obtained results are compared to an analytic solution. Here different simulation parameters were investigated and evaluated on their effect on the normalised error and computation time in relation to a reference configuration.

It was found, however, that the method is quite unstable at wavelengths small in comparison to the geometry in consideration, with little success in improvements by increasing the simulation parameters.

For the surface current on the antennas in free space it was found that current assumes the form of two standing waves, one large on the side facing the incident field and a second smaller one on the opposing side. Resonance was observed, when the wavelength corresponded to twice the path length between the two nodes of the current wave facing the incident field. Furthermore it was found that the surface current for multiple antennas was greater for coupled cases than for corresponding uncoupled antennas, otherwise the current distributions were fairly similar, albeit with some minor differences.

For antennas placed on a dielectric substrate, the surface current was found as a single standing wave along the antenna.

For antennas in free space the incident was observed to be scattered approximately evenly forwards and backwards. For the antennas on a dielectric substrate it was seen that most of the scattered fields of the antennas are coupled into the substrate.

Bibliography

- [1] Dong-Kyu Lee, Ji-Hun Kang, Junghoon Kwon, Jun-Seok Lee, Seok Lee, Deok Woo, Jae Hun Kim, Chang-Seon Song, Q-Han Park, and Minah Seo. Nano metamaterials for ultrasensitive terahertz biosensing. *Scientific Reports*, 7, 12 2017.
- [2] Dong-Kyu Lee, Ji-Hun Kang, Jun-Seok Lee, Hyo-Seok Kim, Kim Chulki, Jae Hun Kim, Taikjin Lee, Joo-Hiuk Son, Q-Han Park, and Minah Seo. Highly sensitive and selective sugar detection by terahertz nano-antennas. *Scientific reports*, 5, 06 2015.
- [3] Y. C. Shen, T. Lo, P. F. Taday, B. E. Cole, W. R. Tribe, and M. C. Kemp. Detection and identification of explosives using terahertz pulsed spectroscopic imaging. *Applied Physics Letters*, 86(24):241116, 2005.
- [4] Yu Tao, Anthony Fitzgerald, and Vincent Wallace. Non-contact, non-destructive testing in various industrial sectors with terahertz technology. *Sensors*, 20:712, 01 2020.
- [5] Frank Ospald, Wissem Zouaghi, René Beigang, Carsten Matheis, Joachim Jonuscheit, Benoit Recur, Jean-Paul Guillet, Patrick Mounaix, Wouter Vleugels, Pablo Venegas Bosom, et al. Aeronautics composite material inspection with a terahertz time-domain spectroscopy system. *Optical Engineering*, 53(3):031208, 2013.
- [6] Andrei V Lavrinenko, Jesper Lægsgaard, Niels Gregersen, Frank Schmidt, and Thomas Søndergaard. *Numerical methods in photonics*, volume 1. CRC Press, 2014.
- [7] Lukas Novotny and Bert Hecht. *Principles of Nano-Optics*. Cambridge University Press, 2nd edition, 2012.
- [8] Lukas Novotny. Optical antennas a new technology that can enhance light-matter interactions. *The Bridge*, 39(4), 2009.
- [9] Riccardo Piccoli, Andrea Rovere, Andrea Toma, Roberto Morandotti, and Luca Razzari. *Terahertz Nanoantennas for Enhanced Spectroscopy*. IntechOpen, 2017.
- [10] Magda O. El-Shenawee Nathan M. Burford. Review of terahertz photoconductive antenna technology. *Opt. Eng.*, 56(1)(010901), 2017.
- [11] Reza Safian, Galia Ghazi, and Nafiseh Mohammadian. Review of photomixing continuous-wave terahertz systems and current application trends in terahertz domain. *Opt. Eng.*, 58(11)(110901), 2019.

-
- [12] Thomas M. Søndergaard, Mikkel O. Sauer, Carl E. M. Nielsen, Lars Merring Mikkelsen, Christian B. Sørensen, and Esben Skovsen. Theoretical analysis of compact cylindrical microlenses for terahertz photoconductive antennas in the photomixer regime. *Journal of the Optical Society of America B*, 37(3), 2020.
- [13] Mads Brincker, Peter Karlsen, Esben Skovsen, and Thomas Søndergaard. Microstructured gradient-index lenses for thz photoconductive antennas. *AIP Advances*, 6(025015), (2016).
- [14] Christian Buhl Sørensen. *Compact array emitters for terahertz spectroscopy and imaging*. PhD thesis, Aalborg University, 2019.
- [15] Thomas Søndergaard. *Green's Function Integral Equation Methods in Nano-Optics*, volume 1. CRC Press, 2019.
- [16] John D. Jackson. *Classical Electrodynamics*. New York: Wiley, 3rd edition, 1999.
- [17] Murray R. Spiegel, Seymour Lipschutz, and John Liu. *Mathematical Handbook of Formulas and Tables*. McGraw-Hill, 3rd edition, 2009.
- [18] Andrew Pressley. *Elementary Differential Geometry*. Springer, 2nd edition, 2010.
- [19] Keith H. Burns and Marian Gidea. *Differential geometry and topology with a view to dynamical systems*. Chapman & Hall/CRC, 2005.
- [20] D. Basu. *Dictionary of Pure and Applied Physics*. Comprehensive dictionary of physics. CRC Press, 2018.
- [21] Sina Vaezi, S. Nikmehr, and ali Pourziad. Nano-antenna synthesis for end-fire and pencil-beam far-field radiation patterns using vector spherical wave functions. *IET Microwaves, Antennas and Propagation*, 14, 05 2020.
- [22] Cecilie Rønne, L. LarsThrane, Per-Olof Åstrand, Anders Wallqvist, Kurt Mikkelsen, and Søren Keiding. Investigation of the temperature dependence of dielectric relaxation in liquid water by thz reflection spectroscopy and molecular dynamics simulation. *The Journal of Chemical Physics*, 107:5319–5331, 10 1997.
- [23] Thomas Garm Pedersen. Electric, optical and magnetic properties of nanostructures.
- [24] George B. Arfken and Hans J. Weber. *Mathematical methods for physicists 6th ed*. Elsevier Academic Press, 2005.

Boundary Conditions

The derivation of the boundary conditions presented here is based on [7, Sec. 2.10].

In Sec. 2.1 the general wave equations (Eq. (2.3))

$$\begin{aligned} -\nabla \times \nabla \times \mathbf{E}(\mathbf{r}) + k_0^2 \varepsilon(\mathbf{r}) \mathbf{E}(\mathbf{r}) &= -i\omega\mu_0 \mathbf{J}(\mathbf{r}), \\ -\nabla \times \frac{1}{\varepsilon(\mathbf{r})} \nabla \times \mathbf{H}(\mathbf{r}) + k_0^2 \mathbf{H}(\mathbf{r}) &= -\nabla \times \frac{1}{\varepsilon(\mathbf{r})} \mathbf{J}(\mathbf{r}), \end{aligned}$$

were derived using Maxwell's equations. Within said section it was further discussed that boundary conditions had to be in place in order to ensure continuity of both the electric- and the magnetic fields across interfaces. These boundary conditions can be found by applying Gauss's theorem and Stokes' law

$$\int_V \nabla \cdot \mathbf{A} d^3r = \oint_S \hat{\mathbf{n}} \cdot \mathbf{A} d^2r \quad \text{Gauss's theorem,} \quad (\text{A.1a})$$

$$\int_S \nabla \times \mathbf{A} \cdot \hat{\mathbf{n}} d^2r = \oint_L \hat{\mathbf{n}} \cdot \mathbf{A} dr \quad \text{Stokes' Law,} \quad (\text{A.1b})$$

to the Maxwell equations presented in Eq. (2.2), which yields

$$\oint_S \hat{\mathbf{n}} \cdot \mathbf{E}(\mathbf{r}) d^2r = \frac{1}{\varepsilon_0} \int_V \frac{\rho(\mathbf{r})}{\varepsilon(\mathbf{r})} d^3r, \quad (\text{A.2a})$$

$$\oint_S \hat{\mathbf{n}} \cdot \mathbf{H}(\mathbf{r}) d^2r = 0, \quad (\text{A.2b})$$

$$\oint_L \hat{\mathbf{n}} \cdot \mathbf{E}(\mathbf{r}) \cdot \hat{\mathbf{n}} dr = i\omega\mu_0 \int_S \mathbf{H}(\mathbf{r}) d^2r, \quad (\text{A.2c})$$

$$\oint_L \hat{\mathbf{n}} \cdot \mathbf{H}(\mathbf{r}) dr = \int_S (\mathbf{J}(\mathbf{r}) - i\omega\varepsilon_0\varepsilon(\mathbf{r})\mathbf{E}(\mathbf{r})) \cdot \hat{\mathbf{n}} d^2r. \quad (\text{A.2d})$$

In order to derive the appropriate boundary conditions from these equations it is useful to consider a single interface between the scatterer and the surrounding media, as can be seen in Fig. A.1.

In Eq. (A.2a) and Eq. (A.2b) a volume integral has to be evaluated on the RHS and Fig. A.1a is therefore considered for the evaluation of these two equations, while Fig. A.1b is used in the evaluation of Eq. (A.2c) and Eq. (A.2d) due to the surface integral on the RHS.

If the expressions in Eq. (A.2) are evaluated for $l \rightarrow 0$, the boundary conditions can be found to

be

$$\hat{\mathbf{n}} \cdot (\varepsilon_2 \mathbf{E}_2(\mathbf{r}) - \varepsilon_1 \mathbf{E}_1(\mathbf{r})) = \frac{\rho_s(\mathbf{r})}{\varepsilon_0} \quad ; \quad \rho_s = \rho l, \quad (\text{A.3a})$$

$$\hat{\mathbf{n}} \cdot (\mathbf{H}_2(\mathbf{r}) - \mathbf{H}_1(\mathbf{r})) = 0, \quad (\text{A.3b})$$

$$\hat{\mathbf{n}} \times (\mathbf{E}_2(\mathbf{r}) - \mathbf{E}_1(\mathbf{r})) = 0, \quad (\text{A.3c})$$

$$\hat{\mathbf{n}} \times (\mathbf{H}_2(\mathbf{r}) - \mathbf{H}_1(\mathbf{r})) = \mathbf{J}_s(\mathbf{r}) \quad ; \quad \mathbf{J}_s = \mathbf{J}l. \quad (\text{A.3d})$$

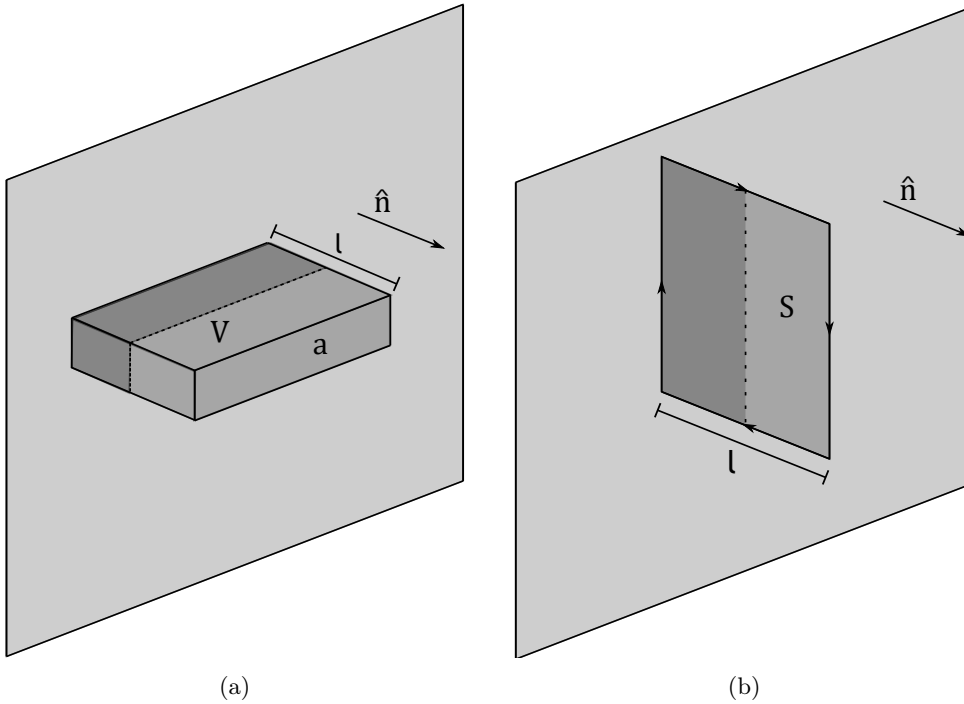


Figure A.1: Illustration of a single interface between the scatterer and the surrounding media. **a**) a box-shaped volume ($V = al$) with equal parts on each side of the interface and **b**) a plane perpendicular to the interface with equal parts on each side of the interface. Inspired by [7, Fig. 2.1].

Weyl Expansion

In this appendix, the Green's function, $g(\mathbf{r}, \mathbf{r}')$, from Eq. (2.19), which can be recalled as

$$g(\mathbf{r}, \mathbf{r}') = \frac{e^{ik_0\sqrt{\varepsilon}|\mathbf{r}-\mathbf{r}'|}}{4\pi|\mathbf{r}-\mathbf{r}'|},$$

is expressed in cylindrical coordinates by using the Weyl expansion. From its defining wave equation in Eq. (2.17), an eigenvalue problem may be stated as

$$(\nabla^2 + k_0^2\varepsilon_1)E_\lambda(\mathbf{r}) = \lambda E_\lambda(\mathbf{r}) \quad (\text{B.1})$$

which may be rewritten such that

$$(\nabla^2 + k^2)E_{\mathbf{k}}(\mathbf{r}) = 0, \quad (\text{B.2})$$

where $k^2 = k_0^2\varepsilon_1 - \lambda_{\mathbf{k}}$, with the solution $E_{\mathbf{k}} = e^{i\mathbf{k}\cdot\mathbf{r}}$. Now the Green's function may be expressed as

$$g(\mathbf{r}, \mathbf{r}') = - \int \frac{E_{\mathbf{k}}(\mathbf{r})E_{\mathbf{k}}(\mathbf{r}')^*}{(2\pi)^3\lambda_{\mathbf{k}}} d^3k, \quad (\text{B.3})$$

which can be shown to be a solution to the wave equation by applying the differential operator from the LHS of Eq. (B.1) to this expression, then using Eq. (B.2) before lastly using the inverse Fourier transform,

$$\frac{1}{(2\pi)^3} \int e^{i\mathbf{k}\cdot(\mathbf{r}-\mathbf{r}')} dk^3 = \delta(\mathbf{r}-\mathbf{r}'). \quad (\text{B.4})$$

Now, by factorising $\lambda_{\mathbf{k}}$ and adding a small imaginary term in the denominator, the Green's function may be stated as

$$g(\mathbf{r}, \mathbf{r}') = \int_{-\infty}^{\infty} \frac{e^{i\mathbf{k}\cdot(\mathbf{r}-\mathbf{r}')}}{(2\pi)^3 \left(k_z - \left(\sqrt{k_0^2\varepsilon_1 - k_\rho^2} + i\alpha\right)\right) \left(k_z + \sqrt{k_0^2\varepsilon_1 - k_\rho^2} + i\alpha\right)} d^3k, \quad (\text{B.5})$$

in the limit of $\alpha \rightarrow 0^+$, where it has been used that $k^2 = k_\rho^2 + k_z^2$. Focusing on the integral over k_z , the integrand goes to zero at infinity as long as the real part of $ik_z(z - z')$ remains negative, hence for e.g. $z > z'$, the integration path may be extended into the complex plane with an upper semicircle in order to form a closed path, such that the pole $k_z = \sqrt{k_0^2\varepsilon_1 - k_\rho^2} + i\alpha$ is enclosed within the path if α is chosen in the positive limit. As the integrand is holomorphic, i.e. complex differentiable in the neighbourhood of every point of its domain, the residue theorem may be

applied, which for first order poles located at z_1, \dots, z_n inside a closed path, C , yields[15, p. 381]

$$\oint_C f(z)dz = 2\pi i \sum_{j=1}^n \lim_{z \rightarrow z_j} (z - z_j)f(z), \quad (\text{B.6})$$

for a function f , in which case Eq. (B.5) yields

$$g(\mathbf{r}, \mathbf{r}') = \frac{i}{2} \frac{1}{(2\pi)^2} \int_{-\infty}^{\infty} \int_{-\infty}^{\infty} \frac{e^{ik_x(x-x')} e^{ik_y(y-y')} e^{ik_{z,1}|z-z'|}}{k_{z,1}} dk_x dk_y, \quad (\text{B.7})$$

from its pole when integrating over k_z , which is known as the Weyl expansion of the green's function. Here the correct pole was obtained by choosing α in the positive limit resulting in the radiating boundary condition being satisfied. If $z < z'$ the opposite sign pole is obtained, so the exponent remains the same if z and z' are interchanged, hence the absolute sign.

Derivation of the Green's Function for a Layered Structure

In Sec. 2.4.1 an outset was taken in the expression for $g(\mathbf{r}, \mathbf{r}')$, which was derived in App. B, Eq. (B.7), which can be recalled as

$$g(\mathbf{r}, \mathbf{r}') = \frac{i}{2} \frac{1}{(2\pi)^2} \int_{-\infty}^{\infty} \int_{-\infty}^{\infty} \frac{e^{ik_x(x-x')} e^{ik_y(y-y')} e^{ik_{z,1}|z-z'|}}{k_{z,1}} dk_x dk_y,$$

which in turn could be used in order to derive, first the direct Green's tensor, presented in Eq. (2.78), and from that the indirect and the transmitted Green's tensors, presented in Eq. (2.79). This appendix will aim to provide the reader with a more in-depth derivation, following [15, Sec. 6.3].

By applying

$$\begin{aligned} k_x &= k_\rho \cos \varphi_k, \\ k_y &= k_\rho \sin \varphi_k, \\ x - x' &= \rho_r \cos \varphi_r, \\ y - y' &= \rho_r \sin \varphi_r, \end{aligned}$$

to the expression for $g(\mathbf{r}, \mathbf{r}')$, it can be converted into cylindrical coordinates as

$$g(\mathbf{r}, \mathbf{r}') = \frac{i}{2} \frac{1}{(2\pi)^2} \int_0^\infty \int_0^{2\pi} \frac{e^{ik_\rho \rho_r \cos(\varphi_k - \varphi_r)} e^{ik_{z,1}|z-z'|}}{k_{z,1}} k_\rho dk_\rho d\varphi_k, \quad (\text{C.1})$$

by using $\cos(\varphi_k - \varphi_r) = \cos \varphi_k \cos \varphi_r + \sin \varphi_k \sin \varphi_r$. Next the definition of the 0th order Bessel function,

$$\mathcal{J}_0(x) = \frac{1}{2\pi} \int_0^{2\pi} e^{ix \cos \theta} d\theta,$$

can be used in order to further reduce the expression for the scalar Green's function in order to obtain

$$g(\mathbf{r}, \mathbf{r}') = \frac{i}{4\pi} \int_0^\infty \frac{\mathcal{J}_0(k_\rho \rho_r) e^{ik_{z,1}|z-z'|}}{k_{z,1}} k_\rho dk_\rho, \quad (\text{C.2})$$

where it has been used that the integral is independent of φ_r , since the integral is over a full period.

The direct dyadic Green's tensor in cylindrical coordinates can then be obtained by inserting this cylindrical expression for the scalar Green's function into the expression for the dyadic Green's

tensor in free space, yielding

$$\vec{\mathbf{G}}^{(d)}(\mathbf{r}, \mathbf{r}') = \left(\vec{\mathbf{Y}} + \frac{1}{k_1^2} \nabla \nabla \right) \frac{i}{4\pi} \int_0^\infty \frac{\mathcal{J}_0(k_\rho \rho_r) e^{ik_{z,1}|z-z'|}}{k_{z,1}} k_\rho dk_\rho. \quad (\text{C.3})$$

By using that $\vec{\mathbf{Y}} = \hat{\rho}_r \hat{\rho}_r + \hat{\varphi}_r \hat{\varphi}_r + \hat{\mathbf{z}} \hat{\mathbf{z}}$ along with the relations between Cartesian and cylindrical coordinates for the unit vectors,

$$\begin{aligned} \hat{\rho}_r &= \hat{\mathbf{x}} \cos \varphi_r + \hat{\mathbf{y}} \sin \varphi_r, \\ \hat{\varphi}_r &= -\hat{\mathbf{x}} \sin \varphi_r + \hat{\mathbf{y}} \cos \varphi_r, \\ \hat{\mathbf{x}} &= \hat{\rho}_r \cos \varphi_r - \hat{\varphi}_r \sin \varphi_r, \\ \hat{\mathbf{y}} &= \hat{\rho}_r \sin \varphi_r + \hat{\varphi}_r \cos \varphi_r, \end{aligned}$$

and the gradient in cylindrical coordinates being given as

$$\nabla = \hat{\mathbf{z}} \frac{\partial}{\partial z} + \hat{\rho}_r \frac{\partial}{\partial \rho_r} + \hat{\varphi}_r \frac{1}{\rho_r} \frac{\partial}{\partial \varphi_r},$$

the direct Green's tensor can be explicitly determined, as was done in Sec. 2.2.2.1. However, while the two gradients does not affect each other in Cartesian coordinates, this is not the case in cylindrical coordinates as $\hat{\rho}_r$ is a function of φ_r , hence

$$\begin{aligned} \frac{\partial}{\partial \varphi_r} \hat{\rho}_r &= \frac{\partial}{\partial \varphi_r} \hat{\mathbf{x}} \cos \varphi_r + \hat{\mathbf{y}} \sin \varphi_r \\ &= -\hat{\mathbf{x}} \sin \varphi_r + \hat{\mathbf{y}} \cos \varphi_r = \hat{\varphi}_r, \end{aligned} \quad (\text{C.4})$$

which leads to

$$\nabla \nabla = \left(\hat{\mathbf{z}} \frac{\partial}{\partial z} + \hat{\rho}_r \frac{\partial}{\partial \rho_r} + \hat{\varphi}_r \frac{1}{\rho_r} \frac{\partial}{\partial \varphi_r} \right) \left(\hat{\mathbf{z}} \frac{\partial}{\partial z} + \hat{\rho}_r \frac{\partial}{\partial \rho_r} + \hat{\varphi}_r \frac{1}{\rho_r} \frac{\partial}{\partial \varphi_r} \right) \quad (\text{C.5})$$

$$\begin{aligned} &= \hat{\mathbf{z}} \hat{\mathbf{z}} \frac{\partial^2}{\partial z^2} + \hat{\mathbf{z}} \hat{\rho}_r \frac{\partial}{\partial z} \frac{\partial}{\partial \rho_r} + \hat{\mathbf{z}} \hat{\varphi}_r \frac{1}{\rho_r} \frac{\partial}{\partial z} \frac{\partial}{\partial \varphi_r} \\ &\quad + \hat{\rho}_r \hat{\mathbf{z}} \frac{\partial}{\partial \rho_r} \frac{\partial}{\partial z} + \hat{\rho}_r \hat{\rho}_r \frac{\partial^2}{\partial \rho_r^2} + \hat{\rho}_r \hat{\varphi}_r \frac{1}{\rho_r} \frac{\partial}{\partial \rho_r} \frac{\partial}{\partial \varphi_r} \\ &\quad + \hat{\varphi}_r \hat{\mathbf{z}} \frac{1}{\rho_r} \frac{\partial}{\partial \varphi_r} \frac{\partial}{\partial z} + \hat{\varphi}_r \frac{1}{\rho_r} \left(\hat{\varphi}_r \frac{\partial}{\partial \rho_r} + \hat{\rho}_r \frac{\partial}{\partial \varphi_r} \frac{\partial}{\partial \rho_r} \right) + \hat{\varphi}_r \hat{\varphi}_r \frac{1}{\rho_r^2} \frac{\partial^2}{\partial \varphi_r^2}. \end{aligned} \quad (\text{C.6})$$

By using that $\frac{\partial}{\partial \varphi_r} g(\mathbf{r}, \mathbf{r}') = 0$, the second term in the direct Green's tensor can be found as

$$\begin{aligned} \nabla \nabla g(\mathbf{r}, \mathbf{r}') &= \left[\hat{\mathbf{z}} \hat{\mathbf{z}} \frac{\partial^2}{\partial z^2} + (\hat{\mathbf{z}} \hat{\rho}_r + \hat{\rho}_r \hat{\mathbf{z}}) \frac{\partial}{\partial z} \frac{\partial}{\partial \rho_r} + \hat{\rho}_r \hat{\rho}_r \frac{\partial^2}{\partial \rho_r^2} \right. \\ &\quad \left. + \hat{\varphi}_r \hat{\varphi}_r \frac{1}{\rho_r} \frac{\partial}{\partial \rho_r} \right] \left[\frac{i}{4\pi} \int_0^\infty \frac{\mathcal{J}_0(k_\rho \rho_r) e^{ik_{z,1}|z-z'|}}{k_{z,1}} k_\rho dk_\rho \right] \\ &= \frac{i}{4\pi} \int_{k_\rho=0}^\infty \left[-\hat{\mathbf{z}} \hat{\mathbf{z}} k_{z,1}^2 \mathcal{J}_0(k_\rho \rho_r) + (\hat{\mathbf{z}} \hat{\rho}_r + \hat{\rho}_r \hat{\mathbf{z}}) ik_{z,1} k_\rho \frac{z-z'}{|z-z'|} \mathcal{J}_0'(k_\rho \rho_r) \right. \\ &\quad \left. + \hat{\rho}_r \hat{\rho}_r k_\rho^2 \mathcal{J}_0''(k_\rho \rho_r) + \hat{\varphi}_r \hat{\varphi}_r \frac{k_\rho}{\rho_r} \mathcal{J}_0'(k_\rho \rho_r) \right] e^{ik_{z,1}|z-z'|} \frac{k_\rho}{k_{z,1}} dk_\rho, \end{aligned} \quad (\text{C.7})$$

hence the direct Green's tensor in its entirety is given as

$$\begin{aligned} \overleftrightarrow{\mathbf{G}}^{(d)}(\mathbf{r}, \mathbf{r}') = & \frac{i}{4\pi} \int_0^\infty \left[\hat{\boldsymbol{\rho}}_r \hat{\boldsymbol{\rho}}_r \left(\mathcal{J}_0(k_\rho \rho_r) + \frac{k_\rho^2}{k_1^2} \mathcal{J}_0''(k_\rho \rho_r) \right) + (\hat{\mathbf{z}} \hat{\boldsymbol{\rho}}_r + \hat{\boldsymbol{\rho}}_r \hat{\mathbf{z}}) \frac{ik_{z,1} k_\rho}{k_1^2} \frac{z - z'}{|z - z'|} \mathcal{J}_0'(k_\rho \rho_r) \right. \\ & \left. + \hat{\mathbf{z}} \hat{\mathbf{z}} \frac{k_\rho^2}{k_1^2} \mathcal{J}_0(k_\rho \rho_r) + \hat{\boldsymbol{\varphi}}_r \hat{\boldsymbol{\varphi}}_r \left(\mathcal{J}_0(k_\rho \rho_r) + \frac{k_\rho^2}{k_1^2} \frac{\mathcal{J}_0'(k_\rho \rho_r)}{k_\rho \rho_r} \right) \right] e^{ik_{z,1}|z-z'|} \frac{k_\rho}{k_{z,1}} dk_\rho, \end{aligned} \quad (\text{C.8})$$

where it in the $\hat{\mathbf{z}}\hat{\mathbf{z}}$ -component has been used that the $\hat{\mathbf{z}}\hat{\mathbf{z}}$ -component of $\overleftrightarrow{\mathbf{T}}$ can be written as $\hat{\mathbf{z}}\hat{\mathbf{z}} \frac{k_1^2}{k_1^2}$ along with $k_\rho^2 = k_1^2 - k_{z,1}^2$.

Now it is assumed that the interface between the homogeneous media and the infinite substrate is in $z = 0$, such that

$$\varepsilon_{\text{ref}} = \begin{cases} \varepsilon_1, & z > 0 \\ \varepsilon_3, & z < 0 \end{cases}. \quad (\text{C.9})$$

The Green's tensor can then be constructed for this structure and with $z' > 0$, where the incident field for $z' > z > 0$ is given by

$$\begin{aligned} \mathbf{E}_{i,z}(\mathbf{r}) = & \overleftrightarrow{\mathbf{G}}^{(d)}(\mathbf{r}, \mathbf{r}') \cdot \hat{\mathbf{z}} \\ = & \frac{i}{4\pi} \int_0^\infty \left(\hat{\mathbf{z}} \mathcal{J}_0(k_\rho \rho_r) \frac{k_\rho^2}{k_1^2} - \hat{\boldsymbol{\rho}}_r \frac{ik_{z,1} k_\rho}{k_1^2} \mathcal{J}_0'(k_\rho \rho_r) \right) e^{ik_{z,1}(z'-z)} \frac{k_\rho}{k_{z,1}} dk_\rho, \end{aligned} \quad (\text{C.10})$$

which can be thought of as a sum of p-polarised waves propagating towards the interface, due to $\hat{\mathbf{z}}$ component. The reflected¹ and transmitted fields for each wave are then given by Fresnel reflection, hence, the reflected and transmitted fields can be written as

$$\mathbf{E}_{r,z}(\mathbf{r}) = \frac{i}{4\pi} \int_0^\infty r^{(p)}(k_\rho) \left(\hat{\mathbf{z}} \mathcal{J}_0(k_\rho \rho_r) \frac{k_\rho^2}{k_1^2} + \hat{\boldsymbol{\rho}}_r \frac{ik_{z,1} k_\rho}{k_1^2} \mathcal{J}_0'(k_\rho \rho_r) \right) e^{ik_{z,1}(z'+z)} \frac{k_\rho}{k_{z,1}} dk_\rho, \quad (\text{C.11a})$$

$$\mathbf{E}_{t,z}(\mathbf{r}) = \frac{i}{4\pi} \int_0^\infty t^{(p)}(k_\rho) \frac{\varepsilon_1}{\varepsilon_3} \left(\hat{\mathbf{z}} \mathcal{J}_0(k_\rho \rho_r) \frac{k_\rho^2}{k_1^2} + \hat{\boldsymbol{\rho}}_r \frac{ik_{z,3} k_\rho}{k_1^2} \mathcal{J}_0'(k_\rho \rho_r) \right) e^{ik_{z,1}z'} e^{-ik_{z,3}z} \frac{k_\rho}{k_{z,1}} dk_\rho, \quad (\text{C.11b})$$

where

$$r^{(p)}(k_\rho) = \frac{E_r^{(p)}}{E_i^{(p)}} = \frac{\varepsilon_3 k_{z,1} - \varepsilon_1 k_{z,3}}{\varepsilon_3 k_{z,1} + \varepsilon_1 k_{z,3}}, \quad (\text{C.12a})$$

$$t^{(p)}(k_\rho) = \frac{n_3 E_t^{(p)}}{n_1 E_i^{(p)}} = 1 + r^{(p)}(k_\rho), \quad (\text{C.12b})$$

are the Fresnel reflection and transmission coefficients for p-polarised light. Here the transmission coefficient is unconventionally, but conveniently, defined as the components of the field may be related as

$$E_{t\perp}^{(p)} = E_t^{(p)} \sin \theta_3 = \frac{n_1}{n_3} E_i^{(p)} t^{(p)} \sin \theta_3 = \frac{\varepsilon_1}{\varepsilon_3} t^{(p)} E_i^{(p)} \sin \theta_1 = \frac{\varepsilon_1}{\varepsilon_3} t^{(p)} E_{i\perp}^{(p)} \quad (\text{C.13a})$$

$$E_{t\parallel}^{(p)} = E_t^{(p)} \cos \theta_3 = \frac{n_1}{n_3} E_i^{(p)} t^{(p)} \cos \theta_3 = \frac{n_1}{n_3} t^{(p)} E_{i\parallel}^{(p)} \frac{\cos \theta_3}{\cos \theta_1} = \frac{\varepsilon_1}{\varepsilon_3} \frac{k_{z,3}}{k_{z,1}} t^{(p)} E_{i\parallel}^{(p)}, \quad (\text{C.13b})$$

¹ \mathbf{E}_r represents the reflected field by the dielectric media on which the antenna is placed and should not be mistaken as being equal to \mathbf{E}_{scat} , presented in Sec. 2.2.2.2, which is the scattered field by the antenna itself.

where \parallel refers to the component parallel to the interface while \perp to the perpendicular component, and θ refers to the propagation angle from the interface normal, as can be seen in Fig. C.1. Here Snell's law, that is $n_1 \sin \theta_1 = n_3 \sin \theta_3$, and $k_{z,i} = k_0 n_i \cos \theta_i$ has been used.

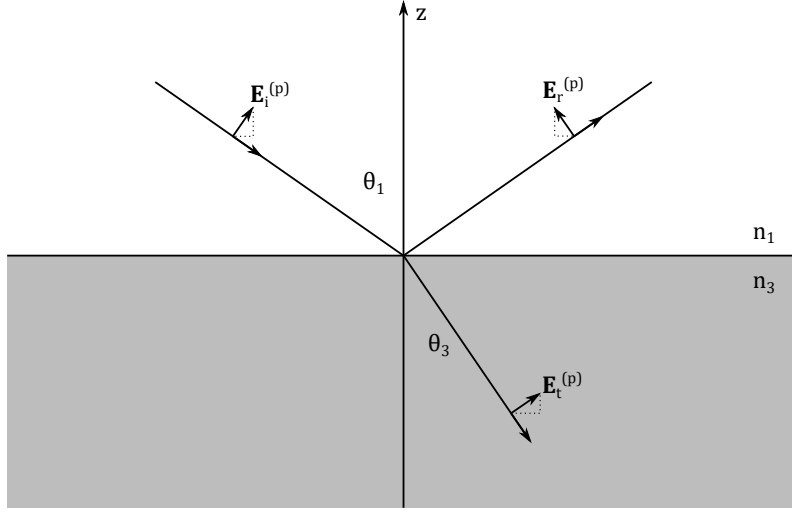


Figure C.1: Illustration of the incident and the transmitted electric field.

Now, consider the incident field in the $\hat{\mathbf{x}}$ -direction, given by

$$\mathbf{E}_{i,x}(\mathbf{r}) = \overleftrightarrow{\mathbf{G}}^{(d)}(\mathbf{r}, \mathbf{r}') \cdot \hat{\mathbf{x}} = \mathbf{E}_{i,x}^{(s)}(\mathbf{r}) + \mathbf{E}_{i,x}^{(p)}(\mathbf{r}), \quad (\text{C.14})$$

where both the s- and p-polarised components of the field are divergence-free, they satisfy the wave equation and are given by

$$\mathbf{E}_{i,x}^{(s)}(\mathbf{r}) = \frac{i}{4\pi} \int_0^\infty \left(\hat{\varphi}_r \sin \varphi_r \mathcal{J}_0''(k_\rho \rho_r) - \hat{\rho}_r \cos \varphi_r \frac{\mathcal{J}_0'(k_\rho \rho_r)}{k_\rho \rho_r} \right) e^{ik_{z,1}(z'-z)} \frac{k_\rho}{k_{z,1}} dk_\rho, \quad (\text{C.15a})$$

$$\mathbf{E}_{i,x}^{(p)}(\mathbf{r}) = \frac{i}{4\pi} \int_0^\infty \left(\hat{\varphi}_r \sin \varphi_r \frac{k_{z,1}^2}{k_1^2} \frac{\mathcal{J}_0'(k_\rho \rho_r)}{k_\rho \rho_r} - \hat{\rho}_r \cos \varphi_r \frac{k_{z,1}^2}{k_1^2} \mathcal{J}_0''(k_\rho \rho_r) + \hat{\mathbf{z}} \cos \varphi_r \frac{-ik_{z,1} k_\rho}{k_1^2} \mathcal{J}_0'(k_\rho \rho_r) \right) e^{ik_{z,1}(z'-z)} \frac{k_\rho}{k_{z,1}} dk_\rho, \quad (\text{C.15b})$$

where the recurrence relation $\mathcal{J}_0''(x) = -\mathcal{J}_0(x) - \frac{1}{x} \mathcal{J}_0'(x)$ has been utilised, while it can be recalled that $\hat{\mathbf{x}} = \hat{\rho}_r \cos \varphi_r - \hat{\varphi}_r \sin \varphi_r$. Now the total x -component of the field can be written as

$$\mathbf{E}_x(\mathbf{r}) = \begin{cases} \mathbf{E}_{i,x}^{(s)}(\mathbf{r}) + \mathbf{E}_{i,x}^{(p)}(\mathbf{r}) + \mathbf{E}_{r,x}^{(s)}(\mathbf{r}) + \mathbf{E}_{r,x}^{(p)}(\mathbf{r}), & z > 0 \\ \mathbf{E}_{i,x}^{(s)}(\mathbf{r}) + \mathbf{E}_{i,x}^{(p)}(\mathbf{r}) & z < 0 \end{cases}, \quad (\text{C.16})$$

where, like for the z -component, the reflected and transmitted field can be found by Fresnel

reflection as

$$\mathbf{E}_{r,x}^{(s)}(\mathbf{r}) = \frac{i}{4\pi} \int_0^\infty \left(\hat{\varphi}_r \sin \varphi_r \mathcal{J}_0''(k_\rho \rho_r) - \hat{\rho}_r \cos \varphi_r \frac{\mathcal{J}_0'(k_\rho \rho_r)}{k_\rho \rho_r} \right) r^{(s)}(k_\rho) e^{ik_{z,1}(z+z')} \frac{k_\rho}{k_{z,1}} dk_\rho, \quad (\text{C.17a})$$

$$\mathbf{E}_{r,x}^{(p)}(\mathbf{r}) = \frac{i}{4\pi} \int_0^\infty \left(-\hat{\varphi}_r \sin \varphi_r \frac{k_{z,1}^2}{k_1^2} \frac{\mathcal{J}_0'(k_\rho \rho_r)}{k_\rho \rho_r} + \hat{\rho}_r \cos \varphi_r \frac{k_{z,1}^2}{k_1^2} \mathcal{J}_0''(k_\rho \rho_r) + \hat{\mathbf{z}} \cos \varphi_r \frac{-ik_{z,1}k_\rho}{k_1^2} \mathcal{J}_0'(k_\rho \rho_r) \right) r^{(p)}(k_\rho) e^{ik_{z,1}(z+z')} \frac{k_\rho}{k_{z,1}} dk_\rho, \quad (\text{C.17b})$$

$$\mathbf{E}_{t,x}^{(s)}(\mathbf{r}) = \frac{i}{4\pi} \int_0^\infty \left(\hat{\varphi}_r \sin \varphi_r \mathcal{J}_0''(k_\rho \rho_r) - \hat{\rho}_r \cos \varphi_r \frac{\mathcal{J}_0'(k_\rho \rho_r)}{k_\rho \rho_r} \right) t^{(s)}(k_\rho) e^{ik_{z,1}z'} e^{-ik_{z,3}z} \frac{k_\rho}{k_{z,1}} dk_\rho, \quad (\text{C.17c})$$

$$\mathbf{E}_{t,x}^{(p)}(\mathbf{r}) = \frac{i}{4\pi} \int_0^\infty \left(\frac{k_{z,3}}{k_{z,1}} \left(\hat{\varphi}_r \sin \varphi_r \frac{k_{z,1}^2}{k_1^2} \frac{\mathcal{J}_0'(k_\rho \rho_r)}{k_\rho \rho_r} - \hat{\rho}_r \cos \varphi_r \frac{k_{z,1}^2}{k_1^2} \mathcal{J}_0''(k_\rho \rho_r) \right) + \hat{\mathbf{z}} \cos \varphi_r \frac{-ik_{z,1}k_\rho}{k_1^2} \mathcal{J}_0'(k_\rho \rho_r) \right) t^{(p)}(k_\rho) \frac{\varepsilon_1}{\varepsilon_3} e^{ik_{z,1}z'} e^{-ik_{z,3}z} \frac{k_\rho}{k_{z,1}} dk_\rho. \quad (\text{C.17d})$$

The Fresnel reflection and transmission coefficients for s-polarisation are given by

$$r^{(s)}(k_\rho) = \frac{E_r^{(s)}}{E_i^{(s)}} = \frac{k_{z,1} - k_{z,3}}{k_{z,1} + k_{z,3}}, \quad (\text{C.18a})$$

$$t^{(s)}(k_\rho) = \frac{E_t^{(s)}}{E_i^{(s)}} = 1 + r^{(s)}(k_\rho), \quad (\text{C.18b})$$

while they for p-polarisation can be recalled from Eq. (C.12).

A similar approach, as the one used for the x -component, can be taken for the incident field in the $\hat{\mathbf{y}}$ direction, where

$$\mathbf{E}_{i,y}(\mathbf{r}) = \overleftrightarrow{\mathbf{G}}^{(d)}(\mathbf{r}, \mathbf{r}') \cdot \hat{\mathbf{y}}. \quad (\text{C.19})$$

Thus, by collecting the expressions for the different directions, an expression for the dyadic Green's tensor for a two-layer structure is obtained

$$\overleftrightarrow{\mathbf{G}}(\mathbf{r}, \mathbf{r}') \begin{cases} \overleftrightarrow{\mathbf{G}}^{(d)}(\mathbf{r}, \mathbf{r}') + \overleftrightarrow{\mathbf{G}}^{(i)}(\mathbf{r}, \mathbf{r}'), & z > 0, z' > 0 \\ \overleftrightarrow{\mathbf{G}}^{(t)}(\mathbf{r}, \mathbf{r}'), & z < 0, z' > 0 \end{cases}, \quad (\text{C.20})$$

where the incident and the transmitted Green's tensor are given as

$$\overleftrightarrow{\mathbf{G}}^{(i)}(\mathbf{r}, \mathbf{r}') = \mathbf{E}_{r,x} \hat{\mathbf{x}} + \mathbf{E}_{r,y} \hat{\mathbf{y}} + \mathbf{E}_{r,z} \hat{\mathbf{z}}, \quad (\text{C.21a})$$

$$\overleftrightarrow{\mathbf{G}}^{(t)}(\mathbf{r}, \mathbf{r}') = \mathbf{E}_{t,x} \hat{\mathbf{x}} + \mathbf{E}_{t,y} \hat{\mathbf{y}} + \mathbf{E}_{t,z} \hat{\mathbf{z}}, \quad (\text{C.21b})$$

which can furthermore be written as

$$\begin{aligned} \vec{\mathbf{G}}^{(i)}(\mathbf{r}, \mathbf{r}') = & \frac{i}{4\pi} \int_0^\infty \left\{ r^{(p)}(k_\rho) \left(\hat{\mathbf{z}}\hat{\mathbf{z}}\mathcal{J}_0(k_\rho\rho_r) \frac{k_\rho^2}{k_1^2} + \hat{\varphi}_r\hat{\varphi}_r \frac{\mathcal{J}'_0(k_\rho\rho_r)}{k_\rho\rho_r} \frac{k_{z,1}^2}{k_1^2} + \right. \right. \\ & \left. \left. \hat{\rho}_r\hat{\rho}_r\mathcal{J}_0''(k_\rho\rho_r) \frac{k_{z,1}^2}{k_1^2} - (\hat{\mathbf{z}}\hat{\rho}_r - \hat{\rho}_r\hat{\mathbf{z}}) \frac{ik_\rho k_{z,1}}{k_1^2} \mathcal{J}'_0(k_\rho\rho_r) \right) \right. \\ & \left. - r^{(s)}(k_\rho) \left(\hat{\varphi}_r\hat{\varphi}_r\mathcal{J}_0''(k_\rho\rho_r) + \hat{\rho}_r\hat{\rho}_r \frac{\mathcal{J}'_0(k_\rho\rho_r)}{k_\rho\rho_r} \right) \right\} e^{ik_{z,1}(z+z')} \frac{k_\rho}{k_{z,1}} dk_\rho, \end{aligned} \quad (\text{C.22a})$$

$$\begin{aligned} \vec{\mathbf{G}}^{(t)}(\mathbf{r}, \mathbf{r}') = & \frac{i}{4\pi} \int_0^\infty \left\{ t^{(p)}(k_\rho) \frac{\varepsilon_1}{\varepsilon_2} \left(\hat{\mathbf{z}}\hat{\mathbf{z}}\mathcal{J}_0(k_\rho\rho_r) \frac{k_\rho^2}{k_1^2} - \hat{\varphi}_r\hat{\varphi}_r \frac{\mathcal{J}'_0(k_\rho\rho_r)}{k_\rho\rho_r} \frac{k_{z,1}k_{z,3}}{k_1^2} \right. \right. \\ & \left. \left. - \hat{\rho}_r\hat{\rho}_r\mathcal{J}_0''(k_\rho\rho_r) \frac{k_{z,1}k_{z,3}}{k_1^2} - \left(\hat{\mathbf{z}}\hat{\rho}_r + \hat{\rho}_r\hat{\mathbf{z}} \frac{k_{z,3}}{k_{z,1}} \right) i \frac{k_\rho k_{z,1}}{k_{z,1}^2} \mathcal{J}'_0(k_\rho\rho_r) \right) \right. \\ & \left. - t^{(s)}(k_\rho) \left(\hat{\varphi}_r\hat{\varphi}_r\mathcal{J}_0''(k_\rho\rho_r) + \hat{\rho}_r\hat{\rho}_r \frac{\mathcal{J}'_0(k_\rho\rho_r)}{k_\rho\rho_r} \right) \right\} e^{ik_{z,1}z'} e^{-ik_{z,3}z} \frac{k_\rho}{k_{z,1}} dk_\rho. \end{aligned} \quad (\text{C.22b})$$

C.1 The Differential Scattering Cross Section Green's Tensor

In Sec. 2.4.2 the far-field Green's tensors were derived from the Green's tensors in Eq. (2.78) and Eq. (2.79), however, this appendix will provide a more detailed derivation than was provided in the Sec. 2.4.2.

First, consider the zz -component of the indirect Green's tensor in Eq. (2.79a), hence

$$G_{zz}^{(i)} = \frac{i}{4\pi} \int_0^\infty \mathcal{J}_0(k_\rho\rho_r) \frac{k_\rho^2}{k_1^2} r^{(p)}(k_\rho) e^{ik_{z,1}(z+z')} \frac{k_\rho}{k_{z,1}} dk_\rho. \quad (\text{C.23})$$

As stated in Sec. 2.4.2 z is large in the far-field and the integration interval can therefore be reduced to $0 \leq k_\rho \leq k_1$. By then applying the coordinate transformations,

$$z = r \cos \theta, \quad \rho = r \sin \theta, \quad 0 < \theta \leq \frac{\pi}{2}, \quad (\text{C.24a})$$

$$x = \rho \cos \varphi, \quad y = \rho \sin \varphi, \quad (\text{C.24b})$$

$$k_{z,1} = k_1 \cos \alpha, \quad k_\rho = k_1 \sin \alpha, \quad (\text{C.24c})$$

the integral reduces to

$$\mathbf{G}_{zz}^{(i,ff)} \approx \frac{i}{4\pi} \int_{\alpha=0}^{\frac{\pi}{2}} \mathcal{J}_0(k_\rho\rho_r) \frac{k_\rho^2}{k_1^2} r^{(p)}(k_\rho) e^{ik_{z,1}(z+z')} k_\rho d\alpha. \quad (\text{C.25})$$

For large input arguments, the Bessel function can be approximated as

$$\mathcal{J}_0(x) \approx \sqrt{\frac{2}{\pi x}} \cos\left(x - \frac{\pi}{4}\right), \quad x \gg 1, \quad (\text{C.26})$$

hence

$$\mathbf{G}_{zz}^{(i,ff)} \approx \frac{i}{4\pi} \int_{\alpha=0}^{\frac{\pi}{2}} \sqrt{\frac{2}{\pi k_\rho\rho_r}} \cos\left(k_\rho\rho_r - \frac{\pi}{4}\right) \frac{k_\rho^2}{k_1^2} r^{(p)}(k_\rho) e^{ik_{z,1}(z+z')} k_\rho d\alpha, \quad (\text{C.27})$$

where it can be found that

$$\cos\left(k_\rho\rho_r - \frac{\pi}{4}\right) e^{ik_{z,1}z} \approx \frac{1}{2} \left(e^{i(k_\rho\rho + k_{z,1}z)} e^{-i\frac{\pi}{4}} e^{-ik_\rho\mathbf{r}'\cdot\hat{\rho}} + e^{i(-k_\rho\rho + k_{z,1}z)} e^{i\frac{\pi}{4}} e^{ik_\rho\mathbf{r}'\cdot\hat{\rho}} \right), \quad (\text{C.28})$$

by using that ρ_r may be approximated as $\rho_r \approx \rho - \mathbf{r}' \cdot \hat{\boldsymbol{\rho}}$ when a point \mathbf{r}' is near the origin and another point \mathbf{r} lies a great distance from the origin, by similar arguments as in Eq. (2.38), along with the trigonometric identity $\cos(x) = \frac{e^{ix} + e^{-ix}}{2}$. By then using the coordinate transformations in Eq. (C.24) the RHS of this expression can be found to be

$$RHS = \frac{1}{2} \left(e^{ik_1 r (\sin \alpha \sin \theta + \cos \alpha \cos \theta)} e^{-i\frac{\pi}{4}} e^{-ik_\rho \mathbf{r}' \cdot \hat{\boldsymbol{\rho}}} + e^{ik_1 r (-\sin \alpha \sin \theta + \cos \alpha \cos \theta)} e^{i\frac{\pi}{4}} e^{ik_\rho \mathbf{r}' \cdot \hat{\boldsymbol{\rho}}} \right), \quad (C.29)$$

which can further be rewritten as

$$RHS = \frac{1}{2} \left(e^{ik_1 r \cos(\alpha - \theta)} e^{-i\frac{\pi}{4}} e^{-ik_\rho \mathbf{r}' \cdot \hat{\boldsymbol{\rho}}} + e^{ik_1 r \cos(\alpha + \theta)} e^{i\frac{\pi}{4}} e^{ik_\rho \mathbf{r}' \cdot \hat{\boldsymbol{\rho}}} \right), \quad (C.30)$$

where the trigonometric identity $\cos(a \pm b) = \cos(a) \cos(b) \mp \sin(a) \sin(b)$ has been utilised.

For large $k_1 r$, the phase of $e^{ik_1 r \cos(\alpha \mp \theta)}$ may oscillate quickly, resulting in cancellation of the integrand, however, this is not true at the extrema, that is when $\alpha \approx \theta$ and $\alpha + \theta \approx \pi$, due to slower oscillations around these points, and it is therefore possible to use a Taylor-expansion in order to get

$$e^{ik_1 r \cos(\alpha \mp \theta)} \approx e^{ik_1 r} e^{-ik_1 \frac{1}{2} r (\alpha \mp \theta)^2}. \quad (C.31)$$

It should be noted that since $\alpha \leq \pi/2$, $\alpha + \theta \approx \pi$ can only occur for $\theta = \pi/2$.

For now, consider the case where $0 \leq \theta < \pi/2$, then the integral in Eq. (C.27) reduces to

$$\mathbf{G}_{zz}^{(i,ff)} \approx \frac{ie^{ik_1 r}}{8\pi} \sqrt{\frac{2}{\pi k_1 r \sin^2 \theta}} e^{-i\frac{\pi}{4} r^{(p)}(k_\rho)} e^{-ik_\rho \mathbf{r}' \cdot \hat{\boldsymbol{\rho}}} e^{ik_{z,1} z'} \frac{k_\rho^3}{k_1^2} \int_0^{\frac{\pi}{2}} e^{-i\frac{1}{2} k_1 r (\alpha - \theta)^2} d\alpha, \quad (C.32)$$

where, $k_\rho \approx k_1 \sin \theta$ and $k_{z,1} \approx k_1 \cos \theta$ since $\alpha \approx \theta$ in the far-field. Furthermore, this integral includes only the first term on the RHS of Eq. (C.30), since $\theta < \pi/2$ and thus $\alpha + \theta \neq \pi$. This integral can then be extended to the integration interval from $-\infty$ to ∞ , since the extension parts are vanishing, as discussed above, hence the integral can now be evaluated using the identity

$$\int_{-\infty}^{\infty} e^{-ax^2} dx = \sqrt{\frac{\pi}{a}}, \quad (C.33)$$

yielding the far-field Green's tensor component,

$$\mathbf{G}_{zz}^{(i,ff)} = \frac{e^{ik_1 r}}{4\pi r} e^{-ik_\rho \mathbf{r}' \cdot \hat{\boldsymbol{\rho}}} e^{ik_{z,1} z'} r^{(p)}(k_\rho) \frac{k_\rho^2}{k_1^2}, \quad (C.34)$$

which is the expression in Eq. (2.80). For $\theta = \pi/2$, the same result is obtained even though both terms on the right-hand side of Eq. (C.30) must be utilised. This is because the terms enter with half weight as the limits are only reached from one side, so the terms are weighted half.

The coordinate transformations used in order to derive the far-field transmitted Green's tensor are on the form

$$z = r \cos \theta, \quad \rho = r \sin \theta, \quad \pi/2 < \theta \leq \pi \quad (C.35a)$$

$$k_\rho = k_3 \sin \alpha, \quad k_{z,3} = k_3 \cos \alpha, \quad (C.35b)$$

which leads to the expression in Eq. (2.82).

C.2 Curl of the Indirect Green's Tensor for the Electric Field

In order to obtain the surface current in Eq. (2.84) one has to find the curl of the indirect Green's tensor for the electric field from Eq. (2.79a), which can be recalled to be

$$\begin{aligned} \vec{\mathbf{G}}^{(i)}(\mathbf{r}, \mathbf{r}') = & \frac{i}{4\pi} \int_0^\infty \left\{ r^{(p)}(k_\rho) \left(\hat{\mathbf{z}}\hat{\mathbf{z}}\mathcal{J}_0(k_\rho\rho_r) \frac{k_\rho^2}{k_1^2} + \hat{\varphi}_r\hat{\varphi}_r \frac{\mathcal{J}'_0(k_\rho\rho_r)}{k_\rho\rho_r} \frac{k_{z,1}^2}{k_1^2} + \right. \right. \\ & \left. \left. \hat{\rho}_r\hat{\rho}_r\mathcal{J}_0''(k_\rho\rho_r) \frac{k_{z,1}^2}{k_1^2} - (\hat{\mathbf{z}}\hat{\rho}_r - \hat{\rho}_r\hat{\mathbf{z}}) \frac{ik_\rho k_{z,1}}{k_1^2} \mathcal{J}'_0(k_\rho\rho_r) \right) \right. \\ & \left. - r^{(s)}(k_\rho) \left(\hat{\varphi}_r\hat{\varphi}_r\mathcal{J}_0''(k_\rho\rho_r) + \hat{\rho}_r\hat{\rho}_r \frac{\mathcal{J}'_0(k_\rho\rho_r)}{k_\rho\rho_r} \right) \right\} e^{ik_{z,1}(z+z')} \frac{k_\rho}{k_{z,1}} dk_\rho, \end{aligned}$$

and can furthermore be split into an s- and a p-polarised part as

$$\begin{aligned} \mathbf{G}^{(i,s)}(\mathbf{r}, \mathbf{r}') &= \frac{i}{4\pi} \int_0^\infty -r^{(s)}(k_\rho) \left(\hat{\varphi}_r\hat{\varphi}_r\mathcal{J}_0''(k_\rho\rho_r) + \hat{\rho}_r\hat{\rho}_r \frac{\mathcal{J}'_0(k_\rho\rho_r)}{k_\rho\rho_r} \right) \frac{k_\rho}{k_{z,1}} e^{ik_{z,1}(z+z')} dk_\rho \\ \mathbf{G}^{(i,p)}(\mathbf{r}, \mathbf{r}') &= \frac{i}{4\pi} \int_0^\infty r^{(p)}(k_\rho) \left(\hat{\mathbf{z}}\hat{\mathbf{z}}\mathcal{J}_0(k_\rho\rho_r) \frac{k_\rho^2}{k_1^2} + \hat{\varphi}_r\hat{\varphi}_r \frac{\mathcal{J}'_0(k_\rho\rho_r)}{k_\rho\rho_r} \frac{k_{z,1}^2}{k_1^2} + \hat{\rho}_r\hat{\rho}_r\mathcal{J}_0''(k_\rho\rho_r) \frac{k_{z,1}^2}{k_1^2} \right. \\ & \left. - (\hat{\mathbf{z}}\hat{\rho}_r - \hat{\rho}_r\hat{\mathbf{z}}) \frac{ik_\rho k_{z,1}}{k_1^2} \mathcal{J}'_0(k_\rho\rho_r) \right) \frac{k_\rho}{k_{z,1}} e^{ik_{z,1}(z+z')} dk_\rho. \end{aligned}$$

Here it can be recalled that $k_1 = k_0 n_1$, $k_{z,1} = \sqrt{k_0^2 \varepsilon_1 - k_x^2 - k_y^2}$, $k_\rho = \sqrt{k_x^2 + k_y^2}$ and the subscript r indicates that the cylindrical coordinates have been defined with respect to relative distances. In order to find the curl of this, it is useful to evaluate each of the six terms separately, where it is used that

$$\nabla = \hat{\rho}_r \frac{\partial}{\partial \rho_r} + \hat{\varphi}_r \frac{1}{\rho_r} \frac{\partial}{\partial \varphi_r} + \hat{\mathbf{z}} \frac{\partial}{\partial z} \quad (\text{C.36})$$

in cylindrical coordinates. Upcoming, the derivatives of \mathcal{J}_0 will be used, which may be evaluated as

$$\mathcal{J}'_0(k_\rho\rho_r) = -\mathcal{J}_1(k_\rho\rho_r), \quad (\text{C.37a})$$

$$\mathcal{J}''_0(k_\rho\rho_r) = \frac{1}{2}(\mathcal{J}_2(k_\rho\rho_r) - \mathcal{J}_0(k_\rho\rho_r)), \quad (\text{C.37b})$$

by using the recurrence relation

$$\frac{\partial}{\partial x} \mathcal{J}_n(x) = \frac{\mathcal{J}_{n-1}(x) - \mathcal{J}_{n+1}(x)}{2}, \quad (\text{C.38})$$

along with

$$\mathcal{J}_{-n}(x) = (-1)^n \mathcal{J}_n(x). \quad (\text{C.39})$$

It should further be noted that $\mathcal{J}_0'''(k_\rho\rho_r)$ can be derived using the defining differential equation for the Bessel functions

$$\mathcal{J}_0''(x) = -\mathcal{J}_0(x) - \frac{1}{x} \mathcal{J}'_0(x) \quad (\text{C.40a})$$

$$\mathcal{J}_0'''(x) = -\mathcal{J}'_0(x) + \frac{1}{x^2} \mathcal{J}'_0(x) - \frac{1}{x} \mathcal{J}_0''(x). \quad (\text{C.40b})$$

Evaluating the curl of the seven terms of the indirect Green's tensor, in the order from left to right, starting with the s-polarised part, yields

$$\begin{aligned}
\text{Term 1: } \nabla \times \left(r^{(s)}(k_\rho) \hat{\varphi}_r \hat{\varphi}_r \mathcal{J}_0''(k_\rho \rho_r) e^{ik_{z,1}(z+z')} \right) \\
= r^{(s)}(k_\rho) e^{ik_{z,1}(z+z')} \left(-ik_{z,1} \mathcal{J}_0''(k_\rho \rho_r) \hat{\rho}_r \hat{\varphi}_r + k_\rho \left(\frac{\mathcal{J}_0''(k_\rho \rho_r)}{k_\rho \rho_r} + \mathcal{J}_0'''(k_\rho \rho_r) \right) \hat{\mathbf{z}} \hat{\varphi}_r \right) \\
= r^{(s)}(k_\rho) e^{ik_{z,1}(z+z')} \left(-ik_{z,1} \mathcal{J}_0''(k_\rho \rho_r) \hat{\rho}_r \hat{\varphi}_r + k_\rho \left(-\mathcal{J}_0'(k_\rho \rho_r) + \frac{\mathcal{J}_0'(k_\rho \rho_r)}{(k_\rho \rho_r)^2} \right) \hat{\mathbf{z}} \hat{\varphi}_r \right), \tag{C.41a}
\end{aligned}$$

$$\begin{aligned}
\text{Term 2: } \nabla \times \left(r^{(s)}(k_\rho) \hat{\rho}_r \hat{\rho}_r \frac{\mathcal{J}_0'(k_\rho \rho_r)}{k_\rho \rho_r} e^{ik_{z,1}(z+z')} \right) \\
= r^{(s)}(k_\rho) e^{ik_{z,1}(z+z')} \left(ik_{z,1} \frac{\mathcal{J}_0'(k_\rho \rho_r)}{k_\rho \rho_r} \hat{\varphi}_r \hat{\rho}_r - k_\rho \frac{\mathcal{J}_0'(k_\rho \rho_r)}{(k_\rho \rho_r)^2} \hat{\mathbf{z}} \hat{\varphi}_r \right), \tag{C.41b}
\end{aligned}$$

$$\begin{aligned}
\text{Term 3: } \nabla \times \left(r^{(p)}(k_\rho) \hat{\mathbf{z}} \hat{\mathbf{z}} \mathcal{J}_0(k_\rho \rho_r) \frac{k_\rho^2}{k_1^2} e^{ik_{z,1}(z+z')} \right) \\
= -r^{(p)}(k_\rho) \frac{k_\rho^3}{k_1^2} \mathcal{J}_0'(k_\rho \rho_r) e^{ik_{z,1}(z+z')} \hat{\varphi}_r \hat{\mathbf{z}}, \tag{C.41c}
\end{aligned}$$

$$\begin{aligned}
\text{Term 4: } \nabla \times \left(r^{(p)}(k_\rho) \hat{\varphi}_r \hat{\varphi}_r \mathcal{J}_0'(k_\rho \rho_r) \frac{k_{z,1}^2}{k_1^2 k_\rho \rho_r} e^{ik_{z,1}(z+z')} \right) \\
= r^{(p)}(k_\rho) \frac{k_{z,1}^2}{k_1^2} e^{ik_{z,1}(z+z')} \left(-ik_{z,1} \frac{\mathcal{J}_0'(k_\rho \rho_r)}{k_\rho \rho_r} \hat{\rho}_r \hat{\varphi}_r + k_\rho \frac{\mathcal{J}_0''(k_\rho \rho_r)}{k_\rho \rho_r} \hat{\mathbf{z}} \hat{\varphi}_r \right), \tag{C.41d}
\end{aligned}$$

$$\begin{aligned}
\text{Term 5: } \nabla \times \left(r^{(p)}(k_\rho) \hat{\rho}_r \hat{\rho}_r \mathcal{J}_0''(k_\rho \rho_r) \frac{k_{z,1}^2}{k_1^2} e^{ik_{z,1}(z+z')} \right) \\
= r^{(p)}(k_\rho) \frac{k_{z,1}^2}{k_1^2} \mathcal{J}_0''(k_\rho \rho_r) e^{ik_{z,1}(z+z')} (ik_{z,1} \hat{\varphi}_r \hat{\rho}_r - \frac{1}{\rho_r} \hat{\mathbf{z}} \hat{\varphi}_r) \tag{C.41e}
\end{aligned}$$

$$\begin{aligned}
\text{Term 6: } \nabla \times \left(-r^{(p)}(k_\rho) \hat{\mathbf{z}} \hat{\rho}_r \frac{ik_\rho k_{z,1}}{k_1^2} \mathcal{J}_0'(k_\rho \rho_r) e^{ik_{z,1}(z+z')} \right) \\
= r^{(p)}(k_\rho) \frac{ik_\rho k_{z,1}}{k_1^2} e^{ik_{z,1}(z+z')} \left(\mathcal{J}_0''(k_\rho \rho_r) \hat{\varphi}_r \hat{\rho}_r - \frac{\mathcal{J}_0'(k_\rho \rho_r)}{k_\rho \rho_r} \hat{\rho}_r \hat{\varphi}_r \right), \tag{C.41f}
\end{aligned}$$

$$\begin{aligned}
\text{Term 7: } \nabla \times \left(r^{(p)}(k_\rho) \hat{\rho}_r \hat{\mathbf{z}} \frac{ik_\rho k_{z,1}}{k_1^2} \mathcal{J}_0'(k_\rho \rho_r) e^{ik_{z,1}(z+z')} \right) \\
= r^{(p)}(k_\rho) \frac{-k_\rho k_{z,1}^2}{k_1^2} \mathcal{J}_0'(k_\rho \rho_r) e^{ik_{z,1}(z+z')} \hat{\varphi}_r \hat{\mathbf{z}}, \tag{C.41g}
\end{aligned}$$

where $\frac{k_\rho}{k_{z,1}}$ has been disregarded since taking the curl does not affect this fraction. Combining these terms, and reintroducing $\frac{k_\rho}{k_{z,1}}$, then yields

$$\begin{aligned}
\nabla \times \mathbf{G}^{(i,s)} = \frac{i}{4\pi} \int_0^\infty r^{(s)}(k_\rho) \left\{ -k_\rho \mathcal{J}_0'(k_\rho \rho_r) \hat{\mathbf{z}} \hat{\varphi}_r - ik_{z,1} \mathcal{J}_0''(k_\rho \rho_r) \hat{\rho}_r \hat{\varphi}_r \right. \\
\left. + ik_{z,1} \frac{\mathcal{J}_0'(k_\rho \rho_r)}{k_\rho \rho_r} \hat{\varphi}_r \hat{\rho}_r \right\} e^{ik_{z,1}(z+z')} \frac{k_\rho}{k_{z,1}} dk_\rho, \tag{C.42a}
\end{aligned}$$

$$\begin{aligned}
\nabla \times \mathbf{G}^{(i,p)} = \frac{i}{4\pi} \int_0^\infty r^{(p)}(k_\rho) \left\{ -k_\rho \mathcal{J}_0'(k_\rho \rho_r) \hat{\varphi}_r \hat{\mathbf{z}} - ik_{z,1} \frac{\mathcal{J}_0'(k_\rho \rho_r)}{k_\rho \rho_r} \hat{\rho}_r \hat{\varphi}_r \right. \\
\left. + ik_{z,1} \mathcal{J}_0''(k_\rho \rho_r) \hat{\varphi}_r \hat{\rho}_r \right\} e^{ik_{z,1}(z+z')} \frac{k_\rho}{k_{z,1}} dk_\rho, \tag{C.42b}
\end{aligned}$$

where it has been used that $k_\rho^2 + k_{z,1}^2 = k_1^2$.

Higher-Dimensional Polynomials

While one-dimensional polynomials only depended on a single parameter, a polynomial of N dimensions depend on N parameters, e.g. a two-dimensional polynomial, as described in Sec. 3.1.3, with the parameters u_1 and u_2 , as has been used for the mesh elements shown in Fig. 3.4. In this more general case with an N -dimensional polynomial of degree m defined on an element of dimension N , the number of polynomials, N_m , may be counted as choosing m out of $N + 1$ objects with replacement and without regard to order, expressed as

$$N_m = \binom{N + m}{m}, \quad (\text{D.1})$$

since each term of a polynomial, up to a constant, can be written as m products of $1, u_1, \dots, u_N$. Here the considered element is an N -dimensional simplex, where for the k^{th} element, a parameterisation $\mathbf{r}^{(k)}(u_1, \dots, u_N)$ is used analogously to the two-dimensional case defined in Eq. (3.1), in which case $0 \leq u_i \leq 1$ for all i and $\sum_i u_i \leq 1$ on the element.

By extrapolating the method for generating mesh points for the one-dimensional case, the mesh points may be evenly distributed along each parameterisation variable with points

$$\mathbf{r}_{(\nu_1, \dots, \nu_N)}^{(k)} = \mathbf{r}^{(k)} \left(\frac{\nu_1}{m}, \dots, \frac{\nu_N}{m} \right), \quad \text{for } \nu_i \in \{0, \dots, m\} \forall i, \quad \sum_{i=1}^N \nu_i \leq m, \quad (\text{D.2})$$

where the total number of points corresponds to choosing $N + 1$ out of m objects with replacement and without regard to order, which is equal to N_m on the element.

Consider the subset of polynomials that can be expressed as a product of linear factors, i.e. a polynomial expressed as

$$f(u_1, \dots, u_N) = \prod_{j=1}^m \left(a_{0,j} + \sum_{i=1}^N a_{i,j} u_i \right), \quad (\text{D.3})$$

then the zeros of a linear factor are along an $N - 1$ -dimensional plane, e.g. for the polynomial that is 1 in the mesh point (0.0) in Fig. 3.4b the zeros of the linear factor can be found along the line through the mesh points (1, 0) and (0, 1). As the polynomial only has a zero if at least one of its factors does, the set of zeros of the polynomial is then the union of the zeros of the linear factors. In order to define a basis of polynomial functions of degree m on an N -dimensional element, a polynomial is, as previously stated, defined for each mesh point such that its value is 1 in that

point and 0 in the remaining points, hence

$$f_{(\nu_1, \dots, \nu_N)} \left(\frac{\nu'_1}{m}, \dots, \frac{\nu'_N}{m} \right) = \prod_{i=1}^N \delta_{\nu_i, \nu'_i}. \quad (\text{D.4})$$

In order to construct such a polynomial with linear factors, the union of the planes of zeros of the m factors must intersect all mesh points except for $\mathbf{r}_{\nu_1, \dots, \nu_N}$. Now it will be shown that such linear factors can be found.

For the linear factors, $P_{i,\eta}(u_i)$, the following $m(N+1)$ functions are considered, where

$$P_{i,\eta}(u_i) = u_i - \frac{\eta}{m}, \quad i \in \{1, \dots, N+1\}, \quad \eta \in \{0, \dots, m-1\}, \quad (\text{D.5})$$

where, for ease of notation, it will be used that $u_{N+1} = 1 - \sum_{i=1}^N u_i$. In this case, the zeros intersect the mesh points if

$$P_{i,\eta} \left(\frac{\nu_i}{m} \right) = \frac{\nu_i - \eta}{m} = 0, \quad \text{for } \nu_i = \eta, \quad i \in \{0, \dots, N+1\}, \quad (\text{D.6})$$

where $\nu_{N+1} = m - \sum_{i=1}^N \nu_i$. In Fig. D.1 such an example is shown with $m = 2$ with two linear factors intersecting all mesh points with the exception of $\mathbf{r}_{2,0}$.

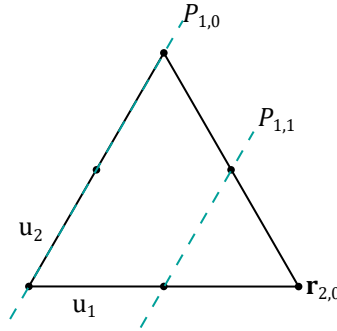


Figure D.1: The zeros of the linear factors $P_{1,0}$ and $P_{1,1}$ are shown with dashed lines on the triangular element, where it can be seen that they intersect every mesh point with the exception of $\mathbf{r}_{2,0}$.

If the product of linear factors at $\mathbf{r}_{(\nu_1, \dots, \nu_N)}$ for all i is then evaluated from $\eta = 0$ to $\eta = \nu_i - 1$ it is evident from Eq. (D.6) that

$$\prod_{i=1}^{N+1} \prod_{\eta=0}^{\nu_i-1} P_{i,\eta}(u_i) \neq 0. \quad (\text{D.7})$$

From this it is seen that the total number of products from the inner sequence product results in polynomials of the ν_i^{th} order, while the outer sequence product results in polynomials of the $(\nu_i + 1)^{\text{th}}$ order, hence the order of the resulting polynomial is given by

$$\sum_{i=1}^N \nu_i + m - \sum_{i=1}^N \nu_i = m. \quad (\text{D.8})$$

Now, consider a mesh point, $\mathbf{r}_{(\nu'_1, \dots, \nu'_N)}$, that is not a zero of the product of linear factors at

$\mathbf{r}_{(\nu_1, \dots, \nu_N)}$, then it follows that $\nu'_i \geq \nu_i$ for all i , hence

$$m - \sum_{i=1}^N \nu'_i \geq m - \sum_{i=1}^N \nu_i \Rightarrow \sum_{i=1}^N \nu'_i \leq \sum_{i=1}^N \nu_i, \quad (\text{D.9})$$

with the only solution $\nu'_i = \nu_i$ for all i proving that $\mathbf{r}_{(\nu_1, \dots, \nu_N)}$ is the only nonzero mesh point of this polynomial. By rescaling, the basis polynomials can therefore be defined on an element by

$$f_{(\nu_1, \dots, \nu_N)}(u_1, \dots, u_N) = \frac{\prod_{i=1}^{N+1} \prod_{\eta=0}^{\nu_i-1} P_{i,\eta}(u_i)}{\prod_{i=1}^{N+1} \prod_{\eta=0}^{\nu_i-1} P_{i,\eta}(\nu_i/m)}. \quad (\text{D.10})$$

However, arbitrary polynomials of the m^{th} order can not be expressed by these basis polynomials as only polynomials of linear factors has been considered in the derivation of this expression. The surface current on element k of the scatterer may then be written for the i^{th} component of the current as

$$\mathbf{J}_{s,i}(\mathbf{r}^{(k)}(u_1, \dots, u_N)) = \hat{\mathbf{t}}_{i,k}(u_1, \dots, u_N) \sum_{\nu_1, \dots, \nu_N} J_{i,k,(\nu_1, \dots, \nu_N)} f_{(\nu_1, \dots, \nu_N)}(u_1, \dots, u_N) \quad (\text{D.11})$$

where $J_{i,k,(\nu_1, \dots, \nu_N)}$ corresponds to the i^{th} component of the current in direction $\hat{\mathbf{t}}_{i,k}(\frac{\nu_1}{m}, \dots, \frac{\nu_N}{m})$ located at $\mathbf{r}^{(k)}(\frac{\nu_1}{m}, \dots, \frac{\nu_N}{m})$.

Analytic Scattering from a Spherical Particle

In this appendix spherical coordinates will be utilized.

Consider a plane wave propagating in a medium with the dielectric constant ε_1 and a particle of radius a with the dielectric constant ε_2 , which is placed with its center in the origin. For this geometry the dielectric function is given by

$$\varepsilon(\mathbf{r}) = \begin{cases} \varepsilon_1, & r > a \\ \varepsilon_2, & r < a \end{cases}. \quad (\text{E.1})$$

The incident electric field will be chosen to propagate along the z-axis and be polarized along the x-axis. Using spherical wave functions, the incident field can be expressed as

$$\mathbf{E}_0(\mathbf{r}) = \hat{\mathbf{x}}E_0e^{ik_0\sqrt{\varepsilon_1}z} = E_0 \sum_{n=1}^{\infty} i^n \frac{2n+1}{n(n+1)} \left(\mathbf{m}_{o,n,1}^{(1)}(\mathbf{r}) - \mathbf{m}_{e,n,1}^{(1)}(\mathbf{r}) \right), \quad (\text{E.2})$$

where the spherical wave functions are defined as

$$\mathbf{m}_{o,n,i}^{(1)}(\mathbf{r}) = \frac{\cos\varphi}{\sin\theta} \mathcal{P}_n^1(\cos\theta) j_n(k_0\sqrt{\varepsilon_i}r) \hat{\boldsymbol{\theta}} - \sin\varphi \frac{d\mathcal{P}_n^1(\cos\theta)}{d\theta} j_n(k_0\sqrt{\varepsilon_i}r) \hat{\boldsymbol{\varphi}}, \quad (\text{E.3a})$$

$$\begin{aligned} \mathbf{n}_{e,n,i}^{(1)}(\mathbf{r}) &= n(n+1) \cos\varphi \mathcal{P}_n^1(\cos\theta) \frac{j_n(k_0\sqrt{\varepsilon_i}r)}{k_0\sqrt{\varepsilon_i}r} \hat{\mathbf{r}} + \cos\varphi \frac{d\mathcal{P}_n^1(\cos\theta)}{d\theta} \frac{[k_0\sqrt{\varepsilon_i}r j_n(k_0\sqrt{\varepsilon_i}r)]'}{k_0\sqrt{\varepsilon_i}r} \hat{\boldsymbol{\theta}} \\ &\quad - \frac{\sin\varphi}{\sin\theta} \mathcal{P}_n^1(\cos\theta) \frac{[k_0\sqrt{\varepsilon_i}r j_n(k_0\sqrt{\varepsilon_i}r)]'}{k_0\sqrt{\varepsilon_i}r} \hat{\boldsymbol{\varphi}}, \end{aligned} \quad (\text{E.3b})$$

where the subscript o and e denotes that the function is odd or even, respectively, while the subscript $i = 1$ indicates the area outside the particle, while $i = 2$ is inside the particle. Furthermore has the short-hand notation $[xj_n(x)]' \equiv \frac{d}{dx}[xj_n(x)]$ been utilized, where

$$j_n(x) = \sqrt{\frac{\pi}{2x}} \mathcal{J}_{n+1/2}(x) \quad (\text{E.4})$$

is the spherical Bessel function and \mathcal{P}_n^m is the Legendre function of the first kind, given by

$$\mathcal{P}_n^m(x) = (1-x^2)^{m/2} \frac{d^m}{dx^m} \mathcal{P}_n(x), \quad (\text{E.5})$$

with the Legendre polynomial

$$\mathcal{P}_n(x) = \frac{1}{2^n n!} \frac{d^n}{dx^n} (x^2 - 1)^n. \quad (\text{E.6})$$

The field inside the spherical particle can be expressed as

$$\mathbf{E}(\mathbf{r}) = E_0 \sum_{n=1}^{\infty} i^n \frac{2n+1}{n(n+1)} \left(c_n \mathbf{m}_{n,2}^{(1)}(\mathbf{r}) - id_n \mathbf{n}_{n,2}^{(1)}(\mathbf{r}) \right), \quad r < a, \quad (\text{E.7})$$

while the field outside of the particle can be found as

$$\mathbf{E}(\mathbf{r}) = \mathbf{E}_0(\mathbf{r}) + \mathbf{E}_{\text{scat}}(\mathbf{r}), \quad r > a, \quad (\text{E.8})$$

where the scattered field can be expressed as

$$\mathbf{E}_{\text{scat}}(\mathbf{r}) = E_0 \sum_{n=1}^{\infty} i^n \frac{2n+1}{n(n+1)} \left(a_n \mathbf{m}_{o,n,1}^{(2)}(\mathbf{r}) - ib_n \mathbf{n}_{e,n,2}^{(2)}(\mathbf{r}) \right). \quad (\text{E.9})$$

Here, $\mathbf{m}_{o,n,i}^{(2)}(\mathbf{r})$ and $\mathbf{n}_{e,n,i}^{(2)}(\mathbf{r})$ are defined to be identical to $\mathbf{m}_{o,n,i}^{(1)}(\mathbf{r})$ and $\mathbf{n}_{e,n,i}^{(1)}(\mathbf{r})$ from Eq. (E.3) and , except that the spherical Bessel function should be replaced by the spherical Hankel function,

$$h_n(x) = \sqrt{\frac{\pi}{2x}} \left(\mathcal{J}_{n+1/2}(x) + i\mathcal{Y}_{n+1/2}(x) \right) = \sqrt{\frac{\pi}{2x}} \mathcal{H}_{n+1/2}^{(1)}(x), \quad (\text{E.10})$$

where \mathcal{Y}_n is the Bessel function of the second kind, and $\mathcal{H}_n^{(1)}$ is the Hankel function of the first kind.

The expansion coefficients can be obtained from the continuity of the tangential component of the electric and magnetic field across the particle surface. They are given by [15, pp. 392]

$$a_n = -\frac{j_n(k_0\sqrt{\varepsilon_2}a)[k_0\sqrt{\varepsilon_1}aj_n(k_0\sqrt{\varepsilon_1}a)]' - j_n(k_0\sqrt{\varepsilon_1}a)[k_0\sqrt{\varepsilon_2}aj_n(k_0\sqrt{\varepsilon_2}a)]'}{j_n(k_0\sqrt{\varepsilon_2}a)[k_0\sqrt{\varepsilon_1}ah_n(k_0\sqrt{\varepsilon_1}a)]' - h_n(k_0\sqrt{\varepsilon_1}a)[k_0\sqrt{\varepsilon_2}aj_n(k_0\sqrt{\varepsilon_2}a)]'} \quad (\text{E.11a})$$

$$b_n = -\frac{\varepsilon_1 j_n(k_0\sqrt{\varepsilon_1}a)[k_0\sqrt{\varepsilon_2}aj_n(k_0\sqrt{\varepsilon_2}a)]' - \varepsilon_2 j_n(k_0\sqrt{\varepsilon_2}a)[k_0\sqrt{\varepsilon_1}aj_n(k_0\sqrt{\varepsilon_1}a)]'}{\varepsilon_1 h_n(k_0\sqrt{\varepsilon_1}a)[k_0\sqrt{\varepsilon_2}aj_n(k_0\sqrt{\varepsilon_2}a)]' - \varepsilon_2 j_n(k_0\sqrt{\varepsilon_2}a)[k_0\sqrt{\varepsilon_1}ah_n(k_0\sqrt{\varepsilon_1}a)]'} \quad (\text{E.11b})$$

$$c_n = -\frac{j_n(k_0\sqrt{\varepsilon_1}a)[k_0\sqrt{\varepsilon_1}ah_n(k_0\sqrt{\varepsilon_1}a)]' - h_n(k_0\sqrt{\varepsilon_1}a)[k_0\sqrt{\varepsilon_1}aj_n(k_0\sqrt{\varepsilon_1}a)]'}{j_n(k_0\sqrt{\varepsilon_2}a)[k_0\sqrt{\varepsilon_1}ah_n(k_0\sqrt{\varepsilon_1}a)]' - h_n(k_0\sqrt{\varepsilon_1}a)[k_0\sqrt{\varepsilon_2}aj_n(k_0\sqrt{\varepsilon_2}a)]'} \quad (\text{E.11c})$$

$$d_n = -\frac{j_n(k_0\sqrt{\varepsilon_2}a)[k_0\sqrt{\varepsilon_1}aj_n(k_0\sqrt{\varepsilon_1}a)]' - j_n(k_0\sqrt{\varepsilon_1}a)[k_0\sqrt{\varepsilon_2}aj_n(k_0\sqrt{\varepsilon_2}a)]'}{\frac{n_1}{n_2}j_n(k_0\sqrt{\varepsilon_2}a)[k_0\sqrt{\varepsilon_1}ah_n(k_0\sqrt{\varepsilon_1}a)]' - \frac{n_1}{n_2}h_n(k_0\sqrt{\varepsilon_1}a)[k_0\sqrt{\varepsilon_2}aj_n(k_0\sqrt{\varepsilon_2}a)]'}. \quad (\text{E.11d})$$

In the case of a PEC, where $\varepsilon_1 \ll \varepsilon_2$,

$$a_n = \frac{j_n(k_0\sqrt{\varepsilon_1}a)}{h_n(k_0\sqrt{\varepsilon_1}a)} \quad (\text{E.12a})$$

$$b_n = \frac{[k_0\sqrt{\varepsilon_1}aj_n(k_0\sqrt{\varepsilon_1}a)]'}{[k_0\sqrt{\varepsilon_1}ah_n(k_0\sqrt{\varepsilon_1}a)]'}. \quad (\text{E.12b})$$

The magnetic field can be obtained by utilising Eq. (2.2c) and that $\nabla \times \mathbf{m} = k\mathbf{n}$ and $\nabla \times \mathbf{n} = k\mathbf{m}$ [23, Ch. 26]

$$\mathbf{H}_0 = -i\sqrt{\frac{\varepsilon_0}{\mu_0}}n_1E_0 \sum_n i^n \frac{2n+1}{n(n+1)} (\mathbf{n}_{o,n,i}^{(1)}(\mathbf{r}) - i\mathbf{m}_{e,n,i}^{(1)}(\mathbf{r})), \quad (\text{E.13a})$$

$$\mathbf{H}_{\text{scat}} = -i\sqrt{\frac{\varepsilon_0}{\mu_0}}n_1E_0 \sum_n i^n \frac{2n+1}{n(n+1)} (a_n \mathbf{n}_{o,n,i}^{(2)}(\mathbf{r}) - ib_n \mathbf{m}_{e,n,i}^{(2)}(\mathbf{r})), \quad (\text{E.13b})$$

where

$$\mathbf{m}_{e,n,i}^{(1)}(\mathbf{r}) = -\frac{\sin \varphi}{\sin \theta} P_n^1(\cos \theta) j_n(k_0\sqrt{\varepsilon_i}r) \hat{\boldsymbol{\theta}} - \cos \varphi \frac{dP_n^1(\cos \theta)}{d\theta} j_n(k_0\sqrt{\varepsilon_i}r) \hat{\boldsymbol{\varphi}}, \quad (\text{E.14a})$$

$$\begin{aligned} \mathbf{n}_{o,n,i}^{(1)}(\mathbf{r}) &= n(n+1) \sin \varphi P_n^1(\cos \theta) \frac{j_n(k_0\sqrt{\varepsilon_i}r)}{k_0\sqrt{\varepsilon_i}r} \hat{\mathbf{r}} + \sin \varphi \frac{dP_n^1(\cos \theta)}{d\theta} \frac{[k_0\sqrt{\varepsilon_i}rj_n(k_0\sqrt{\varepsilon_i}r)]'}{k_0\sqrt{\varepsilon_i}r} \hat{\boldsymbol{\theta}} \\ &+ \cos \varphi P_n^1(\cos \theta) \frac{[k_0\sqrt{\varepsilon_i}rj_n(k_0\sqrt{\varepsilon_i}r)]'}{k_0\sqrt{\varepsilon_i}r} \hat{\boldsymbol{\varphi}}, \end{aligned} \quad (\text{E.14b})$$

where it is once again the case that $\mathbf{m}_{e,n,i}^{(2)}(\mathbf{r})$ and $\mathbf{n}_{o,n,i}^{(2)}(\mathbf{r})$ are defined to be identical to $\mathbf{m}_{e,n,i}^{(1)}(\mathbf{r})$

and $\mathbf{n}_{o,n,i}^{(1)}(\mathbf{r})$ where the spherical Bessel function should be replaced by the spherical Hankel function.

To obtain the surface current, Eq. (2.55b) is used. The total magnetic field is the sum of the two expressions in Eq. (E.13) and in spherical symmetry $\mathbf{n} \times \hat{\varphi} = -\hat{\theta}$ and $\mathbf{n} \times \hat{\theta} = \hat{\varphi}$, so the $\hat{\varphi}$ and $\hat{\theta}$ components of the surface current are given as

$$\mathbf{J}_{\varphi}(\theta, \varphi) = -i\sqrt{\frac{\varepsilon_0}{\mu_0}}n_1E_0 \sum_n i^n \frac{2n+1}{n(n+1)} \left(\frac{\sin \varphi}{k_0\sqrt{\varepsilon_i}r} \frac{dP_n^1(\cos \theta)}{d\theta} [[k_0\sqrt{\varepsilon_i}r j_n(k_0\sqrt{\varepsilon_i}r)]' + a_n[k_0\sqrt{\varepsilon_i}r h_n(k_0\sqrt{\varepsilon_i}r)]' + i \frac{\sin \varphi}{\sin \theta} P_n^1(\cos \theta) [j_n(k_0\sqrt{\varepsilon_i}r) + b_n h_n(k_0\sqrt{\varepsilon_i}r)] \right) \quad (\text{E.15a})$$

$$\mathbf{J}_{\theta}(\theta, \varphi) = i\sqrt{\frac{\varepsilon_0}{\mu_0}}n_1E_0 \sum_n i^n \frac{2n+1}{n(n+1)} \left(\frac{\cos \varphi}{k_0\sqrt{\varepsilon_i}r} \frac{P_n^1(\cos \theta)}{\sin \theta} [[k_0\sqrt{\varepsilon_i}r j_n(k_0\sqrt{\varepsilon_i}r)]' + a_n[k_0\sqrt{\varepsilon_i}r h_n(k_0\sqrt{\varepsilon_i}r)]' + i \cos \varphi \frac{dP_n^1(\cos \theta)}{d\theta} [j_n(k_0\sqrt{\varepsilon_i}r) + b_n h_n(k_0\sqrt{\varepsilon_i}r)] \right). \quad (\text{E.15b})$$

In Fig E.1 the error obtained for varying numbers of summations in the analytical solution for the surface current. It is seen that in this case the current seems to converge so that for more than 30 summations the error does not vary, however, the relative error should converge for all values of $\frac{\lambda}{a}$, where it should be noted that a small relative wavelength should need more summations in order to converge compared to a large relative wavelength.

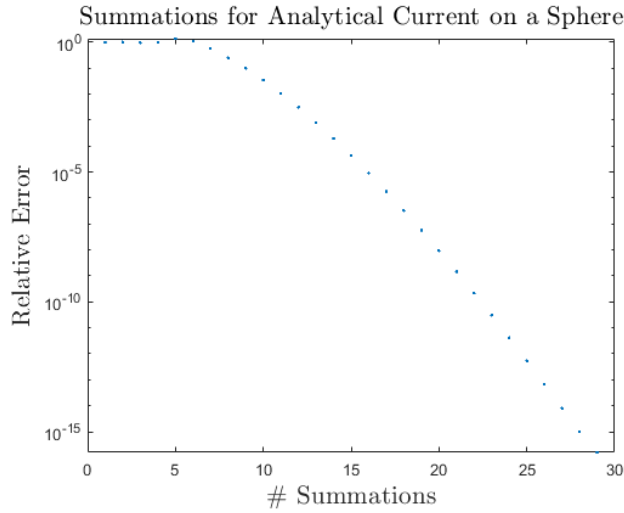


Figure E.1: The relative error between varying numbers of summations in the analytical solution for a sphere, where $\theta = 0$, $\varphi = 0$ and $\frac{\lambda}{a} = 1$.

E.1 Scattering Cross Section

When the relative wavelength is varied the extinction and scattering cross sections are used, and can be expressed in terms of the expansion coefficients as

$$\sigma_{\text{ext}} = -\frac{2\pi}{(k_0\sqrt{\varepsilon_1})^2} \sum_{n=1}^{\infty} (2n+1) \text{Real}\{a_n + b_n\}, \quad (\text{E.16a})$$

$$\sigma_{\text{scat}} = -\frac{2\pi}{(k_0\sqrt{\varepsilon_1})^2} \sum_{n=1}^{\infty} (2n+1) \{|a_n|^2 + |b_n|^2\}, \quad (\text{E.16b})$$

where the absorption cross section is the difference between the two

$$\sigma_{\text{abs}} = \sigma_{\text{ext}} - \sigma_{\text{scat}}. \quad (\text{E.17})$$

E.2 Legendre Polynomials

The Legendre polynomials are defined as solutions to Legendre's differential equation [24]

$$\frac{d}{dx} \left[(1-x^2) \frac{d\mathcal{P}_n(x)}{dx} \right] + n(n+1)\mathcal{P}_n(x) = 0, \quad (\text{E.18})$$

with $\mathcal{P}_n(1) = 1$. The derivatives of the Legendre polynomials can be evaluated using the recurrence relation

$$\frac{x^2-1}{n} \frac{d}{dx} \mathcal{P}_n(x) = x\mathcal{P}_n(x) - \mathcal{P}_{n-1}(x). \quad (\text{E.19})$$

The derivative needed for the analytic solution of a spherical scatterer is of the associated Legendre polynomial given by $\mathcal{P}_n^1(x) = \sqrt{1-x^2} \frac{d}{dx} \mathcal{P}_n(x)$. In the case of $x = \cos \theta$,

$$\begin{aligned} \frac{d}{d\theta} \mathcal{P}_n^1(\cos \theta) &= \frac{n}{\sin^2 \theta} \mathcal{P}_n^1(\cos \theta) - n \frac{\cos \theta}{\sin^2 \theta} \mathcal{P}_{n-1}(\cos \theta) - \frac{n}{\sin^2 \theta} (n \cos \theta (\cos \theta \mathcal{P}_n(\cos \theta) \\ &\quad - \mathcal{P}_{n-1}(\cos \theta)) - (n-1) (\cos \theta \mathcal{P}_{n-1}(\cos \theta) - \mathcal{P}_{n-2}(\cos \theta))) \\ &= n \frac{1-n \cos^2 \theta}{\sin^2 \theta} \mathcal{P}_n(\cos \theta) + 2n(n-1) \frac{\cos \theta}{\sin^2 \theta} \mathcal{P}_{n-1}(\cos \theta) - \frac{n(n-1)}{\sin^2 \theta} \mathcal{P}_{n-2}(\cos \theta). \end{aligned} \quad (\text{E.20})$$

In the limit as θ goes to zero the derivative of the Legendre polynomial becomes

$$\frac{d}{d\theta} \mathcal{P}_n^1(\cos \theta) = \cos \theta \frac{d}{d \cos \theta} \mathcal{P}_n(\cos \theta) + \sin \theta \frac{d}{d\theta} \frac{d}{d \cos \theta} \mathcal{P}_n(\cos \theta). \quad (\text{E.21})$$

It can be seen from Eq. (E.18), by utilising the chain rule, that at $x = 1$ it follows that $\frac{d}{d \cos \theta} \mathcal{P}_n(\cos \theta) = \frac{n(n+1)}{2}$ and as $\theta \rightarrow 0$, $\sin \theta \rightarrow 0$ and $\cos \theta \rightarrow 1$ and thus the second term vanishes and the derivative reduces to

$$\lim_{\theta \rightarrow 0} \frac{d}{d \cos \theta} \mathcal{P}_n^1(\cos \theta) = \frac{n(n+1)}{2}. \quad (\text{E.22})$$

For the limit $\theta \rightarrow \pi$ the derivative, again by using the chain rule on Eq. (E.18) along with the property of parity, $\mathcal{P}_n(-x) = (-1)^n \mathcal{P}_n(x)$, becomes

$$\lim_{\theta \rightarrow \pi} \frac{d}{d \cos \theta} \mathcal{P}_n^1(\cos \theta) = -(-1)^n \frac{n(n+1)}{2}, \quad (\text{E.23})$$

and the derivative of the associated Legendre polynomial in the limit $\theta \rightarrow \pi$ then yields

$$\lim_{\theta \rightarrow \pi} \frac{d}{d \cos \theta} \mathcal{P}_n^1(\cos \theta) = (-1)^n \frac{n(n+1)}{2}. \quad (\text{E.24})$$